

HEPARIN COATED AND 2-DEOXY-D-GLUCOSE CONJUGATED IRON  
OXIDE NANOPARTICLES FOR BIOLOGIC APPLICATIONS

A THESIS SUBMITTED TO  
THE GRADUATE SCHOOL OF NATURAL AND APPLIED SCIENCES  
OF  
MIDDLE EAST TECHNICAL UNIVERSITY

BY  
YELİZ AKPINAR

IN PARTIAL FULFILLMENT OF THE REQUIREMENTS  
FOR  
THE DEGREE OF DOCTOR OF PHILOSOPHY  
IN  
CHEMISTRY

SEPTEMBER 2017



Approval of the Thesis;

**HEPARIN COATED AND 2-DEOXY-D-GLUCOSE CONJUGATED IRON  
OXIDE NANOPARTICLES FOR BIOLOGIC APPLICATIONS**

submitted by **YELİZ AKPINAR** in a partial fulfillment of the requirements for the degree of **Doctor of Philosophy in Chemistry Department, Middle East Technical University** by,

Prof. Dr. Gülbin Dural Ünver  
Dean, Graduate School of **Natural and Applied Sciences** \_\_\_\_\_

Prof. Dr. Cihangir Tanyeli  
Head of Department, **Chemistry** \_\_\_\_\_

Prof. Dr. Mürvet Volkan  
Supervisor, **Chemistry Department, METU** \_\_\_\_\_

Prof. Dr. N. Tülün Güray  
Co-Supervisor: **Biological Science Dept., METU** \_\_\_\_\_

**Examining Committee Members:**

Prof. Dr. Macit Özenbaş  
Dept.of Metallurgical and Materials Engineering, METU \_\_\_\_\_

Prof. Dr. Mürvet Volkan  
Chemistry Dept, METU \_\_\_\_\_

Prof. Dr. Ceyhan Kayran  
Chemistry Dept, METU \_\_\_\_\_

Assoc. Prof. Dr. Sevi Öz  
Chemistry Dept., Ahi Evran University \_\_\_\_\_

Assoc. Prof. Dr. Murat Kaya  
Chemical Engineering and Applied Chemistry Dept., Atılım University \_\_\_\_\_

**Date:** 08.09.2017



**I hereby declare that all information in this document has been obtained and presented in accordance with academic rules and ethical conduct. I also declare that, as required by these rules and conduct, I have fully cited and referenced all material and results that are not original to this work.**

Name, Last name: Yeliz Akpınar

Signature:

## **ABSTRACT**

### **HEPARIN COATED AND 2-DEOXY-D-GLUCOSE CONJUGATED IRON OXIDE NANOPARTICLES FOR BIOLOGIC APPLICATIONS**

Akpınar, Yeliz

Ph. D., Department of Chemistry

Supervisor: Prof. Dr. Mürvet Volkan

Co-Supervisor: Prof. Dr. N. Tülün Güray

September 2017, 127 pages

Over the past decade, there has been an increasing interest in using nanotechnology for cancer therapy. Magnetic-based systems containing magnetic nanoparticles have gained popularity because of their unique ability to be used in magnetic resonance imaging, magnetic targeting, drug carrying and hyperthermia. The last one represents a novel therapeutic concept to cancer treatment. In biomedical and clinical applications the most commonly used magnetic nanomaterials are the iron oxide nanoparticles. Current progress in the synthesis of iron oxide nanoparticles with different shapes (flower, cube, spherical) and compositions show that the heating power of the magnetic material can be optimized for hyperthermia.

Compared to the therapy of using chemotherapeutic agents or molecular-targeting therapeutic agents, an alternative antitumor approach can be proposed by considering tumor metabolism. The reason cancer is so fast growing is that the mitochondria have been deactivated, so the cells avoid apoptosis, as well as being able to grow in the absence of oxygen (glycolysis). Dichloroacetate (DCA) which is a pyruvate dehydrogenase kinase inhibitor, reverses this process, induces apoptosis, decreases proliferation, and inhibits tumor growth. However, therapeutically prohibitive high DCA doses are needed for tumor growth suppression. Thus, preparation of magnetic nanoparticles designed to carry pharmacologically relevant doses of DCA directly to

the tumor site and enhance its effective cellular uptake may represent a more effective therapeutic option.

In this study, flower, cubic and spherical shaped iron oxide nanoparticles, having high heating power that can be used in hyperthermia application were prepared. For inductive heating of magnetic nanoparticles, an induction device was designed. Hyperthermia studies was started by using spherical iron oxide nanoparticles. The surface of nanoparticles prepared was modified with heparin, a natural polymer and DKA was embedded into heparin layer. However, for effectively targeting mitochondria, triphenylphosphonium cation was incorporated to DKA through a biodegradable amide linkage before loading on to the nanoparticle. Finally nanoparticles was conjugated to 2-deoxy-D-glucose (2-DG) in order to transport the particles into the cells via glucose transformers present on the cell membranes. It needs to be stated that, besides DKA and hyperthermia, both heparin and 2-DG are known to play role in apoptosis process. Therefore these novel nanoparticles are expected to deliver their cargo directly to cancer cell and cause a cell death via apoptosis. The binding and uptake of nanoparticles, cytotoxicity and apoptosis were investigated using liver cancer cell line (HepG2). It is known that iron oxide nanoparticles are used as a contrast reagent in MRI systems. Consequently, these nanoparticles were also useful for monitoring the outcomes of the medical treatment by magnetic resonance imaging, MRI.

Keywords: Magnetic Nanoparticles, Hyperthermia, Cancer, Dichloroacetate

## ÖZ

### **BİYOLOJİK UYGULAMALAR İÇİN HEPARİN KAPLI 2-DEOKSİ-D-GLUKOZ BAĞLI DEMİR OKSİT NANOPARÇACIKLAR**

Akpınar, Yeliz

Doktora, Kimya Bölümü

Tez Yöneticisi: Prof. Dr. Mürvet Volkan

Ortak Tez Yöneticisi: Prof. Dr. N. Tülün Güray

Eylül 2017, 127 sayfa

Nanoteknolojinin kanser tedavisi için kullanılmasına olan ilgi geçtiğimiz yıllarda giderek artmaktadır. Manyetik rezonans görüntüleme, manyetik hedefleme, ilaç taşıma ve hipertermi uygulamalarında kullanılabilme yetenekleri ile çarpıcı özelliklere sahip olan manyetik nanoparçacıkların kullanıldığı manyetik temelli sistemlerden biri olan hipertermi, kanser tedavisinde terapötik araçtır. Biyomedikal ve klinik uygulamalarda en sık kullanılan manyetik nanomalzemeler demir oksit nanoparçacıklardır. Yakın zamanda, farklı şekillerdeki (çiçek, küp, küre vb.) ve kompozisyonlardaki demir nanoparçacıkların sentezlenmesindeki gelişmeler hipertermi amaçlı kullanımları için manyetik malzemelerin ısıtma yeteneğinin optimize edilebileceğini göstermiştir.

Kemoterapötik ajanların veya moleküler hedefli terapötik ajanların kullanıldığı tedavilerin yanında tümör metabolizması da göz önünde bulundurularak alternatif bir tümör karşıtı yaklaşım önerilebilir. Kanser hücrelerinin hızlı büyümesinin nedeni mitokondrilerin devre dışı kalması; buna bağlı olarak hücrelerin apoptoza gitmek istememesi ve oksijen yokluğunda da büyüebilmesidir (glikoliz). Bir pirüvat dehidrokinaz inhibitörü olan dikloroasetat (DKA) bu süreci, apoptozu da kapsayacak şekilde, tersine çevirir, proliferasyonu azaltır ve tümör büyümesini engeller. Ancak tümör büyümesini engelleyecek tedavi için oldukça yüksek dozda DKA kullanımı gerekmektedir. Bu durumda farmakolojik olarak uygun dozda DCA'yı tümör

bölgesine taşıyabilecek ve hücrel alım etkinliğini artıracak manyetik nanoparçacıkların hazırlanması daha etkili bir tedavi seçeneği olarak görünmektedir. Bu çalışmada, hipertermide kullanılmak üzere yüksek ısıtma yeteneğine sahip çiçek küp ve küre şeklinde süperparamanyetik demir oksit nanoparçacıklar hazırlandı. Hazırlanan manyetik nanoparçacıkların hipertermi verimleri incelemek üzere parçacıklara değişken manyetik alan uygulayan cihaz tasarlandı. Hipertermi ölçümlerine küre şekilli demir oksit parçacıklar ile başlandı. Küre şekilli nanoparçacıkların yüzeyleri doğal bir polimer olan heparin ile modifiye edilerek DKA'nın bu heparin tabakasının içinde tutturularak taşınması sağlandı. Son olarak, parçacıkların hücre zarında bulunan glikoz taşıyıcılarından hücre içine geçebilmesi için nanoparçacıklar 2-deoksi-D-glikoz (2-DG) ile işaretlendi. DKA ve hipertermiminin yanı sıra heparin ve 2-DG de apoptoz sürecinde rol oynamaktadır. Buna göre, bu yeni nanoparçacıkların taşıdıkları yükleri doğrudan kanser hücresine ulaştırmaları ve apoptoz yoluyla hücre ölümüne neden olmaları beklenmektedir. Bu çalışmada, kanserli karaciğer hücre dizisi (HepG2) kullanılarak nanoparçacıkların bağlanması ve hücre içine alınması, sitotoksitesi ve apoptotik etkileri incelenmiştir. Demir oksit nanoparçacıklarının MRI ölçümlerinde kontrast ajanı olarak kullanıldığı bilinmektedir. Dolayısı ile hazırlanan nanoparçacıklar, tıbbi tedavinin sonuçlarının manyetik rezonans görüntüleme (MRI) sistemi ile takip edilmesine de olanak sağlayacaktır.

Anahtar kelimeler:Manyetik Nanoparçacık, Kanser, Hipertermi,Dikloroasetat.





To my family

## ACKNOWLEDGEMENTS

I would like to express my deep appreciation and respect to my supervisor Prof. Dr. Mürvet VOLKAN for her endless guidance, support, encouragement, understanding, patience and suggestions throughout this study. I have learned many things from her not only chemistry but also social and academic life. She always picked up me and gave me moral when I felt terrible and operated

I am grateful to my co-supervisor Prof. Dr. N. Tülün GÜRAY for valuable contribution to this thesis about biological experiment.

I want to express my gratitude to my Thesis Monitoring Committee members, Prof. Dr. Ceyhan KAYRAN and Prof. Dr. Macit ÖZENBAŞ for their valuable suggestions and comments to complete this thesis in the best way.

My special thanks to Assist. Prof. Dr. Ş. Betül SOPACI for sharing her experiences about organic chemistry and biology. She spent long hours with me for discussions of results.

I am especially grateful and thankful Ezgi Başak SARAÇ for contribution to biological experiments. Without her decisive and disciplined work, I could not progress in biological experiments

I would like to thank my lab mate Seçkin ÖZTÜRK for helping hyperthermia studies. Additionally, has given me advice about explaining of TEM and SEM images of nanoparticles.

I have benefited from the experience ideas and knowledge of Assost. Dr. Gülay ERTAŞ about science and academic life. I would like to thank her for having developed my this side.

Special thanks to Elif AŞIK for her endless friendship. Her advice and supports have been valuable for me.

I would like to thank to Sezin ÖZDEMİR. She had been my student and then she has been my colleague. She always made every endeavor whenever I need help.

My special thanks to my labmates Dilek Ünal, Selin BORA, Zuhale Selvi GÜNER, Pakizan TASMAN, Erhan ÖZDEMİR, Emrah YILDIRIM, Merve Nur GÜVEN, Begüm AVCI, Başak DÜGENCİLİ, Pınar MERCAN, Canan HÖÇÜK, and Assist. Prof. Dr. Çiğdem AY for their valuable friendship, endless help, and support. They have become the second family for me.

I should thank Halil Memiş, Hamit Çağlar, and Cengiz Şimşek who are technical personal of Chemistry department in METU. They have always helped me when I need help about technical problems.

I would like to thank Prof. Dr Özdemir DOĞAN and her students for helping me about organic chemistry experiments.

Finally, my special thanks to my family members Nuri AKPINAR, Hatice AKPINAR Filiz AKPINAR and Merve AKPINAR for their endless, love patience, and moral support. Additionally, I would like to thank to my little nephew ALP. They have never made me alone and desperate when I meet the problem. If they are not in my life, I could not achieve this level.

I would like to thank TÜBİTAK for awarding scholarship (2211A) during my doctorate program. With this scholarship, I was eager to study and search more.

I would like to extend my deepest due to DPT-ÖYP and Ahi Evran University for supporting me to complete my Ph.D. study in the Chemistry Department of METU.

## TABLE OF CONTENTS

ABSTRACT .....	v
ÖZ.....	vii
ACKNOWLEDGEMENTS .....	x
TABLE OF CONTENTS .....	xii
LIST OF TABLES .....	xviii
LIST OF FIGURES.....	xix
LIST OF ABBREVIATIONS AND SYMBOLS.....	xxv
CHAPTERS	
1. INTRODUCTION .....	1
1.1 Introduction to Nanotechnology.....	1
1.1.1 Nanobiotechnology .....	1
1.2 Introduction to Cancer .....	2
1.2.1 Cancer İllness and Cancer Cell Metabolism .....	2
1.2.2 Therapy and Diagnosis of Cancer .....	5
1.2.3 Mitochondrial Cancer Therapy .....	5
1.2.3.1 Dichloroacetate .....	6
1.2.4 Nanotechnology and Cancer .....	8
1.2.4.1 Drug delivery .....	8
1.2.4.2 Imaging or detection system.....	9
1.2.4.3 Hyperthermia .....	10
1.3 Introduction of Magnetic Nanoparticles.....	10

1.3.1	Magnetic Nanoparticles .....	10
1.3.2	Iron Oxide Magnetic Nanoparticles (IONPs) .....	11
1.3.2.1	Hematite ( $\alpha$ -Fe <sub>2</sub> O <sub>3</sub> ).....	11
1.3.2.2	Magnetite (Fe <sub>3</sub> O <sub>4</sub> ).....	11
1.3.2.3	Maghemite ( $\gamma$ - Fe <sub>2</sub> O <sub>3</sub> ).....	12
1.3.3	Magnetism of Iron Oxide Nanoparticles.....	12
1.3.4	Preparation Methods of Iron Oxide Nanoparticles .....	13
1.3.4.1	Co-precipitation Methods.....	15
1.3.4.2	Thermal Decomposition Method.....	15
1.3.4.3	Polyol Method .....	17
1.3.4.4	Hydrothermal Method .....	18
1.3.5	Magnetic Nanoparticle and Biomedical Application.....	18
1.3.6	Modification of Magnetic Nanoparticles for Biomedical Applications .....	19
1.3.6.1	Heparin .....	20
1.4	Hyperthermia.....	21
1.4.1	Magnetic Hyperthermia .....	21
1.4.2	Mechanism of Magnetic Hyperthermia .....	22
1.4.2.1	Eddy Current .....	22
1.4.2.2	Hysteresis losses .....	22
1.4.2.3	Relaxation mechanism.....	24
1.4.3	Specific Absorption Rate (SAR).....	24
1.4.4	Applications of Magnetic Hyperthermia.....	25
1.5	Purpose of This Study .....	26
2.	EXPERIMENTAL.....	27

2.1	Instrumentation .....	27
2.1.1	Infrared Spectrophotometry .....	27
2.1.2	UV-vis Spectrophotometry .....	27
2.1.3	X-Ray Diffraction .....	27
2.1.4	Nuclear Magnetic Resonance Spectrometry .....	27
2.1.5	Thermal Gravimetric Analyser.....	28
2.1.6	Zeta Potential Measurements .....	28
2.1.7	Transmission Electron Microscopy.....	28
2.1.8	Scanning Electron Microscopy .....	28
2.1.9	VSM .....	28
2.1.10	Reactor .....	28
2.1.11	AC Generator .....	29
2.2	Chemicals and Reagents.....	29
2.2.1	Preparation of Spherical Shape Fe <sub>3</sub> O <sub>4</sub> NPs.....	29
2.2.2	Preparation of Flower Shape Fe <sub>2</sub> O <sub>3</sub> NPs.....	29
2.2.3	Synthesizing of Iron Oxide Nanoparticles by Hydrothermal Method .	29
2.2.4	Preparation of Cubic Shape Fe <sub>2-3</sub> O <sub>4</sub> NPs .....	29
2.2.5	Synthesis of (3-hydroxypropyl)triphenylphosphonium-(TPP-(CH <sub>2</sub> ) <sub>3</sub> -OH) .....	30
2.2.6	Synthesis of (3-(2,2-dichloroacetoxy)propyl) triphenylphosphonium (TPP-DCA) by Using Dichloroacetic anhydride .....	30
2.2.7	Synthesis of (3-(2,2-dichloroacetoxy)propyl) triphenylphosphonium (TPP-DCA) By Using Dichloroacetylchloride .....	31

2.2.8	Surface Modification of Nanoparticles: Coating by Heparin, Attaching TPP-DCA to Heparin Coated Iron Oxide surface and Embedding TPP-DCA into Heparin Layer .....	31
2.2.9	Attaching 2-deoxy-D-glucose .....	31
2.3	Biological Experiments .....	31
2.3.1	Cell Growth.....	31
2.4	Procedures .....	32
2.4.1	Preparation Magnetic Nanoparticles.....	32
2.4.1.1	Preparation Spherical Shape Fe <sub>3</sub> O <sub>4</sub> NPs.....	32
2.4.1.2	Preparation Flower Shape Fe <sub>2</sub> O <sub>3</sub> NPs .....	33
2.4.1.3	Synthesizing Iron Oxide Nanoparticles by Hydrothermal Method..	34
2.4.1.4	. Preparation of Hydrophilic Cube Shape Fe <sub>3</sub> O <sub>4</sub> NPs.....	35
2.4.1.5	Conversion of Hydrophobic Cubic Shaped Iron Oxide Nanoparticles into Hydrophilic Form .....	38
2.5	Preparation TPP-(CH <sub>2</sub> ) <sub>3</sub> -OH) and TPP-DCA.....	38
2.5.1	Synthesis of (3-hydroxypropyl)triphenylphosphonium-(TPP-(CH <sub>2</sub> ) <sub>3</sub> -OH) .....	38
2.5.2	Synthesis of (3-(2,2-dichloroacetoxy)propyl) triphenylphosphonium ( TPP-DCA) by Using Dichloroacetic anhydride.....	39
2.5.3	Synthesis of (3-(2,2-dichloroacetoxy)propyl) triphenylphosphonium ( TPP-DCA) by Using Dichloroacetylchloride.....	40
2.6	Surface Modification of Iron oxide Nanoparticles.....	41
2.6.1	Coating by Heparin .....	41
2.6.2	Attaching TPP-DCA to Heparin Coated Iron Oxide Surface .....	41
2.6.3	Embedding TPP-DCA into Heparin Layer .....	42

2.6.4	Attaching 2-deoxy-D-glucose .....	43
2.6.5	Determination 2-Deoxy-D-glucose By Cupric Reduction Based on Methods .....	43
2.7	Biological Experiments .....	44
2.7.1	Cell Culture Conditions.....	44
2.7.2	Cell Passaging/ Trypsinization.....	45
2.7.3	Cell Culturing.....	45
2.7.4	Trypan Blue Exclusion (Cell Counting).....	46
2.7.5	XTT Cell Proliferation Assay .....	46
2.8	Designing Inductive Heating Device.....	47
3.	RESULTS AND DISCUSSION .....	51
3.1	Preparation of Magnetic Nanoparticles .....	51
3.1.1	Preparation Spherical Shape Fe <sub>3</sub> O <sub>4</sub> NPs .....	51
3.1.2	Preparation of Flower Shape Fe <sub>2</sub> O <sub>3</sub> NPs.....	54
3.1.3	Synthesizing Iron Oxide Nanoparticles by Hydrothermal Method.....	62
3.1.4	Synthesis of Hydrophobic Cubic Shaped Iron Oxide Nanoparticles by Thermal Decomposition Methods.....	65
3.1.4.1	Synthesis of Cubic Shaped Iron Oxide Nanoparticles by Using Oleic Acid and Undecanoic Acid as A Surfactant.....	65
3.1.4.2	Synthesis of Cubic Shaped Iron Oxide Nanoparticles by Using Oleic Acid - Oleate as Surfactant.....	70
3.1.4.3	Conversion of Hydrophobic Cubic Shaped Iron Oxide Nanoparticles into Hydrophilic form.....	77
3.2	Preparation TPP-(CH <sub>2</sub> ) <sub>3</sub> -OH and TPP-DCA .....	79
3.2.1	Synthesis of TPP-(CH <sub>2</sub> ) <sub>3</sub> -OH .....	80



3.2.2	Synthesis of TPP-DCA by Using Dichloroacetic Anhydride .....	80
3.2.3	Synthesis of TPP-DCA by Using Dichloroacetylchloride .....	88
3.3	Modification of iron oxide Nanoparticles for Biomedical Applications.....	90
3.3.1	Heparin Coating .....	91
3.3.2	Attaching TPP-DCA to Heparin Coated Iron Oxide Surface .....	94
3.3.3	Embedding TPP-DCA into Heparin Layer .....	96
3.3.4	Determination 2-Deoxy-d-glucose By Cupric Based Methods .....	99
3.4	Biological Experiments .....	99
3.4.1	XTT Cell Cytotoxicity Assay .....	99
3.4.2	Viable Cell Counting with Trypan Blue Exclusion Method.....	102
3.5	Results of Inductive Heating Measurements.....	107
4.	CONCLUSION.....	111
	REFERENCES.....	113
	CURRICULUM VITAE .....	125

## LIST OF TABLES

### TABLES

Table 1. List of different parameters of synthesizing flower shaped iron oxide nanoparticles.....	34
Table 2. Optimization studies of thermal decomposition method. Surfactant is undecanoic acid.....	36
Table 3. Optimization studies of synthesis cubic shaped iron oxides by using oleic acid-sodium oleate as a surfactant.....	37
Table 4. Solvent system that was used for tlc trials. ....	81
Table 5. Table of zeta potential measurements.....	92
Table 6. Optimization studies of inductive heating measurements .....	108

## LIST OF FIGURES

### FIGURES

Figure 1. Scheme of a.) Normal cell mitochondria, b.) Mitochondrial dysfunction of normal cell.....	4
Figure 2. Chemical structure of sodium dichloroacetate.....	6
Figure 3. Scheme of effect of dichloroacetate on mitochondrial dysfunction .....	7
Figure 4. Mechanism of polyol method [68].....	17
Figure 5. Usage of magnetic nanoparticles for biomedical applications .....	19
Figure 6. Chemical structure of heparin.....	20
Figure 7. Hysteresis curve of superparamagnetic(red line) and paramagnetic (blue line) nanoparticle under the magnetic field.....	23
Figure 8. Image of experimental set up of co-precipitation methods.....	32
Figure 9. Image of experimental set up of polyol method .....	33
Figure 10. Image of experimental set up of hydrothermal method .....	34
Figure 11. Image of experimental set up of thermal decomposition method.....	35
Figure 12. Reaction for the synthesis of TPP-(CH <sub>2</sub> ) <sub>3</sub> -OH) .....	38
Figure 13. Reaction for the synthesis of TPP-DCA by using dichloroacetic anhydride.....	39
Figure 14. Reaction for the synthesis of TPP-DCA by using dichloroacetylchloride	40
Figure 15. Scheme of procedure of heparin coating of spherical iron oxide nanoparticles.....	41
Figure 16. Scheme of procedure of TPP-DCA attaching on magnetic nanoparticle surface .....	41
Figure 17. Scheme of procedure of heparin coating of magnetic nanoparticles second layer.....	42

Figure 18. Scheme of attaching 2-deoxy-D-glucose by EDC/NHS coupling method onto the surface of double layer heparin coated and tpp-dca loaded magnetic nanoparticles.....	43
Figure 19. Scheme of detection procedure of glucose on magnetic nanoparticle surface .....	44
Figure 20. Front view of the 13 turn coils used in the hyperthermia system to induce heating from nanoparticles in the sample.....	48
Figure 21. TEM image and size distribution of iron oxide nanoparticles that were prepared by co-precipitation method.....	52
Figure 22. XRD pattern of iron oxide nanoparticle which were prepared by co-precipitation method.....	53
Figure 23. Behavior of spherical shaped magnetite nanoparticles under the magnetic field.....	54
Figure 24. TEM image of flower-like shaped iron oxide nanoparticles that were prepared absence of dea with 1 °C/min heating slope, 2h reflux time at 220 °C; .....	55
Figure 25. TEM images of the nanoparticles prepared by polyol method: solvent is TEG:DEA (1:1, v/v) heating rate is 1 °C/min, reflux temperature is 220 °C. reflux time is (a) 2h (table 1. 2b), (b) 1h (table1. 3c), (c) 0.5 h (Table1.4e) and (d) size distribution histogram for the particles presented in part c of this figure, i.e. 0.5 h reflux time. ..	57
Figure 26. XRD pattern of flower-like shaped iron oxide nanoparticles .....	58
Figure 27. Behavior of flower-like shaped iron oxide nanoparticles under the magnetic field.....	58
Figure 28. Magnetization versus magnetic field curves for flower shaped iron oxide nanoparticles ( table 1 exp 4e )at 298 K .....	60
Figure 29. Magnetization versus magnetic field curves for flower shaped iron oxide nanoparticles (Table1, 4e) at 5 K. ....	61
Figure 30. SEM image of iron oxide nanoparticles which were prepared by hydrothermal method .....	62
Figure 31. Behavior of iron oxide nanoparticles which were prepared by hydrothermal method, under the magnetic field.....	63

Figure 32. a) normal and b) baseline corrected xrd pattern of iron oxide nanoparticles which were prepared by hydrothermal method.....	64
Figure 33. TEM image and the size histogram of the nanoparticles prepared by thermal decomposition method by using oleic acid as surfactant.....	66
Figure 34. TEM images of iron oxide nanoparticles that are synthesized in undecanoic acid by applying a) 1 h and b) 45 min complex formation heating period. Corresponding size distribution histograms of the nanoparticles are given below each tem images. ....	67
Figure 35. TEM images of iron oxide nanoparticles prepared in undecanoic acid with a) 2,5-hours, b) 1-hour and c)1.5-hours intermediate heating applications at constant complex formation( at 60 °C, 45 min) and reflux time (45 min). Corresponding size distribution histograms of the nanoparticles are given below each tem images. ....	68
Figure 36. TEM images of iron oxide nanoparticles prepared at low concentration of undecanoic acid ( $\frac{1}{4}$ fold of the original amount), 45 min complex formation period at 60 °C, 1.5-hours intermediate heating at 200 °c and 45 min refluxing time at the highest possible temperature. Corresponding size distribution histogram of the nanoparticles is given below the tem image.....	69
Figure 37. TEM images of iron oxide nanoparticles that were synthesized by using a) fe-oleate-oleic acid, ( Table 3,a), b) sodium oleate (without preparing fe-oleate complex), ( Table 3,b) as a surfactant system.....	71
Figure 38. TEM images of cubic iron oxide nanoparticles that were synthesized by using sodium oleate and nacl. Corresponding size distribution histogram of the nanoparticles is given below the tem image (Table 3,c).....	72
Figure 39. Behaviors of cubic shaped iron oxide nanoparticles near the magnet .....	73
Figure 40. XRD pattern of cubic shaped iron oxide nanoparticles. Baseline corrected spectrum has been inserted into graph .....	74
Figure 41. Magnetization versus magnetic field curves for cubic shaped iron oxide nanoparticles ( Table 3c) at 298 K.....	75
Figure 42. Magnetization versus magnetic field curves for cubic shaped iron oxide nanoparticles ( Table 3,c) at 5K. ....	76

Figure 43. Cubic shaped magnetic nanoparticles dispersed in water phase after PVP coating.....	77
Figure 44. TEM image of PVP coated iron oxide nanoparticles.....	78
Figure 45. IR spectra of naked (blue line) and PVP coated (red line) iron oxide nanoparticles.....	79
Figure 46 H-NMR spectrum of TPP-(CH <sub>2</sub> ) <sub>3</sub> -OH precursor. <sup>1</sup> H NMR (400 mhz, CDCl <sub>3</sub> ) :δ 7.75 (m, 15H), 4.91 (t, 1H), 3.77 (m, 4H), 1.82 (m, 2H).....	80
Figure 47. Appearance of TLC plate after dcm: methanol: (90:10) and dcm: methanol: ethanol (100:10:70) solvent system were applied.....	82
Figure 48. H-NMR spectrum of TPP-DCA purified using silica-TLC plate with methanol-dcm (9:1) solvent mixture.the molecular formula of the expected product (TPP-DCA) is given as inset and the corresponding peak positions are labeled (a-e). <sup>1</sup> h nmr (400 mhz, CDCl <sub>3</sub> ) : δ 7.74 (dddd, 15H), 6.22 (d, 1H), 6.04 – 5.91 (m, 1H), 5.69 – 5.23 (m, 1H), 4.55 (t, j = 5.4 hz, 2H), 3.95 (t, , 2H), 3.79 – 3.51 (m, 1H), 1.97 (dd, , 1H), 1.34 – 1.09 (m, 1H).....	83
Figure 49. Purification of TPP-DCA utilizing tlc plate and dcm: ethyl acetate solvent mixture in various volume ratios 95:5, 9:5, 7:3 and 10:5. ....	84
Figure 50. Appearance of preparative tlc plate first plate image shows the thin line of the TPP-DCA prepared by using dichloroacetic anhydride, the last plate shows the separation of the same sample after running with dcm: ethylacetate in 2:1 (v/v).....	85
Figure 51. NMR spectrum of lower part (Red Frame 1), TPP-DCA prepared with by using dichloroacetic anhydride. The structure of the the molecular formula of the expected product (tp-dca) is also given in the figure and the position of the protons are labeled with lower case letters (a-e). <sup>1</sup> h nmr (400 mhz, CDCl <sub>3</sub> ) δ 7.78 (s, 15H), 6.14 (s, 1H), 4.43 (d, h), 3.79 (s,2H), 2.04 (s, 2H).....	86
Figure 52. NMR spectrum of upper part (Red Frame 2).....	87
Figure 53. Mechanism of reaction of TPP-(CH <sub>2</sub> ) <sub>3</sub> -OH and dichloroacetic anhydride.....	88
Figure 54. Appearance of preparative TLC. ....	89

Figure 55. NMR spectrum of TPP-DCA prepared by using dichloroacetylchloride. The molecular formula of the expected product (TPP-DCA) is also given in the figure and the position of the protons are labeled with lower case letters (a-e).. <sup>1</sup> H NMR (400 mhz, CDCl <sub>3</sub> ) δ 7.94 – 7.57 (m, 15H), 6.15 (s, 1H), 4.59 (s, 2H), 3.89 (s, 2H), 2.17 – 1.86 (m, 3H). .....	90
Figure 56. Scheme for coating of iron oxide nanoparticles with negatively charged heparin.....	91
Figure 57. .TEM image of heparin coated spherical iron oxide nanoparticles .....	92
Figure 58. IR spectra of naked (black line) and heparin coated (green line) iron oxide nanoparticles .....	93
Figure 59. Scheme for the immobilization of positively charged TPP-DCA on to negatively charged heparin coated iron oxide nanoparticles. ....	94
Figure 60. IR spectra of heparin coated (green line) and TPP-DCA attached heparin coated (blue line) iron oxide nanoparticles. ....	95
Figure 61. Chemical structure of TPP-DCA .....	95
Figure 62. Scheme of heparin coating procedure (second time) TPP-DCA attached heparin coated iron oxide nanoparticles and changing of surface charge.....	96
Figure 63. TEM image of 2-DG-HEP-TPP-DCA-HEP coated IONPs.....	97
Figure 64. TGA curve of naked iron oxide (black line), single layer heparin coated iron oxide nanoparticles (red line) and double layer heparin coated and TPP-DCA loaded iron oxide nanoparticles (blue line).....	98
Figure 65. Light microscopy images of a) dc, b)50 µg/ml, c) 250 µg/ml, d) 500 µg/ml, e) 750 µg/ml and 1000 µg/ml 2-DG-HEP-TPP-DCA-HEP coated IONPs treated HepG2 cells after 24-hour treatment without pre-wash.....	100
Figure 66. XTT results of a) dc, b)50 µg/ml, c) 250 µg/ml, d) 500 µg/ml, e) 750µg/ml and f)1000µg/ml 2-DG-HEP-TPP-DCA-HEP coated ionps treated HepG2 cells after 24-hour treatment without washing (pre-wash) procedure .....	100
Figure 67. Light microscopy images of a) dc, b)125 µg/ml, c) 250 µg/ml, d) 375 µg/ml, e) 500µg/ml and f)750µg/ml 2-DG-HEP-TPP-DCA-HEP coated IONPs treated HepG2 cells after 24-hour treatment with washing procedure. ....	101

Figure 68. XTT results of a) dc, b)125 µg/ml, c) 250 µg/ml, d) 375 µg/ml, e) 500µg/ml and f)750µg/ml 2-DG-HEP-TPP-DCA-HEP coated ionps treated HepG2 cells after 24-hour treatment with washing procedure.....	102
Figure 69. Cell viability with the method.....	103
Figure 70. Comparison of cell viability of 2-DG-HEP-TPP-DCA-HEP coated IONPs with 2-DG-HEP coated IONPs at 250µg/ml, 500µg/ml, 1000µg/ml concentrations by the assay. ....	104
Figure 71. Comparison of cell viability of naked, 2-DG-TPP-DCA-HEP coated and 2-DG-HEP-TPP-DCA-HEP coated IONPs at 500µg/ml concentration by trypan blue exclusion( TBE) method. ....	105
Figure 72. Comparison of cell viability of 2 -DG-HEP-TPP-DCA-HEP coated IONPs, TPP-DCA and Na-DCA at 500µg/ml concentration with the method.....	106
Figure 73. (a,b,c,e,f) Temperature kinetic curves obtained after application of an alternating magnetic field on samples dispersed in water at various instrumental conditions stated in table 6, d.) Photograph of copper pipe coil. ....	109
Figure 74. Comparison of cell viability of 2 -DG-HEP-TPP-DCA-HEP coated IONPs, TPP-DCA and NaDCA molecules at 500µg/ml concentration by trypan blue exclusion method (TBE).....	113



## LIST OF ABBREVIATIONS AND SYMBOLS

TPP-DCA	(3-(2,2-dichloroacetoxy)propyl) triphenylphosphonium
TPP-OH	(3-hydroxypropyl)triphenylphosphonium
XTT	2,3-Bis-(2-Methoxy-4-Nitro-5-Sulfophenyl)-2H-Tetrazolium-5-Carboxanilide
2-DG	2-Deoxy-d-glucose
DCA	Dichloroacetate
DCM	Dichloromethane
DEA	Diethanolamine
EtAoc	Ethyl acetate
FAO	Fatty acid $\beta$ -oxidation
FBS	Fetal Bovine Serum
IR	Infrared
IONPS	Iron oxide Nanoparticles
HepG2	Liver hepatocellular carcinoma
NPs	Nanoparticles
DMP	N-Dimethylformamide
NMR	Nuclear Magnetic Resonance
PVP	Polyvinylpyrrolidone
Ph	Potential of hydrogen
PDH	Pyruvate dehydrogenase
PDK	Pyruvate dehydrogenase kinase
SEM	Scanning Electron Microscopy
SAR	Specific Absorption Rate
IC50	The half maximal inhibitory concentration
TGA	Thermal Gravimetric Analyser
TLC	Thin Layer Chromatography

TEM	Transmission Electron Microscopy
TCA	Tricarboxylic acid
TCA	Tricarboxylic acid
TEG	Triethylene Glycol
PPh <sub>3</sub>	Triphenylphosphin
UV-Vis	Ultraviole -visible
VSM	Vibrating sample magnetometer
XRD	X-Ray Diffraction



## CHAPTER 1

### INTRODUCTION

#### 1.1 Introduction to Nanotechnology

Nanotechnology is a new approach which provides production and examination of materials on the molecular scale. This approach has uncovered mystery of nature at too many fields such as energy, environment, healthy and electronic. Nanodevices, nanocomposite materials etc., produced by using nanotechnology increase quality of life and lifetime of people that also causes the emergence and rising of nanotechnology [1].

##### 1.1.1 Nanobiotechnology

Nanobiotechnology is a major part of nanotechnology which combines engineering, chemistry, biology, physics, electronic and material science. Nanobiotechnology plays an important role in implementing and developing many useful tools in the study of life. Drug delivery systems, gene therapy, sensitive imaging and sensor systems of illness, artificial organs, micro fabricated medical devices have been developed by using nanobiotechnology [2]. Not only medical area but also agricultural, food industry and environmental issues are hot topic for nanobiotechnology [3-5].

Over the 40 years, polymers, ceramics, metals and metal compounds such as oxides, sulfides etc. have been used for the preparation of nanomaterials for biomedical applications [6].

Nanoparticles that are based on noble metals such as Au, Ag widely used for bioimaging, biosensors, and drug delivery system. Their Surface plasmon resonance (SPR) absorption properties make them unique tool for this type applications. Surface

plasmon resonance (SPR) absorption is produced by the collective oscillation of conducting electrons in the metal NP core upon interacting with the incident light, which depends on size and shape of nanoparticles, distance between nanoparticles and dielectric properties of medium [7].

Another type of nanoparticles is magnetic nanoparticles. Because of their magnetic properties, stabilities and lower toxicities, usage of them for biomedical application has taken attention [8].

Additionally, quantum dots (QDs) that are a semiconductor or silisium nanometer sized particles, have an important role because of their luminescence and fluorescence properties which give them the opportunity for being used at biosensing, bioimaging and, immunoassays studies [9].

Polymeric materials are used for therapy and genetic engineering. Drug loaded polymeric nanomaterial release drugs when they are degraded by changing temperature or pH. Controlling the conditions, such as solubility and reactivity properties of polymers, provides dose control for drug delivery systems. [10]. When nanostructure and polymeric materials are combined, mechanic and functionality of these nanocomposite materials increase and become more desirable for biomedical applications [11].

## **1.2 Introduction to Cancer**

### **1.2.1 Cancer İllness and Cancer Cell Metabolism**

Despite the fact that cancer causes have been studied over the past four decades, scientists still do not understand exact reason and metabolism of cancer [12]. Cancer disease is caused by genetic instability and accumulation of multiple molecular alterations [13]. Cancer cells are different from normal cells in term of uncontrolled proliferation, aggression, resistance to apoptosis and anti-growth signals and metastasis properties [14].

Tumor initiation and growth is related to mitochondrial process. The alterations in glucose metabolism, compromise of intrinsic apoptotic and the production of reactive oxygen species (ROS) are result in mitochondrial function disorders. At normal cell,

Glucose is metabolized to pyruvate through glycolysis, and then carbon dioxide in the mitochondria through oxidative phosphorylation (OXPHOS) under the aerobic conditions. In the absence of sufficient oxygen, normal cells may displace the glycolytic pyruvate from mitochondrial oxidation and may reduce it to lactate. On the other hand, at tumor cells glucose metabolism occurs in different pathway. Changes in glucose metabolism in cancer can be explained by Warburg's effect. Although glucose metabolism has enough oxygen for aerobic respiration, it tends to glycolysis instead of aerobic respiration and ATP production efficiency decrease per a molecule glucose. Such changes in cellular metabolism may be desirable for tumor cell growth, since cellular growth and proliferation require biosynthetic intermediates, and the availability of these intermediates may increase with this alteration in cellular metabolism. Additionally, decreasing intrinsic apoptotic function is another result of these alterations so tumor cells become immortal [15-16]. Scheme of alternation of cellular metabolism in mitochondrion shown in Figure 1a and b.

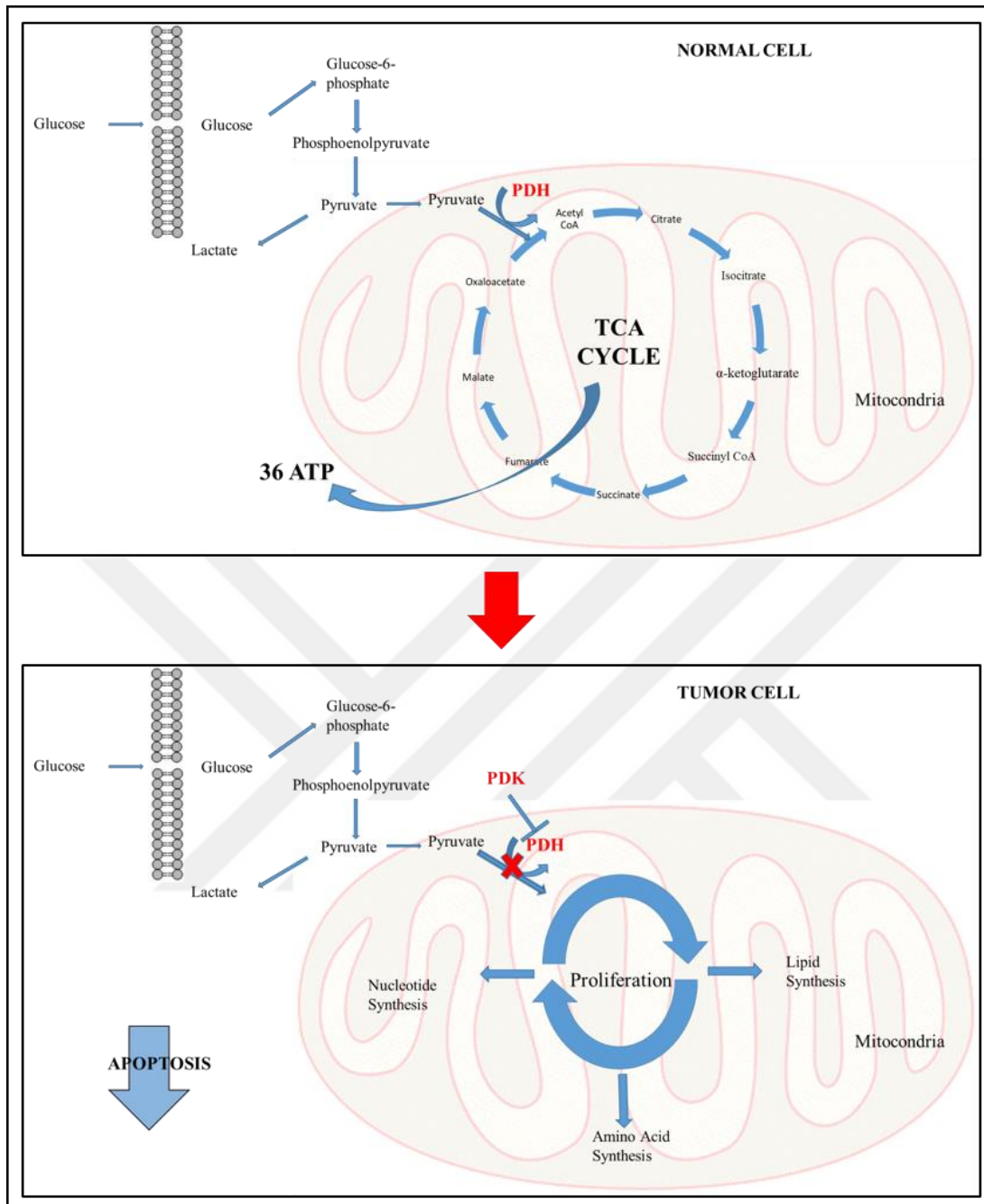


**Figure 1.** Scheme of a.) Normal cell mitochondria, b.) Mitochondrial dysfunction of normal cell

### **1.2.2 Therapy and Diagnosis of Cancer**

During the fifty years, significant progress has been made in the cancer treatment and diagnosis work. Nevertheless, exact cure and sensitive detection system have not developed yet. Available detection systems are not enough and take a long time. Therefore, for many cases cancer cells are metastasized to healthy tissues when diagnosed [13, 17].

For therapy, problems are efficiency, localization and toxicity problems of present therapeutic agents. Anti-cancer drugs or radiations could not identify normal and cancer cells, therefore healthy tissues are also affected negatively. Additionally, side and toxic effect of therapeutic agents cause damage to healthy cell [13, 17].

### **1.2.3 Mitochondrial Cancer Therapy**

Mitochondria is an organelle in a cell, which has important roles in cell variability. Tricarboxylic acid cycle (TCA), oxidative phosphorylation, glycolysis, fatty acid metabolism and pro-apoptotic protein mechanism are some of them. Also, they are responsible for energy production and apoptosis function of the cell. Therefore mitochondrial dysfunction causes neurodegenerative diabetes, obesity, neuromuscular diseases, and cancer [18, 19].

The relation between mitochondrial dysfunction and cancer led to the emergence of a new chemotherapeutic treatment approach. Therefore drugs have been designed, based on the correction of these dysfunctions and the (re)activation of cell death programs. Some pharmacological agents affect directly the mitochondria, others affect mitochondria-associated organelles [20] and induce or facilitate mitochondrial membrane permeabilization. Modulators of the B-cell lymphoma protein 2 (Obatoclax, Gossypol, etc), regulators of reactive oxygen species generation (menadione,  $\beta$ -Lapa Chone), retinoids, heat-shock protein inhibitors (Gamitrinibs) natural compounds (Resveratrol, Betulinic acid and  $\alpha$ -tocopheryl succinate etc.) and metabolic inhibitors (Methyl jasmonate, Dichloroacetate etc.) have been used for this purpose [21].

Working principle of metabolic inhibitors based on disturbing of The tricarboxylic acid (TCA) cycle and fatty acid b-oxidation (FAO) metabolism [20].

### 1.2.3.1 Dichloroacetate

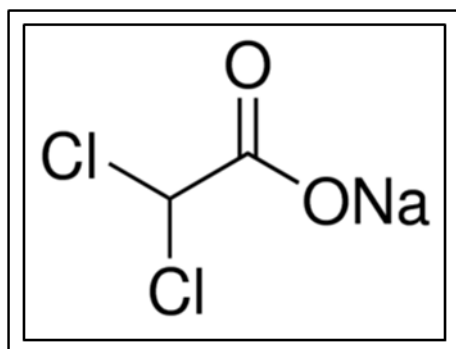


**Figure 2.** Chemical structure of sodium dichloroacetate

Dichloroacetate (DCA) is a small molecule (Figure 2). Nowadays its popularity is that results of its therapeutic effect of cancer illness. Actually dichloroacetate had been for use as a drug for treatment congenital lactic acidosis in the 1960s [22] and its effect on several metabolisms was investigated for diabetes and hypercholesterolemia diseases [23].

For cancer treatment, DCA is used as a tumor suppressor by affecting mitochondrial metabolism (Figure 3). DCA induces the cancer cell to apoptosis by inhibiting pyruvate dehydrogenase kinase which inhibits pyruvate dehydrogenase (PDH), reverses cancer cell abnormal metabolism from glycolysis to glucose oxidation. PDH provides conversion of pyruvate to acetyl-CoA, promoting oxidative phosphorylation (OXPHOS). Thus, (DCA) induces apoptosis, decreases proliferation, and inhibits tumor growth. Therefore, the membrane potential of tumor cell mitochondria turns to the level of normal cell's one owing to increasing glucose oxidation which is promoted by DCA [24] without affecting the mitochondria of non-cancerous cells.



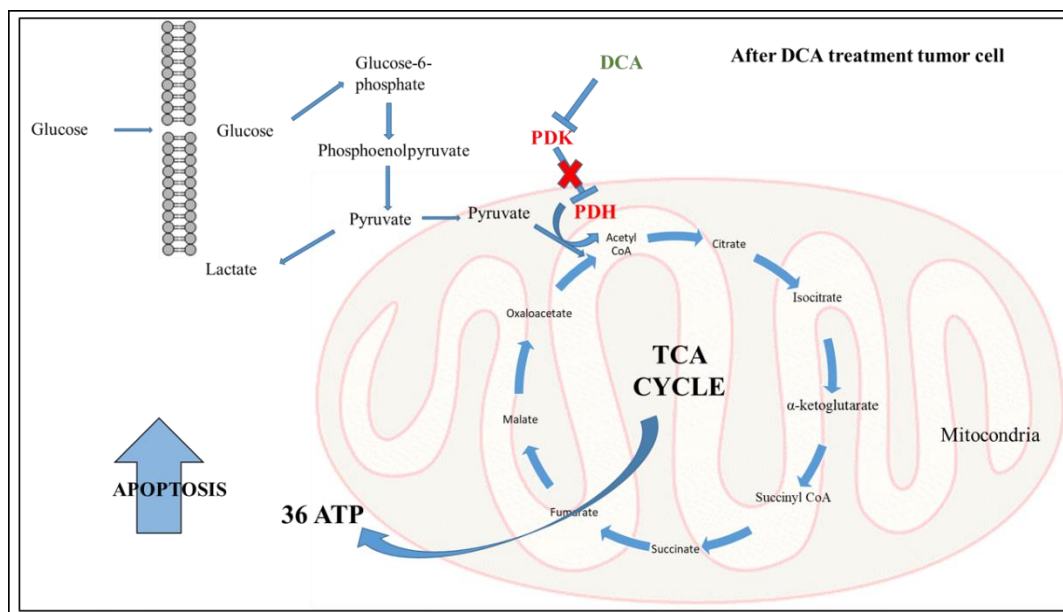


**Figure 3.** Scheme of effect of dichloroacetate on mitochondrial dysfunction

Although DCA used for mitochondrial targeted cancer therapy, its mitochondrial uptake is low because of negative charge [24]. To increase its accumulation into mitochondria, it is modified with lipophilic phosphonium cations. Lipophilic phosphonium cations can cross the mitochondrial inner membrane without help of ionophores. Tetraphenylphosphonium cation and triphenylphosphonium cation are used for this purpose [25].

Another treatment approach for cancer treatment is hyperthermia. The origin of hyperthermia is “overheating” in Greek [26].

Hyperthermia is an unusual high body temperature. The reason of hyperthermia may be an infection, or by exposure to heat. According to this definition, hyperthermia can be perceived negatively, however it is a new tool for cancer treatment. Hyperthermia treatment based on exposing to high temperatures to damage and kill cancer cells or making cancer cells more sensitive to the effects of radiation and certain anticancer drugs [27]. Hyperthermia treatment could not be used as single therapy methods, it should be supported by drug or radiotherapy treatments [28]. Historically, heat therapy was used for breast cancer treatment about five thousand years ago [26].

Hyperthermia treatment is classified external and internal treatment. For external hyperthermia treatment as microwave, ultrasound, radio frequency (RF) can be used as heat source. Unfortunately, all of these methods have some limitations. Microwave hyperthermia is not enough for deep-seated tumors because its penetration capability is low. Despite the higher penetration capability of ultrasound technique than microwave treatment, high energy absorption of the bone and liquid-containing organs and an excessive reflection from the cavities filled with air are disadvantages of the technique. Limitation of RF capacitance hyperthermia is that both tumor and healthy cells are effected in the same ways. RF probe hyperthermia has low penetration and a limited accuracy of localization capability. For internal hyperthermia, nanoparticles can be used as heat source, on the other hand, this type treatment provides a uniform heating of deeply situated tumors with relatively good targeting [29].

#### **1.2.4 Nanotechnology and Cancer**

Nanotechnology helps to overcome the present problem of cancer therapy and diagnosis. Drug or imaging agent conjugated nanoparticles which have multifunctional properties, are prepared for this aim. These properties, such as magnetism, surface plasmon and feasible surface etc., make them superior to single drug or imaging molecules for cancer therapy and diagnosis. Especially drug delivery and detection systems have been developed.

##### **1.2.4.1 Drug delivery**

Basic drawback of today's chemotherapeutic drugs is their low bioavailability to a tumor cell and low differential toxicity toward the tumor cell. Researchers have designed new systems by conjugating drug and targeting molecule to nanoparticles that are addressed directly to tumor cell [12].

According to Prabakaran at all study [30], cell viability of doxorubicin (DOX) is higher when it is conjugated to polyethylene coated, folate modified gold nanoparticles than free DOX molecule. Polymeric particles can also be used for this aim.

Deoxycholate conjugated heparin nanoparticles [31], 4-(2-aminoethyl) and benzenesulfonyl fluoride hydrochloride modified poly-L-glutamic acid nanostructures are two examples of polymeric drug delivery tools. [32]. Camptothecin is another anticancer drug. Laemthong at al., developed poly( $\epsilon$ -caprolactone)(PCL) polymer coated camptothecin nanorods for breast cancer treatment. They reported that nanostructured of camptothecin derivatives are more efficient than molecular types. For increasing efficiency and decreasing toxicity, they used poly( $\epsilon$ -caprolactone) as coating materials. For the targeting purpose, they used antibody (Trastuzumab) which is specific breast cancer cells. On the other hand, they claimed that camptothecin has some side effect such as renal failure, diarrhea and hepatic toxicity [33]. Additionally Beak at al, used folate conjugated nanoparticles for increasing bioavailability of paclitaxel and curcumin which are anticancer drug [34]. Low availability and solubility are important drawbacks of paclitaxel [35].

#### **1.2.4.2 Imaging or detection system**

Plasmonic nanoparticles such as gold, silver nanoparticles, quantum dots are used for designing diagnostic system. Especially these particles increase the sensitivity of surface enhanced raman spectroscopy [36] or fluorescence spectroscopy [37] methods. Magnetic resonance imaging (MRI) is another popular detection technique. It is useful for examination cellular and nonvascular imaging and more favourable than other methods such as computerized axial tomography (CAT), positron emission tomography (PET), and single-photon-emission computed tomography (SPECT) Because radioactive agent and ionizing radiation are not required for MRI [33]. For tumor detection, the efficiency of magnetic resonance imaging (MRI) is increased by using nanoparticles[12]. Specially Gd-based nanoparticles and iron oxide nanoparticles are used as T1 and T2 contrast agents respectively [33].

### **1.2.4.3 Hyperthermia**

Nanotechnology provides a significant contribution to hyperthermia treatment by introducing magnetic nanoparticles that can be driven and accumulated in the desired area of the body. Therefore harmful side effects of hyperthermia such as ionization of the genetic material or absence of selectiveness in microwaves and radiation therapies that affect the surrounding healthy tissues are eliminated. Magnetic hyperthermia treatment includes magnetic nanoparticles which are injected into cancerous tissue and induce local heat when an alternative magnetic field is applied. A temperature increase above 42°C in a tumor cell, due to the transformation of the electromagnetic energy into heat through hysteresis, Néel and Brownian relaxations lead to apoptosis of tumor cell [38-39].

## **1.3 Introduction of Magnetic Nanoparticles**

### **1.3.1 Magnetic Nanoparticles**

Magnetic nanoparticles are extensively used in data storage and biomedical application areas. Higher surface-to-volume ratio makes magnetic nanoparticles more attractive and useful than bulk magnetic materials [40]. Magnetic nanoparticles can be classified as magnetic alloy nanoparticles (Co, Fe) or magnetic metallic nanoparticle (Fe-Co, Fe-Ni, Fe-Pt, Co-Pt, Co-Ni) and metal oxide nanoparticles ( $\text{Fe}_3\text{O}_4$ ,  $\gamma\text{-Fe}_2\text{O}_3$ ,  $\text{NiFe}_2\text{O}_4$ ,  $\text{MnFe}_2\text{O}_4$ ,  $\text{CoFe}_2\text{O}_4$ , NiO,  $\text{Co}_3\text{O}_4$  according to their structure [41].

Metallic magnetic nanoparticles (MMNPs) are more advantageous in terms of information, synthesis and magnetic properties than metal oxide magnetic nanoparticles (MOMNPs). On the other hand, their chemical stability and biocompatibility are lower than MOMNPs. Additionally, higher reactivity for oxidation and pyrophoricity of MMNPs at room temperature render them inappropriate so they are not suitable for hyperthermia application. Although the problem of oxidation is addressed by the incorporation of two or more metals onto iron for the preparation of metallic alloys magnetic nanoparticles (MAMNPs), MOMNPs are still preferred for biomedical applications [41].

### 1.3.2 Iron Oxide Magnetic Nanoparticles (IONPs)

There are eight type iron oxides, but commonly, maghemite ( $\gamma$ -Fe<sub>2</sub>O<sub>3</sub>), hematite ( $\alpha$ -Fe<sub>2</sub>O<sub>3</sub>), magnetite (Fe<sub>3</sub>O<sub>4</sub>) are known. Crystal structure of iron oxide nanoparticles affects their applications. For example, magnetic properties change according to crystal forms. They become desirable for technical and biomedical application because of their unique magnetic, biochemical, and catalytic properties [42].

#### 1.3.2.1 Hematite ( $\alpha$ -Fe<sub>2</sub>O<sub>3</sub>)

Hematite that is oldest iron oxide known types, is most stable iron oxide forms. It used as starting materials for synthesizing magnetite and magnetite types. This type can be called ferric oxide, or iron sesquioxide and its color is red [43]. Its application area is large about catalysts, technology and gas sensors because of its low cost, high resistance to corrosion, and n-type semiconductor properties [42].

The crystal structure of hematite nanoparticles can be defined rhombohedral and hexagonal because of Fe<sup>3+</sup> ions locate two-thirds of the octahedral sites that are boundary determined by the nearly ideal hexagonal close-packed O lattice [42,44].

Their magnetic saturation level and coevircity are lower than other two types, for this reason, they are not eligible for hyperthermia and magnetic applications [43].

#### 1.3.2.2 Magnetite (Fe<sub>3</sub>O<sub>4</sub>)

Magnetite can be called black iron oxide. Its magnetic saturation is higher than other two type iron oxide nanoparticles due to lower oxygen ratio than maghemite ( $\gamma$ -Fe<sub>2</sub>O<sub>3</sub>), hematite ( $\alpha$ -Fe<sub>2</sub>O<sub>3</sub>). Maghemite can easily be obtained by oxidizing magnetite [45].

Magnetite has inverse spinel crystal structure and that is formed polyhedral model with stacking plans. It has a face-centered cubic unit cell according to the position of 32 O<sup>2-</sup> and Fe (III) ions occupy between octahedral and tetrahedral sites, randomly while Fe(II) ions place in octahedral sites [42,43].

### 1.3.2.3 Maghemite ( $\gamma$ - $\text{Fe}_2\text{O}_3$ )

When oxidizing magnetite or heating of other iron oxides, maghemite is obtained. It has a similar spinel structure with magnetite, differently, there are vacancies in the cation sublattice cell of magnetite contains  $21\frac{1}{3}$   $\text{Fe}^{3+}$  ions, 32  $\text{O}^{2-}$  ions, and  $2\frac{1}{3}$  vacancies. While oxygen atoms occur cubic close-packed array, eight Fe ions per a unit cell locate tetrahedral sites and other Fe ions disturb to octahedral sites [42,43].

### 1.3.3 Magnetism of Iron Oxide Nanoparticles

Magnetism of iron oxide nanoparticles depends on spins and aligned of electrons in orbitals. Considering to change magnetic dipole and the net magnetization in the presence and absence of a magnetic field magnetism of iron oxide nanoparticles can be classified diamagnetic, paramagnetic, ferromagnetic, ferrimagnetic, and antiferromagnetic [40,43].

For diamagnetic materials, there is not magnetic dipole in the absence of a magnetic field, but under the external magnetic field the material produces a magnetic dipole that is oriented opposite to that of the applied field. For paramagnetic materials, there are magnetic dipoles but these dipoles are aligned only through the external magnetic field. Ferromagnetic materials have net magnetic dipole moments in the absence of an external magnetic field. For antiferromagnetic and ferrimagnetic materials, the atomic level magnetic dipole moments are similar to those of ferromagnetic materials, but when there is not any magnetic field, adjacent dipole moments exist that are not oriented in parallel and this situation reduces the impact of neighbouring magnetic dipoles within the material [41].

Superparamagnetic material likes ferromagnetic and ferromagnetic materials in case of under the external magnetic field. However, when the external field is removed they do not indicate same magnetic properties. As a result of this properties, they do not attract each other out of the external magnetic field so aggregation does not occur. Size of superparamagnetic particles (about 2-20nm) is smaller than others. Because, for larger or bulk magnetic materials, there are multi-domains to aligning the spin orientation so higher field energy is needed to change the spin of them. In contrast, for smaller particles (2nm-20nm diameter), amount domain walls per a particle decreases

and single domain occur, therefore the requirement of energy for changing spin decreases and these particles exhibit superparamagnetic properties [41].

Super paramagnetic materials are favourable for biomedical applications owing to unique property. This property is that their magnetic behaviour appears only under the magnetic field. The most successful type which has been widely investigated consists of superparamagnetic iron oxide NPs (SPION) [27, 40, 46-49].

#### **1.3.4 Preparation Methods of Iron Oxide Nanoparticles**

The synthesis method of magnetic nanoparticles is important for magnetic properties and behaviours of nanoparticles. Size distribution, shape, particle size, crystal structure, morphology and surface properties can be controlled by changing synthesis methods [27].

There are some difficulties in preparing iron oxide particles, for this reason, choosing method is important for purpose of application. The large surface-to-volume ratio of magnetic iron oxide nanoparticles causes aggregation to reduce surface energies. In addition, the stability and solvent distribution of magnetic nanoparticles depends on their surface properties, so the preparation method has a decisive role in the surface properties of the particles [50]. Anhydrous systems and nonpolar solvents are used to synthesize hydrophobic particles while the aqueous solvent and reaction system are used to obtain hydrophilic particles in the same manner [8].

In addition, the importance of the method that used for preparation, quite significant in controlling the crystal structure, shape and size of the particles. Firstly, the mechanism of particle formation depends on the experimental conditions and the materials used [50]. For instance, when  $\text{Fe}^{2+}$  and  $\text{Fe}^{3+}$  ions are oxidized, maghemite and hematite nanoparticles are formed, while magnetite nanoparticles are obtained under oxygen free conditions. For biomedical application, hematite form is not favourable due to low magnetic properties [51].

Secondly, size and shape of iron oxide nanoparticles affect the efficiency of the application. Magnetic behaviour of iron oxide nanoparticles, generally, is related to size. As the size of the magnetic nanoparticles decreases, the magnetic anisotropy energy per nanoparticle decreases. Anisotropy energy in a characteristic dimension of

magnetic nanoparticles equals thermal energy, which randomly changes the magnetic moment. In addition, the  $M_s$  value varies with the particle size [40].

Third, the magnetic behaviour of iron oxide nanoparticles depends on their shape. The figure has an important role in the formation of magnetic anisotropy. For instance, while spherical nanoparticles do not exhibit net shape anisotropy, rod-shaped nanoparticles have shape anisotropy at the same time crystalline anisotropy. Therefore rod-shaped nanoparticles have higher coercivity [52].

Zeng et al. was reported that cubic shaped magnetic nanoparticles have higher magnetic saturation ( $M_s$ ) than spherical shaped magnetic nanoparticles [53]. Noh et al. explain this situation by using framework program, which analyses disorder of spins. Results of analysis indicate that disorder level is about 4% in cubic MNPs and 8% in spherical MNPs. Lower disorders of cubic shaped particles cause higher  $M_s$ . However, they claim that this comparison should be done by same volume spherical and cubic shaped nanoparticles [40, 54].

There is too many methods for synthesizing magnetic nanoparticles. They can be classified three according to route of the process. First one is physical methods Deposition of the gas phase, laser pyrolysis techniques, Electron beam lithography, laser ablation[8], which is not able to control size and shape. Biological Methods another method. At these type methods, for preparation iron oxide nanoparticles, the microbial enzymes or the phytochemicals of plant are used to reduce iron salts. Also, microorganisms can be used for synthesizing iron oxide nanoparticles such as magneto tactic bacteria or iron reducing bacteria. This type method are compatible with the approach of green chemistry and eco-friend [8].

The final route is chemical preparation methods. These methods are both simple and efficient. Because control of size, shape, composition iron oxide nanoparticles and experimental conditions can be easily changed and controlled. In addition, their low production costs make them favourable in comparison to other routes. The general mechanism of these type methods is based on reducing of  $Fe^{2+}$  and  $Fe^{3+}$  ions with base. The ratio of  $Fe^{2+}$  and  $Fe^{3+}$  ions, pH, surfactants, temperature, pressure and ionic strength etc. are a determinative parameter for preparation [55].

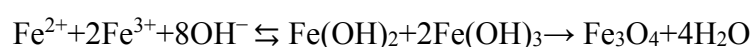
Co-precipitation, thermal decomposition, polyol, hydrothermal or solvothermal methods, microwave assist, electrochemical methods, Sol-gel method,



Aerosol/vapour phase, Sonochemical decomposition, Supercritical fluid method, microemulsion are some of methods that are used at chemistry based route. In the main, first four methods have been applied [56].

#### **1.3.4.1 Co-precipitation Methods**

Co-precipitation methods the handiest procedures in terms of application convenience. It is based on reduction of mixture of ferrous and ferric ions in a 1:2, or 1:3 molar ratio with aqueous base [51, 57]. Aqueous medium synthesis provides obtaining hydrophilic nanoparticles. Reaction of formation of magnetite nanoparticles is given by:



Because pH change is affect ionic strength, size of particles can be control easily. When pH of solution lower than 11, nucleation of iron oxide crystal is favourable, pH of solution higher than 11, growth of iron oxide nucleus is favourable[8]. Generally magnetic nanoparticles have large size distribution when they are prepared this method [8].

By using this method both  $\text{Fe}_2\text{O}_3$  and  $\text{Fe}_3\text{O}_4$  nanoparticle can be synthesized. By applying same method,  $\text{Fe}_3\text{O}_4$  NPs and  $\text{Fe}_2\text{O}_3$  NPs are synthesized under the inert gas and oxygen atmosphere, respectively [50]. Without any surfactant usage Kang. et al and Lin et al synthesized  $\text{Fe}_3\text{O}_4$  nanoparticle with different iron precursors and both of them have 8-10 nm size distribution [51,57]. In addition, generally spherical magnetic nanoparticles with co-precipitation methods, however, surfactant are used, different shape magnetic nanoparticles can be obtained. For instance sodium dodecyl sulphate (SDS) and the time of irradiation with visible light nanoneedle and nanocube shaped iron oxide nanoparticles can be obtained [58].

#### **1.3.4.2 Thermal Decomposition Method**

Generally to obtain magnetite superparamagnetic nanoparticles thermal decomposition method are used. This method is based on high temperature decomposition of organic iron precursors in the presence of organic solvent and

surfactants in high temperature. Surfactant type, decomposition temperature, reflux time and solvent effect shape and size control [59-61].

When compared to co-precipitation method, thermal decomposition method has advantages and disadvantages. Firstly, crystallinity of iron oxide nanoparticles is higher than iron oxide nanoparticles which are synthesized by co-precipitation methods. Because high crystallinity is formed at high temperature [8]. Second advantage is that iron oxide nanoparticles have narrow size distribution. Also because of surfactants they are monodisperse in solution so aggregation level is too low [8].

Third advantage is that controlling of size and shape are easier for thermal decomposition methods. While for co-precipitation methods only pH change and adding rate of precursors can be optimized, there are various parameters for obtaining desirable size and shape options at thermal decomposition. Some of them are that changing or optimizing of iron precursors, temperature, solvent and surfactant types [62]  $\text{Fe}(\text{CO})_5$ , iron oleate,  $\text{Fe}(\text{Cup})_3$  (Cup = N-nitrosophenylhydroxylamine  $\text{Fe}(\text{acac})_3$  (acac = acetylacetonate)),  $\text{Fe}_3(\text{CO})_{12}$  and ferrocene  $\text{Fe}(\text{C}_5\text{H}_5)_2$  are used as iron precursors which are slightly soluble in water [8].

Other parameter is reaction time and heating rate. According to Dewi et al 's study, when heating rate decreased and growth time of reaction (at reflux temperature) decreased, shape of iron oxide nanoparticles changes from spherical to cubic and their size increase about 5 nm to 10 nm [59].

Solvents are another parameters. Their role is significant because for thermal decomposition occurs at high temperature above to generally at 250 °C and this temperature is provided by organic solvents which are have high boiling points. Generally octadecene, benzylether, phenylether, eicosene, hexadecane, di-n-octyl ether, di-n-hexyl ether and squalane are used as a solvent and solvent types effect size of particles [8, 60].

Surfactant and stabilizers are have important role for shape and size controlling. Usually oleic acid, sodium oleate, decanoic acid, and decanoic acid are some of surfactant [60, 61,63,64].

Sun et al. study indicated that spherical iron oxide nanoparticles are obtained when oleylamine as surfactant, benzylether as a solvent are used and decomposition occurs at 298°C [65]. Differently, according to Dewi et al 's study, cubic shaped iron oxide

nanoparticles can be obtained when sodium oleate as surfactant, octadecene as solvent [59].

Aqueous media are required for biomedical applications. Thus, the production of hydrophobic iron oxide nanoparticles is the main disadvantage of this method for biomedical applications. By applying ligand exchange and coating procedure, these particles become hydrophilic. Polyvinylpyrrolidone [66],  $\text{NOBF}_4$  and oxalic acid [59,67] can be used as ligand exchange and coating material.

### 1.3.4.3 Polyol Method

Polyol method is another approach for the synthesis of iron oxide nanoparticles. High dielectric points, capability of solving inorganic materials and high boiling point of polyols provide perfect conditions for the synthesis. The hydrolysis of chelate metal alkoxide complexes at high temperature in solutions of alcohol is main mechanism of this method [56]. In other words polyol is used as a solvent, reducing agents and stabilizer. Mechanism of chelation reaction and metal ferrite nanoparticle formation as a results of the decomposition of the chelate are depicted in .

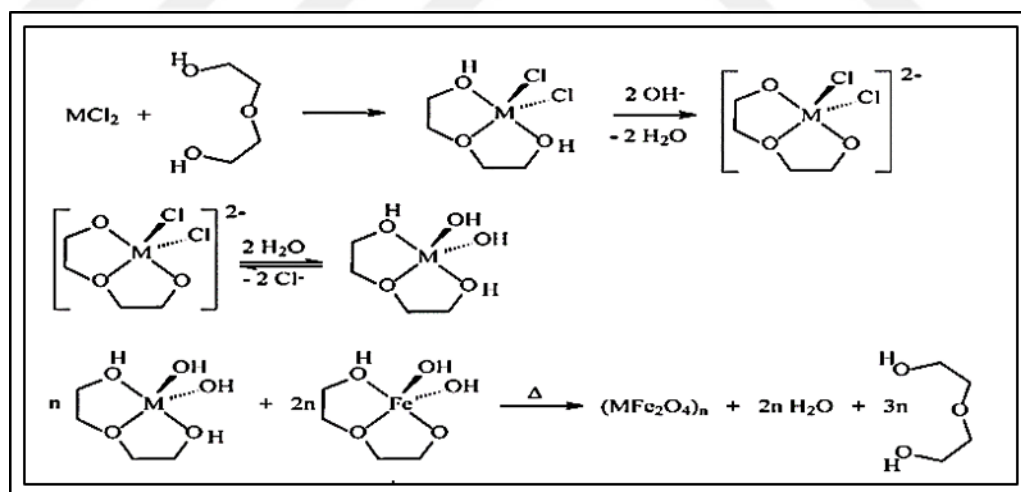


**Figure 4.** Mechanism of polyol method [68].

This method provide non-aggregated nanoparticles, with different size and composition due to controlling to participation kinetically is easy by the same way

thermal-decomposition method. Another advantage of polyol method is that they are stable in aqueous medium due to labile layer of solvent without requiring any surfactants and coating materials [68] so they are suitable for biomedical applications. Diethylene glycol (DEG), triethylene glycol (TEG), tetraethylene glycol (TTEG) are used as solvent and stabilizers. Additionally, study of Hachani et al. indicated that DEG, TREG, TEG are used about 6nm, 10 nm and 13 nm spherical iron oxide nanoparticles can be obtained, respectively [69].

#### **1.3.4.4 Hydrothermal Method**

Hydrothermal method is another method which is used often. For formation nanocrystals high temperature ( $>200^{\circ}\text{C}$ ) and high pressure ( $>2,000$  psi) are required at this method. To achieve these conditions, autoclave is used. The advantages of hydrothermal methods are that high reactivity of the reactants, good crystallization of nanoparticles and simple controlling of product morphology [55]. By using this method various shape such as nanospheres, nanoplates, nanorods, nanocubes, nanorings, nanosheets, and nanowires and size about 1nm to  $\mu\text{m}$ . Additionally different crystal forms can be obtained such as  $\alpha\text{-Fe}_2\text{O}_3$ ,  $\gamma\text{-Fe}_2\text{O}_3$ , and  $\text{Fe}_3\text{O}_4$  NPs [8].

#### **1.3.5 Magnetic Nanoparticle and Biomedical Application**

Magnetic nanoparticles have become unique tool for biomedical applications. Specially, they are used for diagnostic and therapeutic tools for cancer treatments [49]. Drug delivery, imaging, magnetic targeting, and magnetic hyperthermia are some of applications (Figure 5).

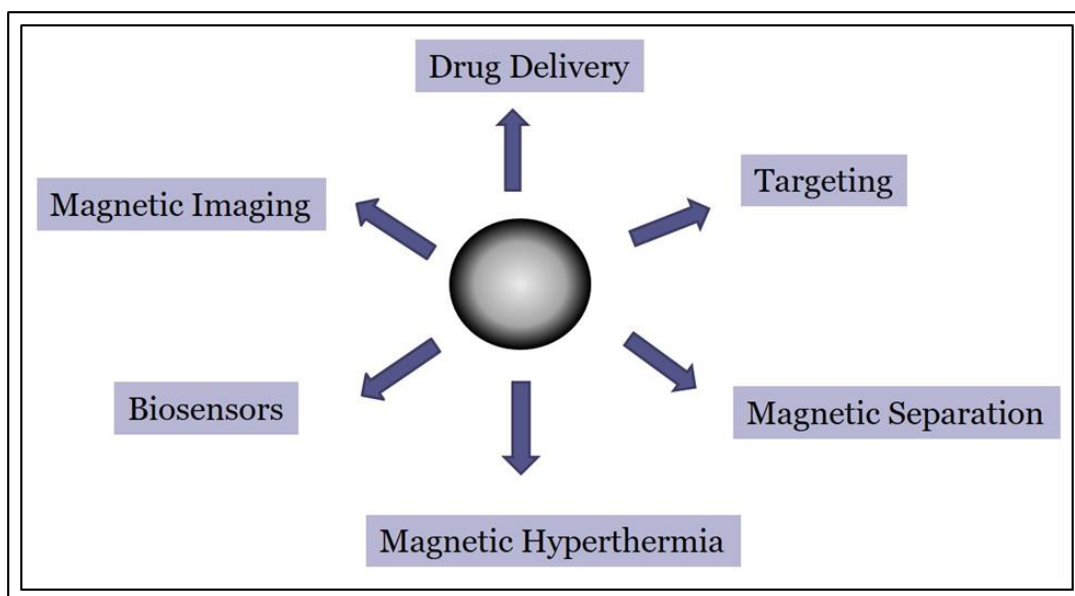


**Figure 5.** Usage of magnetic nanoparticles for biomedical applications

Reason that magnetic nanoparticles more attractive for these type applications is their magnetic properties. Magnetic properties not only provide easiness to experimental procedure in terms of magnetic separation, but also enrich the biomedical applications by allowing multiple approach synchronously [70].

### 1.3.6 Modification of Magnetic Nanoparticles for Biomedical Applications

The crucial factor is magnetic nanoparticles for usage biomedical applications are that keeping stable, increasing their dispersion in aqueous medium, making their surface favourable for functionalization and decreasing their toxicity. Surface modification provides keeping this condition. Also this process protect nanoparticles physically and chemically. For instance, iron oxide nanoparticles, loosing magnetization important drawbacks for this application.  $\text{Fe}_3\text{O}_4$  nanoparticles turn to  $\text{Fe}_2\text{O}_3$  form under the atmospheric oxygen so their magnetisation decrease [8, 49]. For modification, surface coating process is applied. As for coating inorganic material silica, noble metals; for organic coating materials phosphate, carboxylate, sulphonate and phosphonate tartaric, gluconic or dimercaptosuccinic acid, phosphorylcholine and taurine can be used [71].

Coating magnetic nanoparticles with biocompatible polymer is preferable procedure because these polymers increase multifunctionality, colloidal stability and biological activity of magnetic nanoparticles. Generally synthetic and natural biodegradable polymers are used. Some of polymers which are used for this purpose such as gelatine, dextran, polysaccharides, polyethyleneglycol, or chitosan [8].

Another natural biocompatible polymer is heparin. Details of heparin are given below.

### 1.3.6.1 Heparin

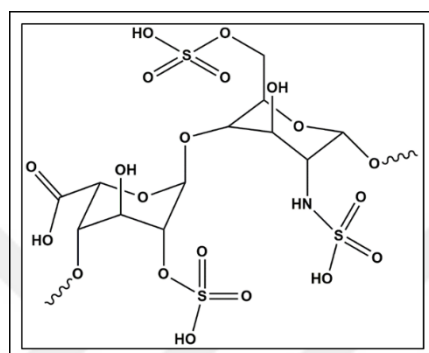


**Figure 6.** Chemical structure of heparin

Heparin (Figure 6) is clinically used as anticoagulant drug. Besides, it is widely used as an anticoagulant coating of blood-contacting material surfaces. Heparin, is a highly sulphated glycosaminoglycan, rich in hydroxyl, carboxyl and sulfo groups [72, 73].

In clinical studies generally low molecular weight heparin molecules are used as drug. When its molecular weight is in between 3,000-30,000 Dalton, it is called low molecular weight heparin [74]. There are various low molecular weight heparin types. Heparin is also used as coating material for theranostic nanoparticles. Studies indicate that negative charge of heparin give opportunity for ionic attachment molecule to nanoparticle surface. As in clinical application, high molecular weight heparin is not desired for working with nanoparticle because it causes agglomeration [72, 73].

Other advantages of heparin for biomedical application are cancer detection and therapy. For detection studies, their derivatives can be used as optical imaging agents. In addition, heparin has anticancer activity through anti-angiogenesis process. As the

number of deoxycholate group on heparin is increases, the capability of tumor growth inhibition is increases as well [31].

## **1.4 Hyperthermia**

Hyperthermia is used one of treatment method. At previous part, some of detail have been given hyperthermia treatment types. Briefly, when microwave, ultrasound etc. are used, it is called external hyperthermia. This type is used now clinically. The hyperthermia treatment basically divided in two parts external hyperthermia and internal hyperthermia. According to The National Cancer Institute (NCI), when small tumor tissue are exposed to high temperature, it is called local hyperthermia; when all organs or body part are exposed to heat, it is called regional hyperthermia; at metastatic cancer case, high temperature are applied to all body and it is called whole body hyperthermia treatment [75].

### **1.4.1 Magnetic Hyperthermia**

Magnetic hyperthermia can be described as injecting cancer cells into magnetic nanoparticles, producing magnetic nanoparticles under an alternating magnetic field, and increasing the temperature to cause these cancer cells to become apoptotic [38]. Due to providing homogenous temperature distribution, magnetic hyperthermia approach is more favourable than other hyperthermia treatment approach [76]. For aim of cancer treatment, first trials were made at 1960s and differently they used H-field dominant system instead of E-field dominant system and application were treated to ex-vivo tissue samples. Unfortunately, due to lack of in vivo tissue application, controlling temperature increasing and observation change volume of solid tumor, these studies were insufficient. Firstly, Jordan et al. ,by applying H-field amplitude, they succeeded calculation of specific absorption rate (SAR) at 1993 [77].

## **1.4.2 Mechanism of Magnetic Hyperthermia**

Generally, magnetic materials generate heat under the alternative magnetic field according to independent four different mechanism. These mechanisms are eddy currents, hysteresis loss, and relaxations mechanisms.

### **1.4.2.1 Eddy Current**

Heat is produced via resistant which occur result of magnetic flux changing which induce eddy current. Eddy current happens only bulk materials which are at centimetre scale and it is negligible for nanometre scale materials [78]. For this reason this type heat generation is not suitable for biomedical application [27].

### **1.4.2.2 Hysteresis losses**

Magnetisation of magnetic nanomaterial undergoes a closed loop during reversal of orientation under the external magnetic field and this loop can be called: the hysteresis loop. The area within the loop indicates that energy delivered in the form of heat to the material of the magnetic particles during reversal of magnetisation. The coupling of the atomic magnetic moments to the crystal lattice cause to convention of energy to heat [46].

Hysteresis curve is given at Figure 7. Hysteresis loop depends on saturation magnetisation( $M_s$ ), remanent magnetisation ( $M_r$ ), The coercivity or coercive field ( $H_c$ ) [76]. The maximum magnetization value of magnetic nanoparticles under the external magnetic field is called saturation magnetisation. Remanent magnetisation is defined as magnetisation which remain after removing external magnetic field, coercivity is that intensity of magnetic field that force to magnetisation zero [40].



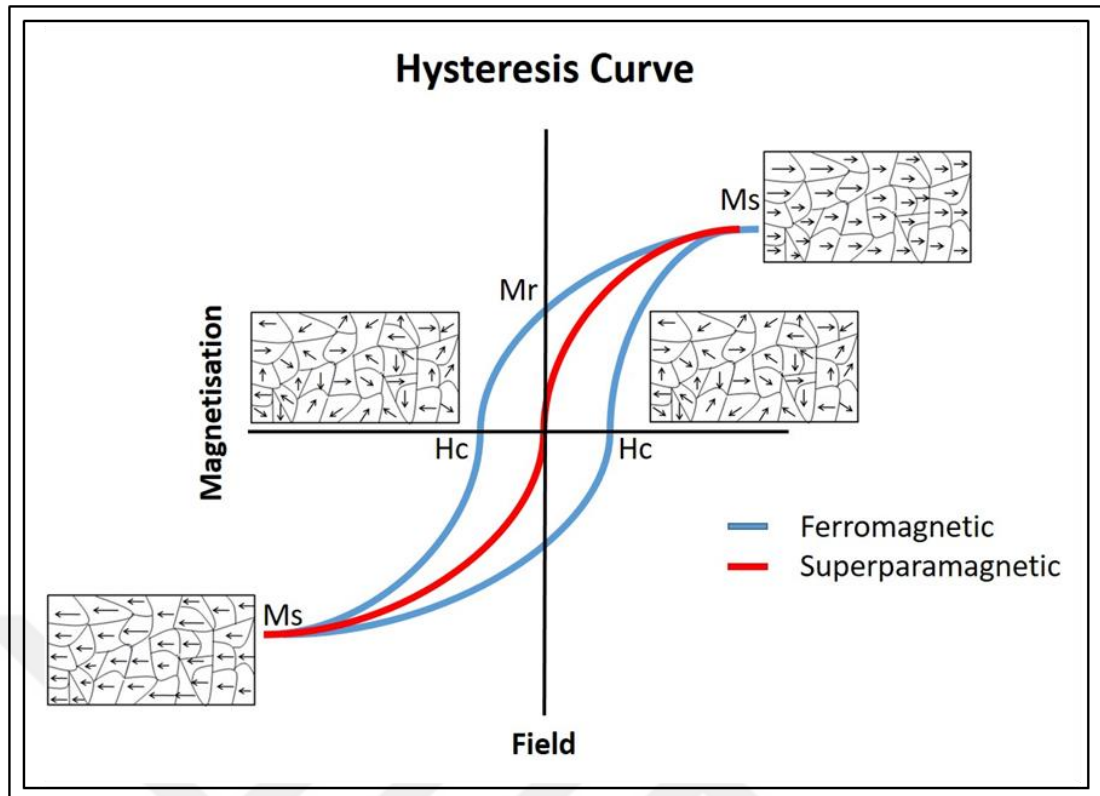


**Figure 7.** Hysteresis curve of superparamagnetic (red line) and paramagnetic (blue line) nanoparticle under the magnetic field

Size of magnetic nanoparticles affects their coercivity. With the particle size decreases, coercivity increases and that after achieving maximum, it tends to be zero. As a results of particle size and coercivity relation, magnetization of nanoparticles can be classified Single domain, multidomain and superparamagnetism. Size of multidomain particles are higher than others and magnetization changes through domain walls motion. For single domain particles, diameters of particles below the critical value, they become single domain. Due to their magnetization change only spin rotation and without any wall moving, they have high coercivity. But as the diameter of particle decrease below  $D_c$ , the thermal effects cause the decreasing of coercivity. For the superparamagnetism, diameters of particles decreases under  $D_p$  and coercivity becomes zero [27].

### 1.4.2.3 Relaxation mechanism

Final mechanism is relaxation mechanism. Small nanoparticle generate the heat according to these mechanisms. According to these mechanism, due to decreasing particle size, energy barrier for magnetization reversal decreases and thermal fluctuation cause the relaxation [46]. Neel relaxation appears when the atomic magnetic moment is rotated through same direction with external magnetic field. Another relaxation mechanism is Brownian relaxation. Brownian relaxation appears through the friction which occurs as a results of the rotation of the particle itself in the carrier liquid [79].

The viscosity of medium affects Brownian relaxation. When viscosity is high, motion of nanoparticles slow down and all particle rotation is prevented. For this reason Brownian relaxation becomes minimum in vivo experiments because of high viscosity of cell medium. Generating of heat by Neel relaxation is dominant in these type application [80].

### 1.4.3 Specific Absorption Rate (SAR)

The amount of inductive heating is important for clinical application. Because the amount of heat released and the amount of exposed nanoparticles must be at the optimum level against side effects. For this reason, the specific absorption rate (SAR) is calculated. Specific absorption rate (SAR) is defined as the amount of heat released by a unit weight of the material per unit time during exposure to alternating magnetic field. The unit of SAR is watts per gram.

$c$  is the specific heat capacity, and  $\Delta T$  is the temperature rise in normal tissue during the exposure time interval ( $\Delta t$ ) [81].

In inductive RF generators are used for SAR value measurement. Generally classical type inductive machine are used for SAR measurement. Generator, coil, isolation material and thermometer are component of this type devices. Changing of temperature of magnetic fluid after applied alternating magnetic field is recorded and SAR value is calculated [82]. There are significant points to consider when designing the device. After the magnetic field is applied, the coil heats up. In order to protect the

sample from this heat, an isolation and cooling system should be installed between the sample and coil.

#### **1.4.4 Applications of Magnetic Hyperthermia**

The SAR value is directly proportional to the height of the applied magnetic field. For this reason, as the magnetic field strength increases, the SAR value increases. But to obtain high SAR value, high frequency and excessive magnetic field should not be applied. Because high frequency and excessive magnetic field may cause uncontrolled heating through eddy current in non-magnetic tissue. For clinical studies, to prevent this uncontrolled heating, magnetic field and frequency should be  $4,85 \times 10^8 \text{ Am}^{-1} \text{ s}^{-1}$  and 100-150 kHz, respectively [47].

Many research groups work between these intervals, but the results are not likely to be appropriate for clinical practice. Generally, magnetic nanoparticles are used at high concentration to obtain high SAR values of this magnetic field and frequency. For this reason, the toxic effect of nanoparticles increases and the efficiency of the treatment decreases. For this reason, the most important goal in studies should be to achieve the temperature increase necessary for effective hyperthermia treatment, using particles with the lowest magnetic field [79].

In addition, one of the important factors for hyperthermia studies is which kind of magnetic particle is used. First, the use of super paramagnetic particles may be more convenient for hyperthermia treatment. Because their magnetic behaviours are minimized in the absence of magnetic field so their agglomeration level is minimized at that time. These properties make them suitable for usage in capillary vessels due to prevent embolization problem. On the other hand, usage of ferrimagnetic or ferromagnetic nanoparticles have advantage in terms of heating efficiency for hyperthermia, despite their high agglomeration level. This agglomeration problem affects the use of particles in vivo work in the negative [80] By modifying their surface, agglomeration level can be decreased [71].

The clinical trials have been made since 1993. In 2007, Jordan et al. set up their experiment with 14 patient who suffered from glioblastoma multiform (brain tumor). They combined external radiotherapy and hyperthermia therapy. For hyperthermia

treatment, they used aminosilane modified iron oxide nanoparticles (core size 15nm) that are dispersed in water and concentrated  $112 \text{ mg Fe mL}^{-1}$ . After injected 0.1 to 0.7 mL of the magnetic fluid each tumor, they applied a magnetic field of 3.8 to 13.5  $\text{kA m}^{-1}$  alternating at 100 kHz to patients. According to their study, results were hopeful. Although tumors could not be ended exactly therapy were tolerated by patients. To achieve evaluation exact clinical outcomes, they started phase 2 trials with 65 patients [83, 84].

### **1.5 Purpose of This Study**

In this study, we aimed to developed multifunctional tool cancer treatment that includes both magnetic hyperthermia, targeting and drug cure. For this aim, magnetic nanoparticles which have different shape and size have been synthesized. To make them biocompatible, their surface have been coated with heparin. Dichloroacetate is used as a drug for mitochondrial cancer therapy for years in medicine. To increase the uptake in to the mitochondria, drug molecules were modified with triphenylphosphonium ions. Modified drug molecules were also embedded in heparin layer. 2-deoxy-D-glucose that has been used as a targeting agent, were attached to heparin surface. For biological trials, HepG2 cell lines was used. After determining IC50 values cytotoxicity experiments were done. For hyperthermia studies, inductive heating device was designed and heating efficiency of spherical magnetite nanoparticles was examined.

## CHAPTER 2

### EXPERIMENTAL

#### 2.1 Instrumentation

##### 2.1.1 Infrared Spectrophotometry

Alpha, Bruker Fourier Transform Spectroscopy was used for characterization of surface modification of magnetic nanoparticles. For sample holding procedure, pellet preparation method was used. Pellets were prepared by using KBr.

##### 2.1.2 UV-vis Spectrophotometry

Qualitative and quantitative characterization of TPP-DCA at 190-500 nm were held on by T80+ UV-VIS PG Instruments. These measurements were done by using quartz cuvette.

##### 2.1.3 X-Ray Diffraction

Rigaku Mini-Flex X-ray powder Diffractometer (XRD) source of Cu-K $\alpha$  line ( $\lambda=1,54056 \text{ \AA}$ ) was used.

##### 2.1.4 Nuclear Magnetic Resonance Spectrometry

Nuclear magnetic resonance ( $^1\text{H}$  NMR) spectra were taken from a Bruker Instrument Avance Series-Spectrospin DPX-400 Ultra shield instrument in  $\text{CDCl}_3$ .

### **2.1.5 Thermal Gravimetric Analyser**

For characterization of heparin coated iron oxide nanoparticles Perkin Elmer STA 6000 device used as a thermo gravimetric analyser.

### **2.1.6 Zeta Potential Measurements**

Potential of surface of naked, acid treated naked, heparin coated, TPP-DCA modified heparin coated and TPP-DCA embedded heparin coated modified iron oxide nanoparticles were measured by Malvern Nano ZS90 device.

### **2.1.7 Transmission Electron Microscopy**

JEOL 2100 F Transmission Emission Microscopy (TEM operated at 200 kV, at METU Central Laboratory, was used for morphologic characterization of nanoparticles. 200 mesh holey carbon coated grid and 200 mesh lacey carbon coated grid were used for analysis. Samples were dried on the grid at room temperature 24 hours before performing TEM analysis. Unless otherwise is stated, regular dropping technique was used in sample preparation.

### **2.1.8 Scanning Electron Microscopy**

In the characterization of iron oxide nanoparticles, JEOL JSM-6400 model scanning electron microscope was used.

### **2.1.9 VSM**

Magnetic saturation measurements was done Cryogenic Limited PPMS in METU Central Laboratory

### **2.1.10 Reactor**

Hydrothermal Synthesis was done utilizing PARR<sup>®</sup> 5500 model reactor

### 2.1.11 AC Generator

A homemade generator that was designed and prepared in our laboratory was used.

## 2.2 Chemicals and Reagents

### 2.2.1 Preparation of Spherical Shape Fe<sub>3</sub>O<sub>4</sub> NPs

Ferrous sulphate (FeSO<sub>4</sub>·7H<sub>2</sub>O, ≥99%, SIGMA-ALDRICH), Ferric sulphate hydrate (Fe<sub>2</sub>(SO<sub>4</sub>)<sub>3</sub>·xH<sub>2</sub>O, ≥97%, SIGMA-ALDRICH), Ammonium hydroxide solution (28% NH<sub>3</sub> in H<sub>2</sub>O, SIGMA-ALDRICH).

### 2.2.2 Preparation of Flower Shape Fe<sub>2</sub>O<sub>3</sub> NPs

Ferric chloride hexahydrate (FeCl<sub>3</sub>·6H<sub>2</sub>O, ≥97%, SIGMA-ALDRICH), Ferrous chloride tetrahydrate (FeCl<sub>2</sub>·4H<sub>2</sub>O, ≥99%, SIGMA-ALDRICH), Triethylene Glycol, ≥99%, SIGMA-ALDRICH), Sodium hydroxide (NaOH, puriss., meets analytical specification of Ph. Eur., BP, NF, E524, 98-100.5%, pellets, SIGMA-ALDRICH), Diethanolamine (HOCH<sub>2</sub>CH<sub>2</sub>)<sub>2</sub>NH<sub>2</sub>, 98.5%, ALDRICH), Ferric nitrate nonahydrate (Fe(NO<sub>3</sub>)<sub>3</sub>·9H<sub>2</sub>O, ≥98%, SIGMA-ALDRICH), Nitric acid (HNO<sub>3</sub>, ACS reagent, 70%, SIGMA-ALDRICH), Diethyl ether ((C<sub>2</sub>H<sub>5</sub>)<sub>2</sub>O, ≥99.7%, MERCK MILLIPORE), Acetone (CH<sub>3</sub>COCH<sub>3</sub>, ≥99.7%, CARLO ERBA REAGENTS)

### 2.2.3 Synthesizing of Iron Oxide Nanoparticles by Hydrothermal Method

Ferrous chloride tetrahydrate (FeCl<sub>2</sub>·4H<sub>2</sub>O, ≥99%, SIGMA-ALDRICH), Sodium dodecyl sulfate (CH<sub>3</sub>(CH<sub>2</sub>)<sub>11</sub>OSO<sub>3</sub>Na, ACS reagent, ≥99.0%, SIGMA-ALDRICH), Sodium tetrahydroborate (NaBH<sub>4</sub>, powder, ≥98.0%, SIGMA-ALDRICH).

### 2.2.4 Preparation of Cubic Shape Fe<sub>2.3</sub>O<sub>4</sub> NPs

Iron(III)acetylacetonate (Fe(acac)<sub>3</sub>, ≥97%, SIGMA-ALDRICH), oleic acid (CH<sub>3</sub>(CH<sub>2</sub>)<sub>7</sub>CH=CH(CH<sub>2</sub>)<sub>7</sub>COOH, ≥97%, SIGMA-ALDRICH), benzyl ether

((C<sub>6</sub>H<sub>5</sub>CH<sub>2</sub>)<sub>2</sub>O), 97%, SIGMA-ALDRICH), Acetone (C<sub>3</sub>H<sub>6</sub>O, for analysis MERCK), Ethanol (C<sub>2</sub>H<sub>5</sub>OH Ethanol absolute suitable for use as an excipient, MERCK), Chloroform (CHCl<sub>3</sub>, ACS, ISO, Reag. Ph Eur., MERCK), Undecanoic acid (C<sub>11</sub>H<sub>22</sub>O<sub>2</sub>, ≥99.0% FCC, FG, SAFC), Sodium oleate (CH<sub>3</sub>(CH<sub>2</sub>)<sub>7</sub>CH=CH(CH<sub>2</sub>)<sub>7</sub>COONa, ≥82%, SIGMA-ALDRICH), Ferric chloride hexahydrate (FeCl<sub>3</sub>.6H<sub>2</sub>O, ≥97%, SIGMA-ALDRICH), Octadecene (C<sub>18</sub>H<sub>36</sub>, ≥95%, FLUKA), Hexane (CH<sub>3</sub>(CH<sub>2</sub>)<sub>4</sub>CH<sub>3</sub>, ≥97%, SIGMA-ALDRICH), Toluene (C<sub>6</sub>H<sub>5</sub>CH<sub>3</sub>, ≥98% anhydrous, SIGMA-ALDRICH), Polyvinylpyrrolidone ((C<sub>6</sub>H<sub>9</sub>NO)<sub>n</sub>, average mol wt 10,000, SIGMA-ALDRICH), N, N-Dimethylformamide ((DMF), (HCON(CH<sub>3</sub>)), 2,99.8% SIGMA-ALDRICH), Dichloromethane (CH<sub>2</sub> Cl<sub>2</sub>, LiChrosolv®, MERCK), Diethyl ether ((C<sub>2</sub> H<sub>5</sub>)<sub>2</sub> O for analysis EMSURE®, MERCK MILLIPORE).

### **2.2.5 Synthesis of (3-hydroxypropyl)triphenylphosphonium-(TPP-(CH<sub>2</sub>)<sub>3</sub>-OH)**

3-Bromo-1-propanol (Br(CH<sub>2</sub>)<sub>3</sub>OH, ≥98% anhydrous, SIGMA-ALDRICH), Triphenylphosphine ((C<sub>6</sub>H<sub>5</sub>)<sub>3</sub>P, 99%, ReagentPlus®, SIGMA-ALDRICH), Dichloromethane (CH<sub>2</sub> Cl<sub>2</sub>, LiChrosolv®, MERCK), Diethyl ether ((C<sub>2</sub> H<sub>5</sub>)<sub>2</sub> O for analysis EMSURE®, MERCK MILLIPORE).

### **2.2.6 Synthesis of (3-(2,2-dichloroacetoxy)propyl) triphenylphosphonium (TPP-DCA) by Using Dichloroacetic anhydride**

Dichloroacetic anhydride (C<sub>4</sub> H<sub>2</sub> Cl<sub>4</sub> O<sub>3</sub>, for synthesis, END MILLIPORE), Methanol (CH<sub>4</sub> O, hypergrade for LC-MS LiChrosolv®, MERCK MILLIPORE), Dichloromethane (CH<sub>2</sub> Cl<sub>2</sub>, LiChrosolv®, MERCK), Diethyl ether ((C<sub>2</sub> H<sub>5</sub>)<sub>2</sub> O for analysis EMSURE®, MERCK MILLIPORE), Acetone (CH<sub>3</sub>COCH<sub>3</sub>, ≥99.7%, CARLO ERBA REAGENTS), Ethanol (C<sub>2</sub>H<sub>5</sub>OH Ethanol absolute suitable for use as an excipient, MERCK), Ethyl acetate (CH<sub>3</sub> COOC<sub>2</sub> H<sub>5</sub>, LiChrosolv®MERCK), Silica Gel 60( (0.063-0.200 Mm) for Column Chromatography, MERCK MILLIPORE) Silica gel 60 HF254 (MERCK), Aluminum TLC plate, silica gel coated with fluorescent indicator F254 (MERCK MILLIPORE).



### **2.2.7 Synthesis of (3-(2,2-dichloroacetoxy)propyl) triphenylphosphonium (TPP-DCA) by Using Dichloroacetylchloride**

Dichloroacetyl chloride ( $\text{Cl}_2\text{CHCOCl}$ , 98% SIGMA-ALDRICH), Methanol ( $\text{CH}_3\text{OH}$ , hypergrade for LC-MS LiChrosolv®, MERCK MILLIPORE), Dichloromethane ( $\text{CH}_2\text{Cl}_2$ , LiChrosolv®, MERCK), Ethanol ( $\text{C}_2\text{H}_5\text{OH}$  Ethanol absolute suitable for use as an excipient, MERCK), Ethyl acetate ( $\text{CH}_3\text{COOC}_2\text{H}_5$ , LiChrosolv® MERCK), Silica Gel 60 ((0.063-0.200 Mm) for Column Chromatography, MERCK MILLIPORE), Silica gel 60 HF254 (MERCK), Aluminum TLC plate, silica gel coated with fluorescent indicator F254 (MERCK MILLIPORE).

### **2.2.8 Surface Modification of Nanoparticles: Coating by Heparin, Attaching TPP-DCA to Heparin Coated Iron Oxide surface and Embedding TPP-DCA into Heparin Layer**

Enoxaparin (CLAXENE®), Sodium hydroxide (NaOH, puriss., meets analytical specification of Ph. Eur., BP, NF, E524, 98-100.5%, pellets, SIGMA-ALDRICH), Nitric acid ( $\text{HNO}_3$  ACS reagent, 70% SIGMA-ALDRICH).

### **2.2.9 Attaching 2-deoxy-D-glucose**

1-Ethyl-3-(3-dimethyl aminopropyl)carbodiimide ((EDC), Pierce Chemical Co, USA), N-Hydroxysuccinimide ((NHS), 98% SIGMA-ALDRICH), D-Glucosamine hydrochloride ( $\text{C}_6\text{H}_{13}\text{NO}_5 \cdot \text{HCl}$ , 98%, ACROS ORGANICS).

## **2.3 Biological Experiments**

### **2.3.1 Cell Growth**

HepG2 Cell Line ATCC (American Type Culture Collection), Dulbecco's Modified Eagle Medium (Biowest), HEPES (Biowest, Cat.No: L0065) Fetal Bovine Serum (FBS, Biowest), Penicillin-Streptomycin (Pen-Step, Biological Industries), Trypsin

(Biological Industries ), Phosphate Buffer Saline (PBS Biological Industries ), Cell Proliferation Kit-XTT based, Biological Industries).

## 2.4 Procedures

### 2.4.1 Preparation Magnetic Nanoparticles

#### 2.4.1.1 Preparation Spherical Shape $\text{Fe}_3\text{O}_4$ NPs



**Figure 8.** Image of experimental set up of co-precipitation methods

Magnetic  $\text{Fe}_3\text{O}_4$  nanoparticles with an average particle size of 5–15 nm were synthesized by a chemical co-precipitation method in a nitrogen atmosphere (Figure 8). Briefly, 2.36 g  $\text{FeSO}_4 \cdot 7\text{H}_2\text{O}$  and 3.00 g  $\text{Fe}_2(\text{SO}_4)_3$  were dissolved in 150.0 mL deionized water, which was preheated to  $80^\circ\text{C}$  before the co-precipitation reaction. 10 mL ammonia solution (28 wt %) was quickly added to this mixture and vigorously stirred (700 rpm) for 30 min. The resulting black precipitate was collected with the help of a magnet and thoroughly washed several times with deionized water [85].

#### 2.4.1.2 Preparation Flower Shape Fe<sub>2</sub>O<sub>3</sub> NPs

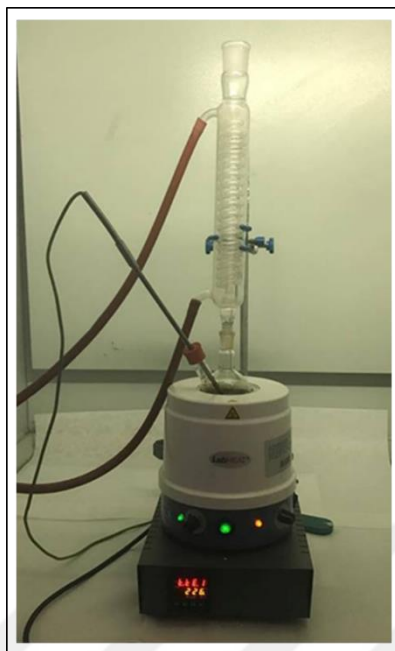


**Figure 9.** Image of experimental set up of polyol method

Flower shape Fe<sub>2</sub>O<sub>3</sub> NPs were synthesized by polyol method [86]. Experimental set up is given at Figure 9. 1 mmol FeCl<sub>3</sub>.6H<sub>2</sub>O and 1mmol FeCl<sub>2</sub>.4H<sub>2</sub>O were dissolved in 10 g TEG + 10 g diethanolamine mixture (DEA). 0.16 g NaOH prepared in 5 g TEG + 5 g DEA mixture was added to the previous mixture while stirring at room temperature. After 1hour stirring, the temperature was raised to 220 °C. The polyol composition and the reflux time were optimized. These are indicated at Table 3. After cooling to room temperature, the black precipitate formed was collected using a magnet. Following the washing process with 1:1 ethanol ethyl acetate mixture, the precipitate was treated with 10 % nitric acid to remove possible iron hydroxides. After magnetic separation, particles were added into 5.0 mL water solution containing 2.05 g Fe(NO<sub>3</sub>)<sub>3</sub> under stirring and heated to 80 °C for 45 min. At the final step, the black color of the precipitate was turned into brown. The precipitate was collected by a magnet, treated by 10 % nitric acid and washed with acetone and diethyl ether. After washing procedure flower shape Fe<sub>2</sub>O<sub>3</sub> NPs were dispersed in deionized water. All optimization studies are given at Table 1

**Table 1.** List of different parameters of synthesizing flower shaped iron oxide nanoparticles.

Experiment Number	Polyol Composition (TEG:DEA)(w:w)	Heating Slope (from 25°C to 220 °C)	Reflux time (220 °C)
1.a	1:0	1 °C/min	2.0 h
2.b	1:1	1 °C/min	2.0 h
3.c	1:1	1 °C/min	0.5 h
4.e	1:1	1 °C/min	1.0 h

### 2.4.1.3 Synthesizing Iron Oxide Nanoparticles by Hydrothermal Method

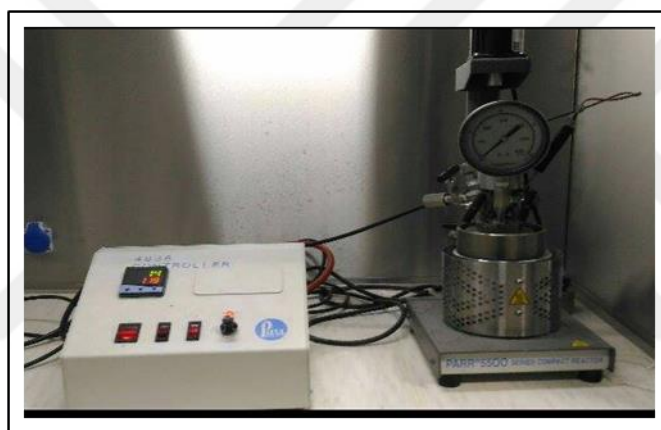


**Figure 10.** Image of experimental set up of hydrothermal method

Hydrothermal method of Liu et. al was used [87]. Reaction was made in reactor (Figure 10). Briefly, 1 mmol of  $\text{FeCl}_2 \cdot 4\text{H}_2\text{O}$ , 1 mmol of sodium dodecyl sulphate and 10.0 mL of water were added to a 5 mg/mL aqueous sodium borohydride solution. The colour of the solution becomes black. This mixture stirred slowly about 5 h in the reactor at 140 °C under 5 bars pressure. The pink-orange precipitate formed was collected by using a magnet and washed three times with water

#### 2.4.1.4 . Preparation of Hydrophilic Cube Shape Fe<sub>3</sub>O<sub>4</sub> NPs



**Figure 11.** Image of experimental set up of thermal decomposition method

##### 2.4.1.4.1 Synthesis of Cubic Shape Iron Oxide Nanoparticles by Using Oleic Acid and Undecanoic Acid as Surfactant

Thermal decomposition method was used to synthesize cube shape Fe<sub>3</sub>O<sub>4</sub> NPs [63]. 0.5 mmol Fe(acac)<sub>3</sub>, 2 mmol oleic acid and 12.5 mL benzyl ether were degassed for 1 h at 60 °C under N<sub>2</sub> atmosphere in three necked round-bottom flask (Figure 11). Then the temperature was increased to 200 °C at a rate of 4 °C/min. The mixture was stirred at this temperature about 2.5 h and then the temperature was raised to reflux temperature (280 °C) at a heating rate of 2 °C/min. After 1 hour stirring at reflux temperature, the black precipitate was washed with acetone- ethanol mixture and dispersed in chloroform. Table 2,A [88].

Oleic acid used in the thermal decomposition method described above was replaced with undecanoic acid. Under this condition duration of refluxing and heating period were optimized, as displayed in Table 2, (B, C, D, E, F)

**Table 2.** Optimization studies of thermal decomposition method. Surfactant is undecanoic acid.

Experiment Name	Initial Heating Heating Time	Reflux Time	Amount of Acid
A	2,5 h	60 min	2.0 mmol
B	2.0 h	60 min	2.0 mmol
C	2.5 h	45 min	2.0 mmol
D	1.0 h	45 min	2.0 mmol
E	1.5 h	45 min	2.0 mmol
F	2.0 h	60 min	1,5 mmol

#### **2.4.1.4.2 Synthesis Cubic Shaped Iron Oxides by Using Oleic Acid –Sodium Oleate as a Surfactant**

To be able to increase the reflux temperature a new procedure was applied [59], where oleic acid and sodium oleate mixture was used as a surfactant. Firstly iron oleate was synthesized by mixing 3 mmol sodium oleate, 15 mL water, 8.95 g oleic acid, 10 mmol  $\text{FeCl}_3 \cdot 6\text{H}_2\text{O}$ , 20.0 mL ethanol, and 35 mL hexane for 4h at 70 °C. After washing product with water and hexane, the brown paste was obtained as iron oleate. For thermal decomposition procedure, 0.95 g iron oleate, 0.16 g was dissolved in octadecene stirred for 1 h at 200 °C and temperature was increased to the reflux temperature of about 310 °C. Following 1 h stirring at this temperature, washing procedure applied and nanoparticles dispersed in hexane (Table3, A).

**Table 3.** Optimization studies of synthesis cubic shaped iron oxides by using oleic acid-sodium oleate as a surfactant.

Experiment Name	Iron–oleate complex formation in reaction medium	NaCl Addition
A	No	No
B	Yes	No
C	Yes	Yes

Xu et al.'s method was also tried for synthesizing cubically shaped iron oxide nanoparticles. In this method, iron oleate complex was not prepared separately. All of the precursors (0.25 mmol  $\text{FeCl}_3 \cdot 6\text{H}_2\text{O}$ , 1.5 mmol sodium oleate, and 5.0 mL octadecene) were stirred for 1h at  $130^\circ\text{C}$ . Afterwards, the mixture was stirred for 2 h 20 min at a reflux temperature of about  $317^\circ\text{C}$ . After cooling room temperature, magnetite nanoparticles were washed with ethanol, water and hexane mixture via extraction method and dispersed in toluene (Table 3, B)

Finally, Xu et al.'s method was modified. Iron oleate complex was prepared according to the first method [63]. For thermal decomposition procedure, sodium oleate was used as the surfactant. 0.25 mmol iron oleate, 0.75 mmol Na-oleate, 0.75 mmol sodium chloride, and 5.0 mL octadecene were stirred for 1 h at  $130^\circ\text{C}$  and temperature was elevated to reflux temperature of about  $317^\circ\text{C}$  and after stirred 2 h 20 min at that temperature, particles washed again extraction procedure same way at previous trial and dispersed at toluene (Table3, C).

### 2.4.1.5 Conversion of Hydrophobic Cubic Shaped Iron Oxide Nanoparticles into Hydrophilic Form

To make cube shaped iron oxide nanoparticle hydrophilic [89] Rho et al. procedure was used. 0.6 mL hydrophobic cube shaped magnetic nanoparticles were added to 5.0 mL DMF/DCM, (1/1) mixture and 60 mg Polyvinylpyrrolidone (PVP) added at stirring. The final mixture was stirred 10 hours at 100 °C. After 10 hours, 10 mL diethyl ether was added drop by drop to the mixture and the white precipitate was obtained. That precipitate was washed with ethanol and dispersed in water.

## 2.5 Preparation TPP-(CH<sub>2</sub>)<sub>3</sub>-OH and TPP-DCA

### 2.5.1 Synthesis of (3-hydroxypropyl)triphenylphosphonium-(TPP-(CH<sub>2</sub>)<sub>3</sub>-OH)

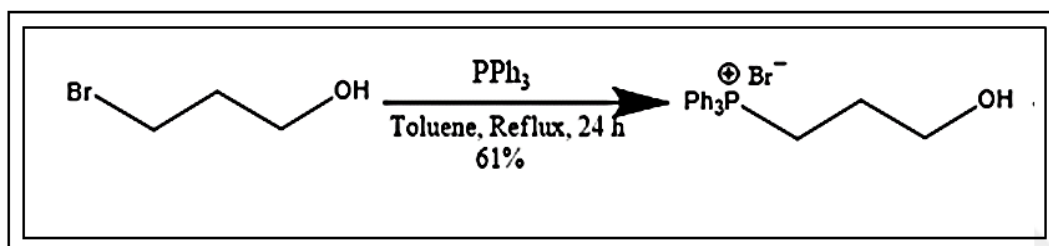


**Figure 12.** Reaction for the synthesis of TPP-(CH<sub>2</sub>)<sub>3</sub>-OH)

A mixture of 0.5 g 3-bromopropanol and 1.05 g triphenylphosphine, 12.5 mL toluene were heated to reflux for 24 h. After the evaporation of the solvent, white precipitate was washed with diethyl ether three times [90]. Reaction conditions are given in reaction scheme in Figure 12.



### 2.5.2 Synthesis of (3-(2,2-dichloroacetoxy)propyl) triphenylphosphonium ( TPP-DCA) by Using Dichloroacetic anhydride

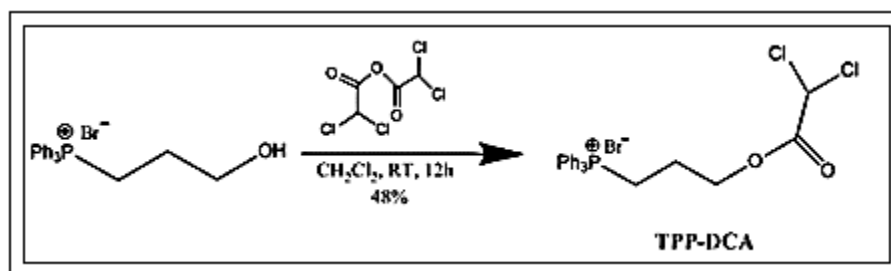


**Figure 13.** Reaction for the synthesis of TPP-DCA by using dichloroacetic anhydride

A solution of 0.125 g TPP-(CH<sub>2</sub>)<sub>3</sub>-OH in CH<sub>2</sub>Cl<sub>2</sub> (15.0 mL) was prepared in a round-bottom flask and stirred for 10 minutes under nitrogen gas flow. 0.262 g (3.72 mmol) dichloroacetic anhydride was added to the solution. The mixture was stirred overnight at RT. The same procedure was repeated by using 1.86 mmol dichloroacetic anhydride. Reaction is given in Figure 13. After reaction was complete, the solvent was evaporated and colorless-light yellow paste was obtained. By using TLC technique, the suitable solvent system was found for purification studies. Different solvents such as CH<sub>2</sub>Cl<sub>2</sub>:CH<sub>3</sub>OH: CH<sub>2</sub>H<sub>5</sub>OH, CH<sub>2</sub>Cl<sub>2</sub>:CH<sub>3</sub>OH, and CH<sub>2</sub>Cl<sub>2</sub>:CH<sub>3</sub> COOCH<sub>2</sub> CH<sub>3</sub> were tested for best resolution. Silica column chromatography and preparative TLC was used for purifications [91].

To prepare silica column, 60 cm length and 2,5 cm diameter glass burette was filled by Silica Gel 60 ((0.063-0.200 Mm) in dichloromethane.

To prepare Preparative TLC plate, 80 mg silica gel (Silica gel 60 HF254 (MERCK)) was dispersed in 100.0 mL DI water. 20x20 cm glass surface was coated with this mixture and dried at room temperature. The silica thickness was about 0.4 mm.

Preparative TLC procedure applied. After filtering procedure, the solvent was evaporated under vacuum and yellow to colourless oily product remained.

### 2.5.3 Synthesis of (3-(2,2-dichloroacetoxy)propyl) triphenylphosphonium (TPP-DCA) by Using Dichloroacetylchloride

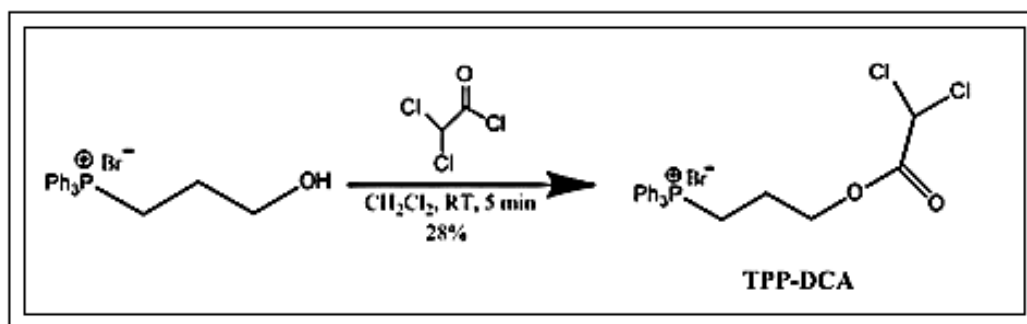


**Figure 14.** Reaction for the synthesis of TPP-DCA by using dichloroacetylchloride

TPP-DCA was synthesized in a different way. Instead of using dichloroacetic anhydride, dichloroacetylchloride was used. 0.125 g TPP-(CH<sub>2</sub>)<sub>3</sub>-OH and 70 μl dichloroacetylchloride were stirred in CH<sub>2</sub>Cl<sub>2</sub> (15.0 mL) in a round-bottom flask. Reaction is given in Figure 14. After 10 minutes stirring under nitrogen gasses, reaction condition was kept during 5 minutes at room temperature until turbidity disappear. For purification studies, TLC, silica column and preparative TLC were used and different solvent systems were tried. For preparation silica column and preparative TLC plate same procedure that were used in section 2.5.1, were applied.

## 2.6 Surface Modification of Iron oxide Nanoparticles

### 2.6.1 Coating by Heparin

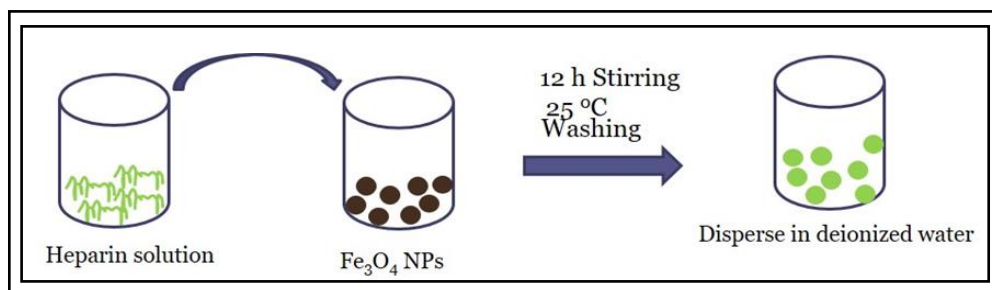


**Figure 15.** Scheme of procedure of heparin coating of spherical iron oxide nanoparticles

Scheme of heparin coating procedure is given above at

Figure 15. The concentration of spherical magnetite nanoparticles was adjusted 2.78 mg/mL. Before the coating procedure, magnetite nanoparticle solution was acidified to pH 3 by using 0.5 M HNO<sub>3</sub> solutions. Heparin solution that 40 mg heparin in 5 mL DI water, prepared and its pH adjusted to 10. That solution was added to 25 mL spherical magnetite NPs solution drop by drop. After two times washing with DI water by using a magnet, heparin coated magnetite nanoparticles dispersed in 25 mL DI water.

### 2.6.2 Attaching TPP-DCA to Heparin Coated Iron Oxide Surface

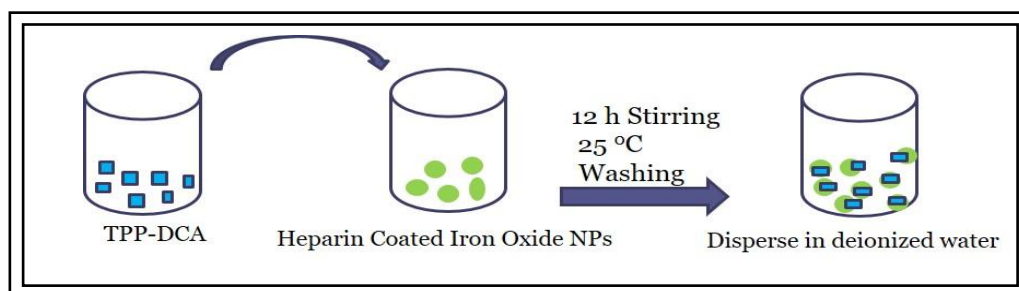


**Figure 16.** Scheme of procedure of TPP-DCA attaching on magnetic nanoparticle surface

Scheme of TPP-DCA attaching on magnetic nanoparticle surface procedure is given above at Figure 14. 9 mg Heparin coated iron oxide nanoparticles were dispersed in 25 mL DI water. TPP-DCA solution is prepared as 1mg/mL and iron oxide nanoparticles added to 8 mL TPP-DCA solution drop by drop. After 2 h stirring, nanoparticles were washed two times by using a magnet (Figure 16).

### 2.6.3 Embedding TPP-DCA into Heparin Layer

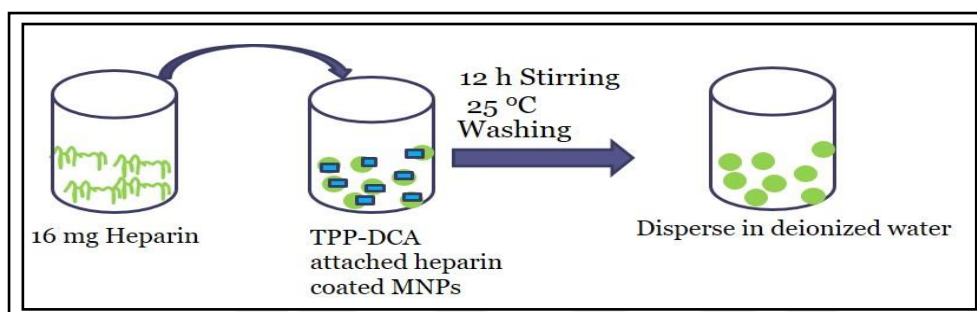


**Figure 17.** Scheme of procedure of heparin coating of magnetic nanoparticles second layer

9 mg TPP-DCA attached heparin coated iron oxide nanoparticles were dispersed in DI water. This solution was added to 10.0 mL heparin solution (1.6mg/mL). After 12 h stirring nanoparticles were washed two times. Scheme of procedure of heparin coating of magnetic nanoparticles second layer is give above at Figure 17.

#### 2.6.4 Attaching 2-deoxy-D-glucose

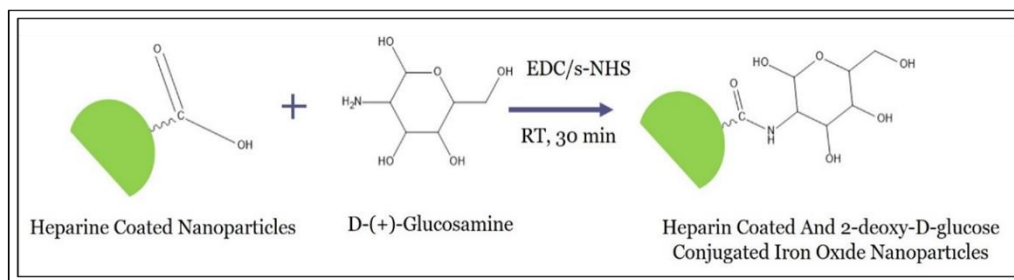


**Figure 18.** Scheme of attaching 2-deoxy-D-glucose by EDC/NHS coupling method onto the surface of double layer heparin coated and TPP-DCA loaded magnetic nanoparticles.

Heparin coated iron oxide nanoparticles were dispersed in DI water. By using EDC/sNHS coupling reaction 2-deoxy-D-glucose molecule was attached to the surface of heparin coated iron oxide nanoparticles. 0.5 m M EDC and 2.5 mM s-NHS were added to heparin coated iron oxide nanoparticles solutions, respectively. After 30 min stirring, 10.0 mL, 0.05mg/mL 2-deoxy-D-glucose solution added to the same solution. After 2 h stirring, by using a magnet, magnetic nanoparticles were washed four times [92]. Scheme of attaching 2-deoxy-D-glucose by EDC/NHS coupling method onto the surface of double layer heparin coated and TPP-DCA loaded magnetic nanoparticles is given in Figure 18.

#### 2.6.5 Determination 2-Deoxy-D-glucose By Cupric Reduction Based on Methods

Scheme of detection procedure of glucose on magnetic nanoparticle surface is given below, Figure 19. Total volume adjusted as 5.0ml and 1 mL of Copper (II) chloride, 1 mL of Neocuproine solution, (x) mL standart or sample, (1 – x) mL in H<sub>2</sub>O, 1 mL sodium hydroxide solution, and 1 mL of sodium potassium tartrate solution were added test tubes. Test tubes were incubated at 60 °C about 20 min. By adding NaOH solution at different concentrations, the optimum pH was adjusted. A standard glucose

solution was used for drawing calibration curve. Absorbance at 455 nm against blank were used to determine the unknown amount of 2-deoxy-D-glucose on the surfaces of magnetite and nanoparticles [93].

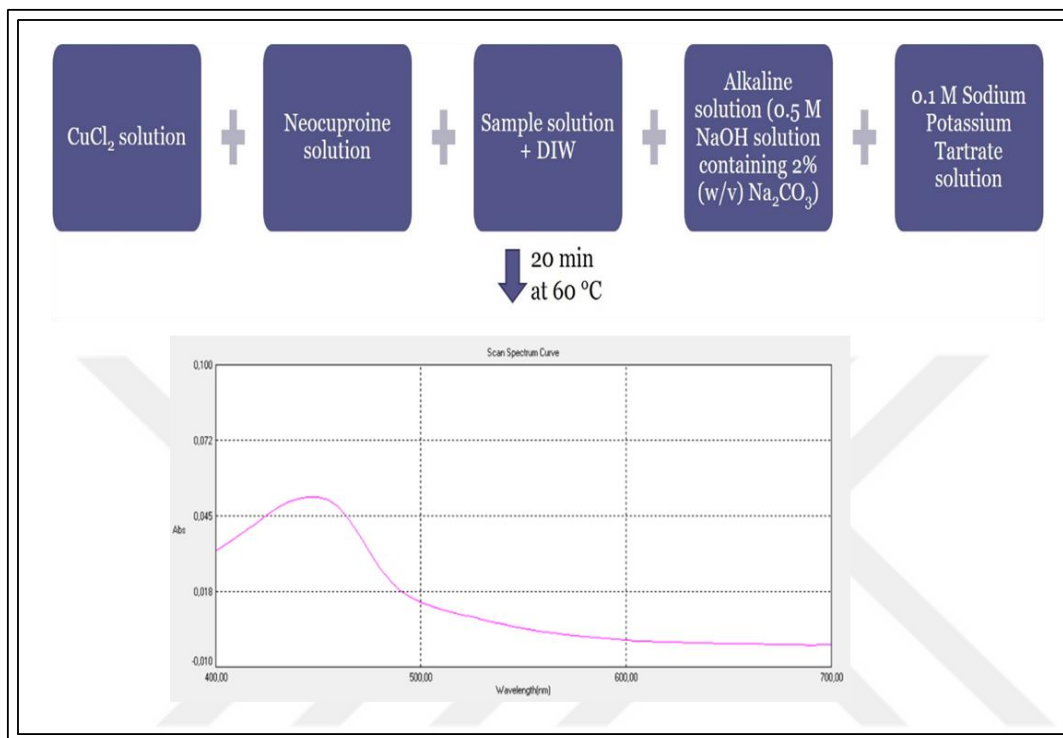


**Figure 19.** Scheme of detection procedure of glucose on magnetic nanoparticle surface

## 2.7 Biological Experiments

Biological experiments were carried out at Department of Biological Sciences (METU) under the supervision of Prof.Dr. N.Tülün Güray.

### 2.7.1 Cell Culture Conditions

Adherent and epithelial-like hepatocellular carcinoma cell lines (HepG2) were used in the investigation of cytotoxic effects of 2-DG-HEP-TPPDCA-HEP coated IONPs. Dulbecco's Modified Eagle Medium (DMEM) Low Glucose with L-Glutamine,

Sodium Pyruvate and 25mM HEPES (Biowest, Cat.No: L0065) medium was used as growth medium with the addition of 10% Fetal Bovine Serum (FBS) and 1% Penicillin-Streptomycin. The cells were incubated at 37°C under a humidified atmosphere with 5% CO<sub>2</sub> and the medium changed 1-2 days intervals.

### **2.7.2 Cell Passaging/ Trypsinization**

The cells were grown in the growth medium in the T-75 flasks until their confluency reached to around 80%. After removing growth medium, cells were washed with PBS solution. Then, in order to detach cells from the surface of flasks, 2 mL Trypsin/EDTA solution was added and then T-75 flasks were incubated in 5% CO<sub>2</sub> humidified atmosphere at 37°C in incubator. Nearly 5 minutes were sufficient for deattachment of HEPG2 cells. Then, 6 ml of growth medium was added to each flasks to neutralize the activity of trypsin. The final cell suspension (8 ml) were divided in new two T-75 flasks as equal volumes (4 ml) and 6 ml of fresh growth medium was added to each flasks and cells were incubated at 37 °C under a humidified atmosphere with 5% CO<sub>2</sub> in incubator.

### **2.7.3 Cell Culturing**

For the preparation of stock solution of 2-deoxy-D-glucose modified TPP-DCA embedded heparin coated iron oxide nanoparticles (2-DG-HEP-TPPDCA-HEP coated IONPs), nanoparticles which had been dispersed in DI water, were collected with the help of magnet and washed two times with growth medium. After washing procedure, they were diluted with the growth medium containing % 0.1 DMSO and the nanoparticles of 4mg/ml concentration were sonicated in the ultrasonic bath for about 5 minutes. 2-DG-HEP-TPPDCA-HEP coated IONP solution were prepared as 50µg/ml, 125µg/ml, 250µg/ml, 375µg/ml, 500µg/ml, 750µg/ml dilutions and the cells were treated with these diluted nanoparticle solutions. Then the cells were incubated for 24-hour at 37°C under 5% CO<sub>2</sub> in the incubator.

#### **2.7.4 Trypan Blue Exclusion (Cell Counting)**

About 500,000 cells/well were seeded in 6-well plates and incubated at 37 °C under the humidified atmosphere in CO<sub>2</sub> incubator. After a 24-hour incubation, medium in the wells was removed and cells were washed with PBS. In order to detach the cells, 0.5 ml trypsin was added to each well and then waited for 5 minutes in the incubator. Later, to deactivate trypsin, 1 ml of fresh growth medium was added into the wells. The detached HepG2 were transferred into Eppendorf tubes. The cells were diluted with 0.25 M Trypan Blue with a 1:1 ratio and then cells were counted with a hemacytometer under the light microscope to understand cell viability. Trypan Blue penetrates into the dead cells so dead cells were observed in blue color, while living cells were still transparent.

#### **2.7.5 XTT Cell Proliferation Assay**

XTT- tetrazolium dye (2, 3 -Bis- (2-Methoxy- 4-Nitro- 5-Sulfophenyl)-2HTetrazolium- 5-Carboxanilide) cell proliferation kit can be used for cell proliferation, apoptosis assays, and cytotoxicity. This kit is used for the detection of mitochondrial dehydrogenase activity and it forms an orange coloured formazan XTT product which is water-soluble. The sensitivity of the XTT assay is suitable for the determination of IC<sub>50</sub> value.

10,000 cells were seeded per well in a 96-well plate and incubated for overnight to allow cells to attach. Afterwards, medium in the wells were discarded and the wells were washed with 50 µl of PBS and then wells containing cells and empty wells for controls were treated with the dilutions of the nanoparticle solution (50µg/ml-750µg/ml) for 24 hours. After the 24 hour incubation, first, magnet was kept at the top of the 96-well plate for 30 seconds to collect remaining nanoparticles (magnetic washing), and then, the medium containing nanoparticles were discarded and wells were washed with 50 µl of PBS twice in order to get rid of black-coloured nanoparticles which might interfere with the absorbance readings of XTT reagent. Then 100µl of growth medium was added to the each well immediately to avoid drying out the cells and 50µl of XTT solution that was freshly prepared by mixing 5 ml of



XTT reagent and 100 $\mu$ l of activation reagent provided by the kit (Cell Proliferation Kit-XTT based, Biological Industries) was added to the wells and waited for incubation. After 4 hour incubation, the absorbance values were measured at 450nm and 630nm by using microplate reader. The absorbance readings at 630nm were subtracted from 450nm readings to clear non-specific readings in the wells and also by subtracting absorbance values of control wells from that of wells containing cells, the cell viability percentages were calculated.

## **2.8 Designing Inductive Heating Device**

Magnetic Hyperthermia device is started to be developed in our laboratory by Seckin ÖZTÜRK in response to the lack of adequate induction heaters available on the market to work with superparamagnetic nanoparticles. Figure 20 shows the view of the 13 turn copper wire (2 and 4 cm diameter) coils used by the magnetic hyperthermia device to induce heating through magnetic nanoparticles. The image also shows reflux condenser system (0.5 mm insulation thickness) that isolate the sample container from the heat radiated by the coil, the sample container and the thermometer. This was the first design used in our hyperthermia measurements.

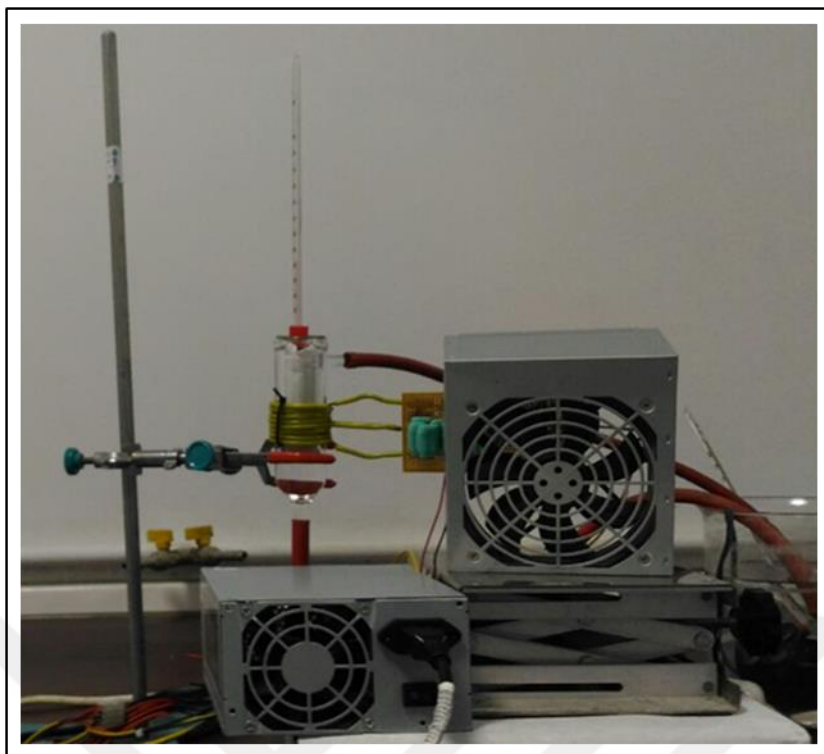


**Figure 20.** Front view of the 13 turn coils used in the hyperthermia system to induce heating from nanoparticles in the sample.

We were able to change the coil appendages and tried several different turn coils that allow the system to bring the inductive heating.

Figure 20 shows such a coil. The sample is located in a tube 1 mL inside the cooling system which is placed in the coil. Following the application of the frequency a thermometer measures the temperature increase of the solution in due course. At the beginning of the work the hyperthermia device was powered by 12 Volts at ca. 2.5 Amps. It provided a frequency of  $\sim 100$  kHz. We could not measure the magnetic field created. After power supply was changes the hyperthermia device was powered by 20 Volts at ca. 4.5 Amps.

The constructed system is still in development. During the optimization studies power intensity, capacitor, power supplier, coil type and coil diameter have been changed. In all measurements spherical shaped iron oxide nanoparticles were used at different

concentrations (20mg/mL, 40mg/mL and 160mg/mL) these will be mentioned in the Result and Discussion section.





## CHAPTER 3

### RESULTS AND DISCUSSION

In the aim of this thesis, iron oxide nanoparticles were synthesized with different shape and size. For biological experiments spherical magnetite nanoparticles were prepared. To characterize size and shape of nanoparticles Transmission Electron Microscopy and Scanning Electron microscopy were used. Their crystal structure were analyzed by using X-ray Diffraction Spectroscopy. Their surface coated with heparin and TPP-DCA that prepared and purified. For being embedded of TPP DCA into heparin layer, second layer heparin was coated. For targeting aim, 2-deoxy-D-glucose molecules were attached to nanoparticles layer. To prove heparin and TPP DCA coating, Zeta Potential Measurements and UV-VIS Spectroscopy were used. Additionally, thermal gravimetric analysis hold on.

For biological experiment HepG2 cell lines were used. To determine IC50 value XTT analysis was hold on. For hyperthermia measurements, device which induce the inductive heating of magnetic nanoparticles. First trials were done and results were recorded.

#### **3.1 Preparation of Magnetic Nanoparticles**

##### **3.1.1 Preparation Spherical Shape Fe<sub>3</sub>O<sub>4</sub> NPs**

Spherical shaped magnetite nanoparticles were synthesized by co-precipitation methods [57]. Transmission Electron Microscopy (TEM) was used for characterization and X-Ray Diffraction (XRD) measurements were used for characterization

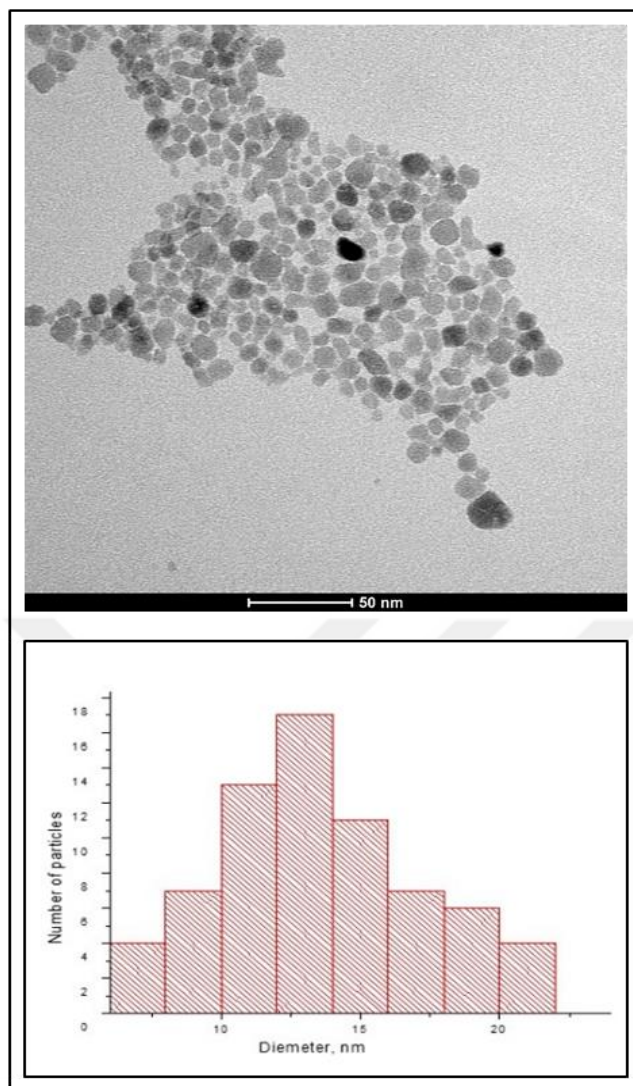


**Figure 21.** TEM image and size distribute on of iron oxide nanoparticles that were prepared by co-precipitation method

For TEM imaging procedure formvar and carbon coated 200 mesh grid was used. To decrease agglomeration of iron oxide nanoparticles, solution was acidified by using 0.5 M HNO<sub>3</sub> and pH of solution adjusted to 3.0. When preparing the TEM grid, if the sample is dropped on the grid, magnetic particles were collapsed during drying stage due to the magnetic attraction among particles. For this reason, dipping technique is preferred instead of dropping. In this way, the TEM grit is kept in contact with the iron oxide solution for a very short time by holding it with a tweezers and then the excess solution is removed by means of an absorbent paper. TEM image and size distribution

histogram of the magnetite nanoparticles are given in Figure 21a and 21b respectively. As can be seen from Figure 21a, shapes of the nanoparticles are mainly spherical. According to the histogram, Figure 21b, the size distribution range of the nanoparticles is 6-21 nm. However almost 50% of the particles are in the size range of 10-16 nm. The mean diameter of the particles is  $13.6 \pm 3.6$  nm.

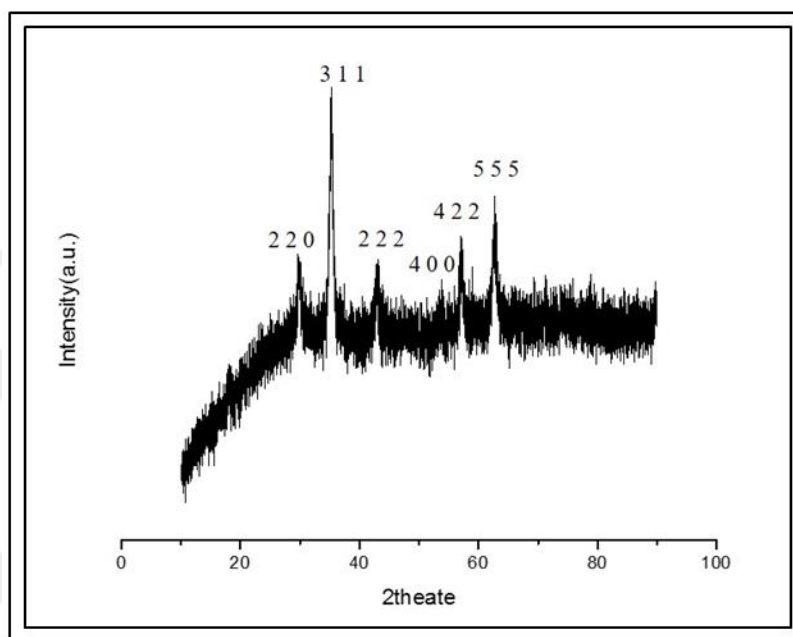


**Figure 22.** XRD pattern of iron oxide nanoparticle which were prepared by co-precipitation method

To confirm crystal structure of magnetite nanoparticles XRD analysis was carried out in the angular range of  $10^\circ \leq 2\theta \leq 90^\circ$ . The peaks at  $2\theta$  values:  $30.07^\circ$ ,  $34.54^\circ$ ,  $42.00^\circ$ ,  $53.95^\circ$ ,  $56.65^\circ$ ,  $64.69^\circ$  are corresponding to (2 2 0), (3 1 1), (2 2 2), (4 0 0), (4 2 2), (5 5 5) Bragg's reflections, respectively (Figure 22). According to comparison of the experimental XRD pattern with the standard database (JCPDS card no:19-0629), face centered cubic (fcc) structures of magnetite nanocrystals were synthesized [94].

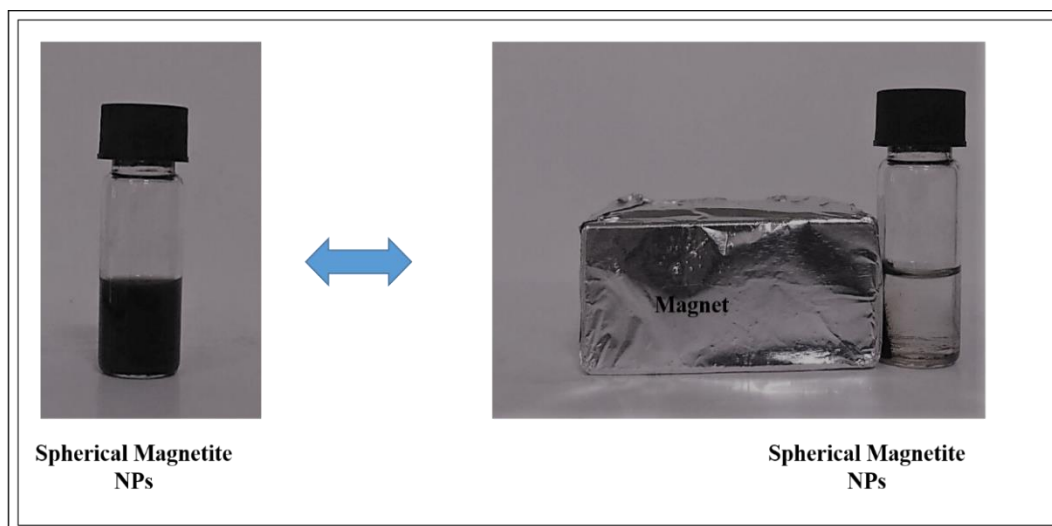


**Figure 23.** Behavior of spherical shaped magnetite nanoparticles under the magnetic field.

Figure 23 shows the magnetic behaviour of the spherical shaped iron oxide nanoparticle solution. Nanoparticles were collected magnet after 15 seconds. This observation indicates that although they were small in size, they formed agglomeration.

### 3.1.2 Preparation of Flower Shape $\text{Fe}_2\text{O}_3$ NPs

The polyol pathway is an effective synthesis method for oxide nanoparticles. Temperature, the nature of the precursors and the solvent, reaction time are important parameters to obtain nanoparticles with adjustable size and shape. In this study, polyol method was used for the synthesis of flower shape  $\text{Fe}_2\text{O}_3$  NPs. At first trial, as a solvent and stabilizer only TEG was used without a co-solvent (DEA). Reflux was carried out at 220 °C, for 2 hours. Heating rate was 1 °C/min. The collapse of particles at the end of the reaction due to the aggregate formation was observed. Metal oxides formation occurs from chelated TEG complexes and this process is irreversible. Hydrolysis reactions in TEG is followed by a rapid nanocrystal nucleation and growth.



Coalescence of small nanocrystals and Internal recrystallization of the nanoparticles take place during aging period [68]. TEM was used for the characterization of the particles, Figure 24.

According to the TEM images, homogeneous, spherical particles were synthesized at a size range of 10 nm instead of the expected flower-like particles.

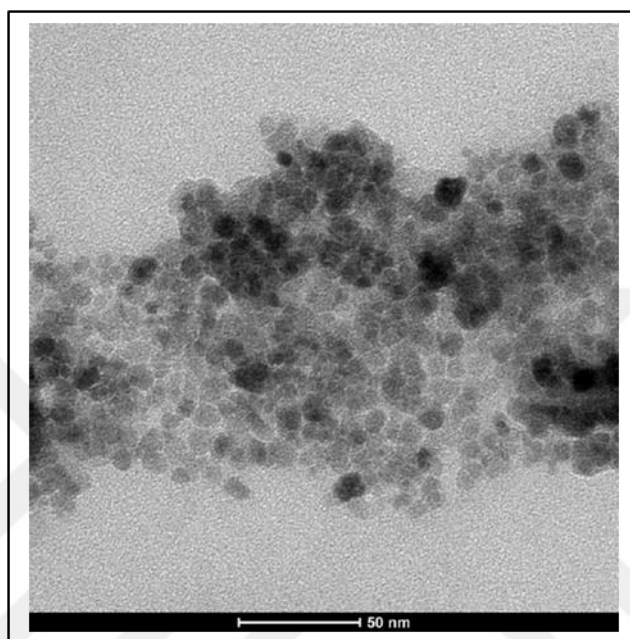


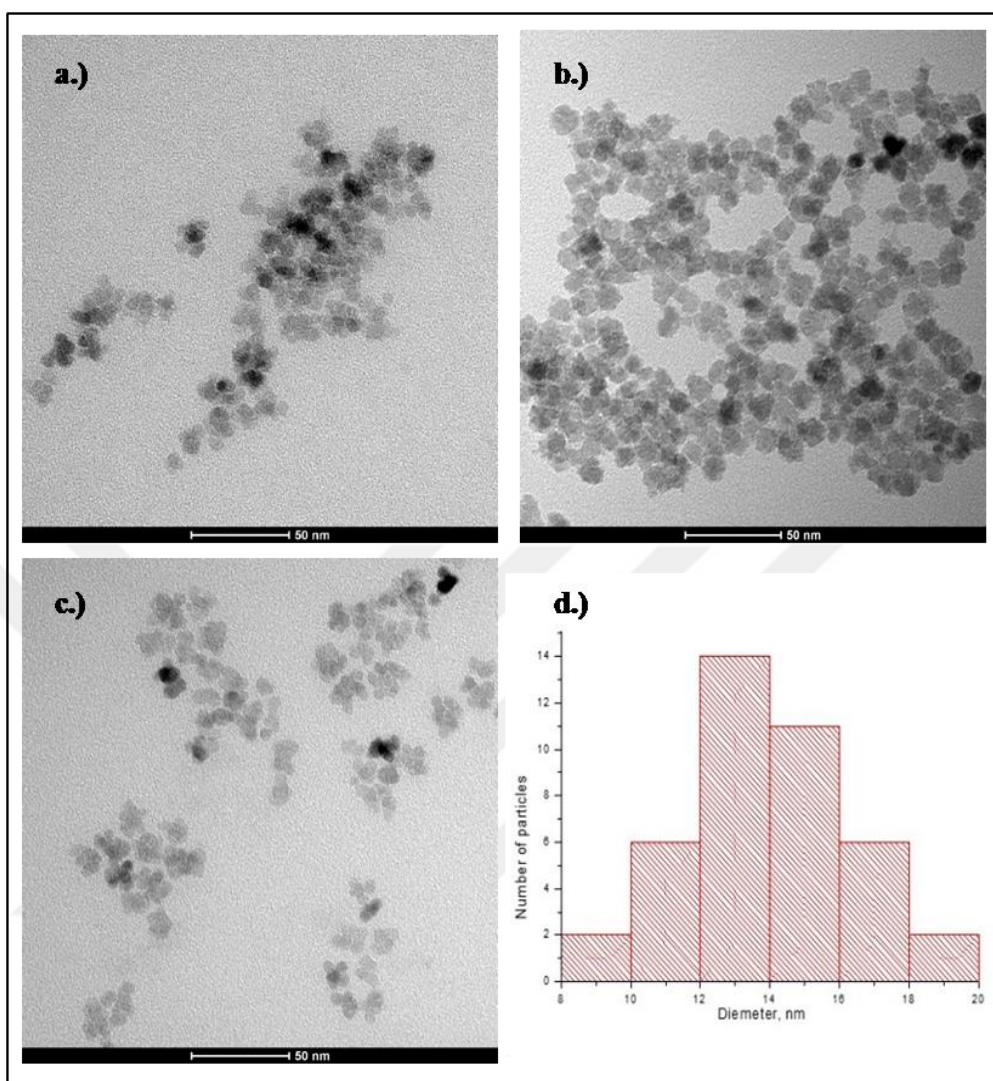
**Figure 24.** TEM image of flower-like shaped iron oxide nanoparticles that were prepared absence of DEA with 1 °C/min heating slope, 2h reflux time at 220 °C;

In order to obtain flower shape, a co-solvent was decided to be used in the reaction to slow down the reaction rate. Therefore TEG:DEA mixture with a ratio of 1:1 was started to be used as polyol and reflux time was changed as 0.5, 1.0 and 2.0 hours. Reflux temperature and heating rate were not changed. TEM images belong to flower shape Fe<sub>2</sub>O<sub>3</sub> NPs prepared under the conditions specified in Table1 (2b,3c and 4e). Usage of cosolvent provides that lower hydrolysis reaction of metal between the solid oxide and metal complexes in solution. When only TEG was used, internal recrystallization was favourable without any mass transfer. Therefore DEG metal oxide complex becomes irreversible. On the other hand, when DEA was used as cosolvent, hydrolysis reaction occurs slower and small nanoparticles are formed

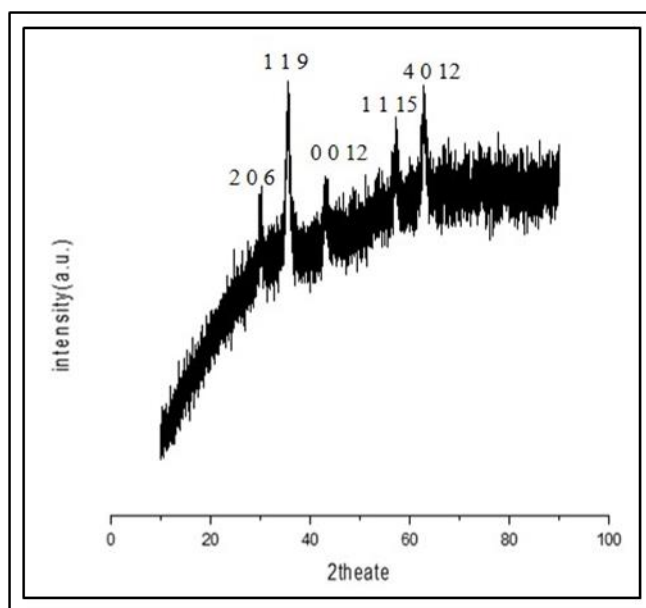
and these small nanoparticles agglomerate to form larger nanoparticles with the secondary recrystallization [68].

According to TEM images shown in Figure 25 as the reflux time shortens the level of aggregation decreases and more disperse flower shape structures were obtained. Therefore 0.5 h reflux time was decided to be the optimum condition to synthesize flower like iron oxide nanoparticles with proper size, Figure 25(c). Size distribution histogram of these particles is given in Figure 25, d. Histogram shows that particle size varies in the range of 9-19 nm and their average size is  $13.5 \pm 3.6$  nm. XRD was used for their crystallographic analysis, Figure 26.



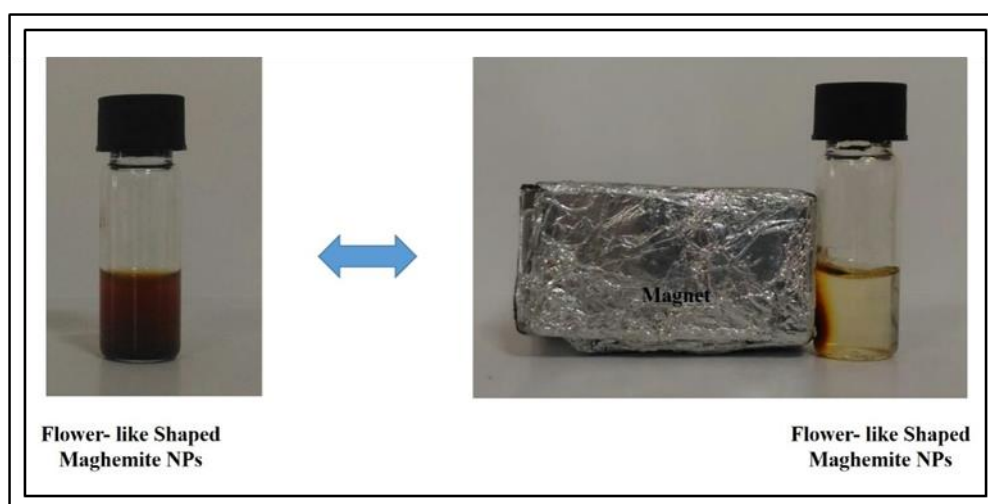


**Figure 25.** TEM images of the nanoparticles prepared by polyol method: Solvent is TEG:DEA (1:1, v/v) heating rate is 1 °C/min, reflux temperature is 220 °C. Reflux time is (a) 2h (Table 1. 2b), (b) 1h (Table 1. 3c), (c) 0.5 h (Table 1. 4e) and (d) size distribution histogram for the particles presented in part c of this Figure, i.e. 0.5 h reflux time.



**Figure 26.** XRD pattern of flower-like shaped iron oxide nanoparticles

The analysis was carried out between angular range at  $10^\circ \leq 2\theta \leq 90^\circ$ . The  $2\theta$  values at  $30.48^\circ$ ,  $35.70^\circ$ ,  $42.79^\circ$ ,  $57.34^\circ$ ,  $62.94^\circ$  depict the (2 0 6), (1 1 9), (0 0 12), (1 1 1 5), (4 0 12) Bragg's reflections, respectively (Figure 25).  $2\theta$  values of the particles are matching with the characteristic  $2\theta$  values of a tetragonal phase of  $\text{Fe}_2\text{O}_3$ , (JCPDS Card no: 25-1402). Results are also consistent with the literature [95].



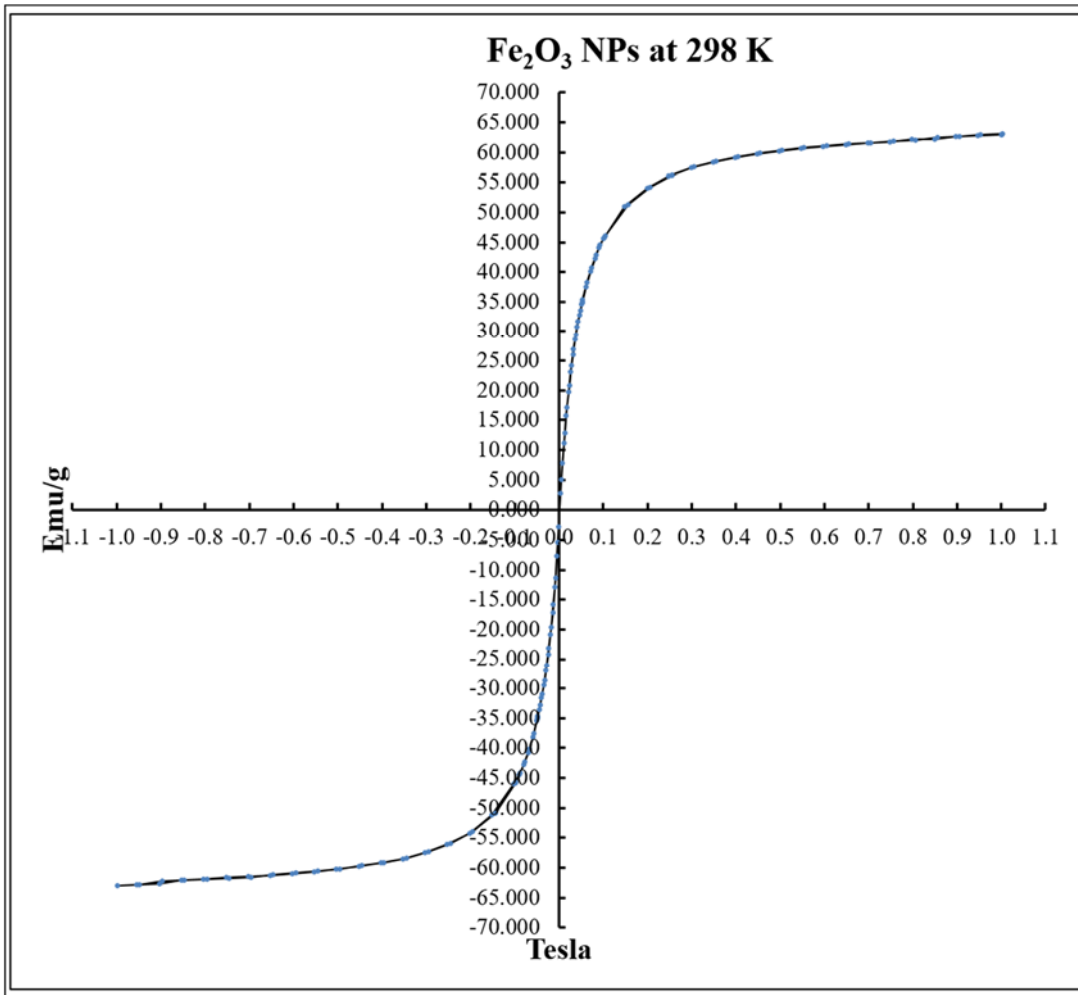
**Figure 27.** Behavior of flower-like shaped iron oxide nanoparticles under the magnetic field.

Figure 27 shows the magnetic behaviour of the nanoflower shaped iron oxide nanoparticles at 300 K. Nanoparticles were collected magnet after 1 minute.

Magnetization measurements are carried out with a field scan of  $\pm 1.1$ T at 298 K and 5 K and hysteresis loops of the nanoflower shaped iron oxide powder (Table 1,4e) are obtained. As it is known nanoparticles are less magnetic than their bulk form because of their high fraction of surface metal ions that are contributing ineffectively to the net magnetization [96]. At Figure 28 magnetisation versus magnetic field curves for flower shaped iron oxide nanoparticles at 298K shown. Nevertheless, nanoflower particles exhibit saturation magnetization of 64,00 emu/g which is quite close the saturation magnetization ( $M_s$ ) value of bulk maghemite, 80 emu/g [97].

$M_s$  values of our flower shaped iron oxide nanoparticles were also compared to that of the literature values [86]. As stated previously, size is an important factor for the magnetization. Nanoflowers, synthesized in this study were having a mean diameter of 13.5 nm and they were established of 6 nm sized grains of maghemite whereas the smallest nanoflowers synthesized by Hugounenqat.al. are having 22 nm average size and the size of the grains constituting the flower shape is 11 nm.

The  $M_s$  value obtained in our study was 64 emu/g which is almost equal to the  $M_s$  value of the nanoflowers (66emu/g) reported by Hugounenqat.al [86] .



**Figure 28.** Magnetization versus magnetic field curves for flower shaped iron oxide nanoparticles (Table 1 Exp 4e) at 298 K .

It is known that, above the blocking temperature ( $T_b$ ) of the nanoparticles, superparamagnetic nanoparticles have zero coercivity due to the competition between the magnetocrystalline anisotropy energy and the thermal energy [86].

As can be seen from the Figure 28, the magnetization reduces from saturation value, 64 emu/g to zero on the absence of the magnetic field, without having any coercivity.

This behaviour proved that our particles are superparamagnetic.

Figure 29 shows magnetization ( $M_s$ ) as a function of applied magnetic field ( $H$ ) for nanoflower shaped iron oxide nanoparticles (Table 1e) at 5K, below  $T_b$  of maghemite ( $\sim 80$  K) [98]. In general, at the temperature values below the blocking temperature, the vector of magnetization cannot be fluctuated even in the absence of an external magnetic field and hence the coercivity value of the superparamagnetic nanoparticles is greater than zero.

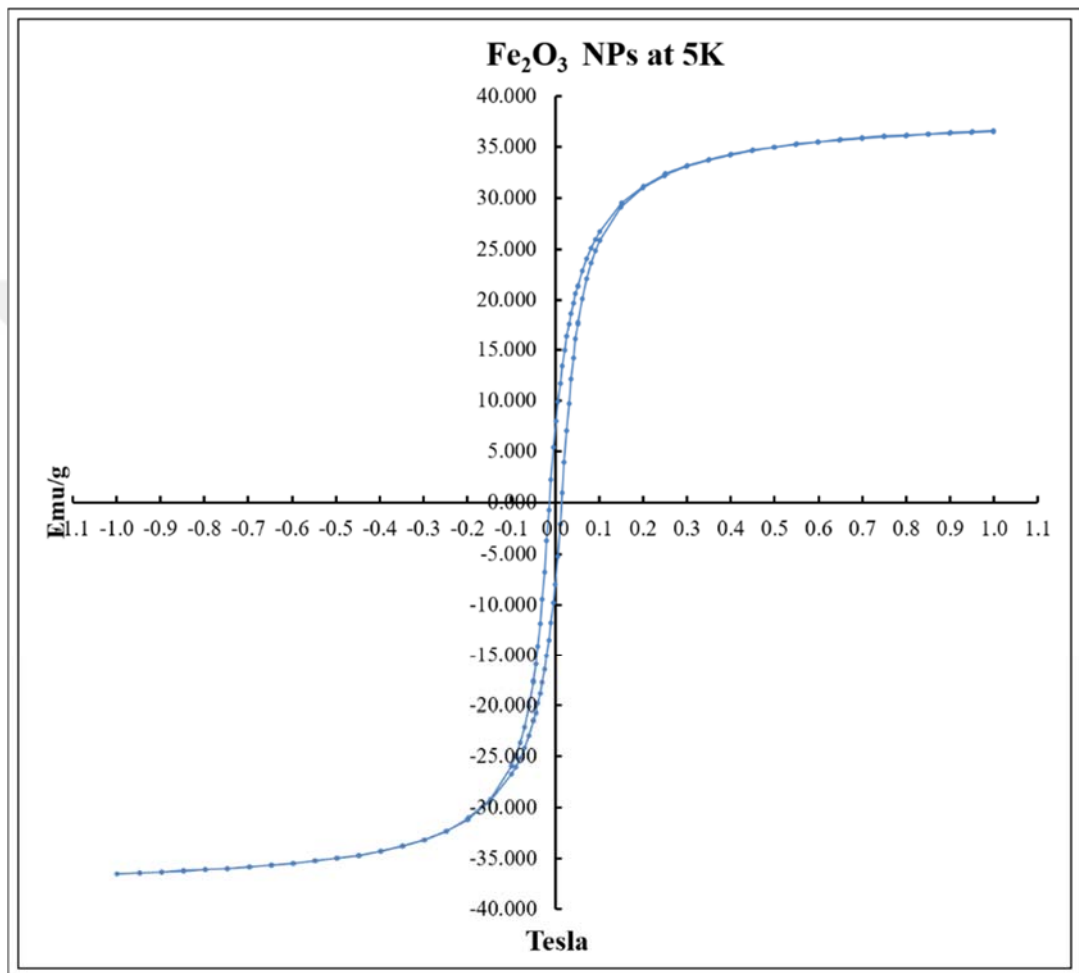


**Figure 29.** Magnetization versus magnetic field curves for flower shaped iron oxide nanoparticles (Table1, 4e) at 5 K.

As expected our nanoflowers do have hysteresis at 5K. As can be seen from Figure 28  $M_s$  of nanoflowers is 36.50 emu/g and their remanent magnetization ( $M_r$ ) is 5.00/g. These magnetic measurements indicate that superparamagnetic nanoflower particles

prepared in this study have high Ms value and are a good candidate for biomedical and particularly for hyperthermia application

### 3.1.3 Synthesizing Iron Oxide Nanoparticles by Hydrothermal Method

The hydrothermal method [87] was applied for the synthesis of cubic shaped iron oxide nanoparticles. Sodium dodecylsulfate and sodium borohydride and  $\text{FeCl}_2 \cdot 4\text{H}_2\text{O}$  were used as a surfactant, reducing agent and iron precursor respectively. For characterization studies SEM and XRD were used. SEM image is presented in Figure 30. Their shape is mostly cubic having about 80 nm size though some spherical shape particles also exist.

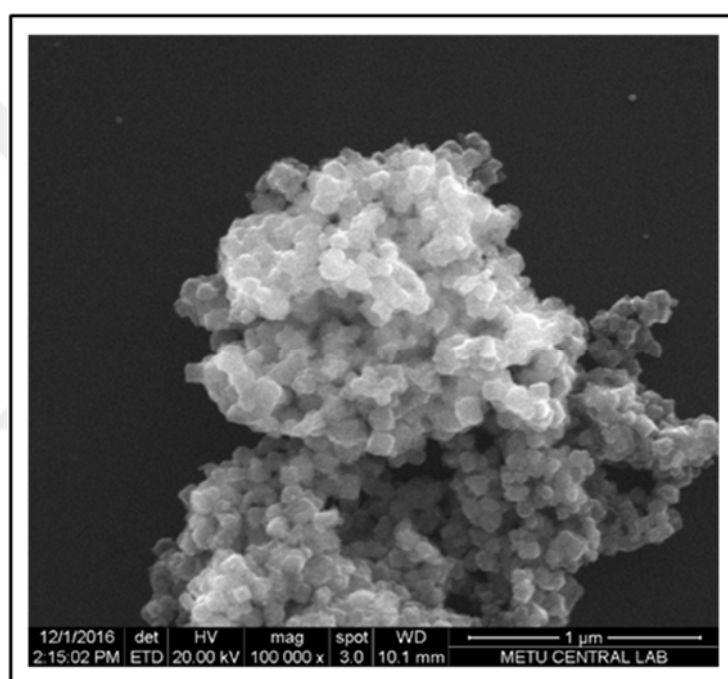


**Figure 30.** SEM image of iron oxide nanoparticles which were prepared by hydrothermal method



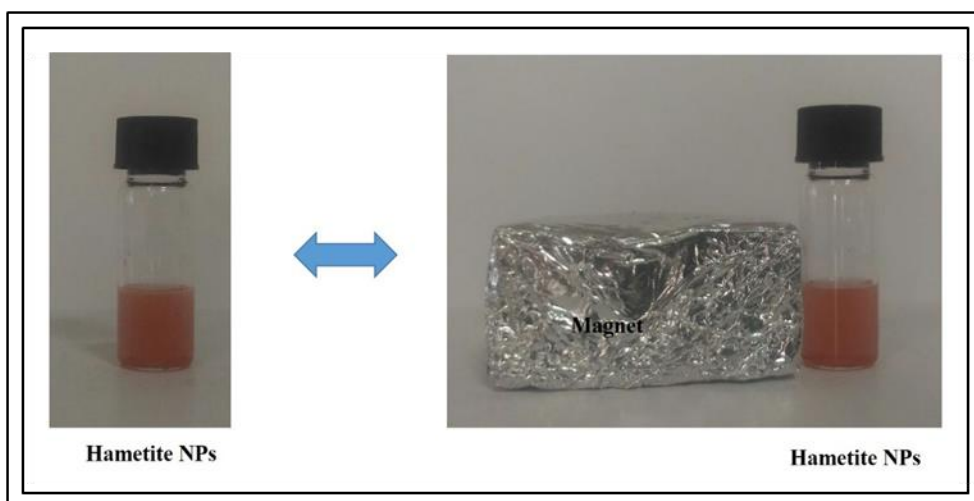


**Figure 31.** Behavior of iron oxide nanoparticles which were prepared by hydrothermal method, under the magnetic field

Despite the fact that it seems to be a very convenient method for obtaining cubic nano structures in a short period of time, the particles obtained do not exhibit magnetic property. As seen in Figure 31, they were not separated from the solution under magnetic field in about an hour.

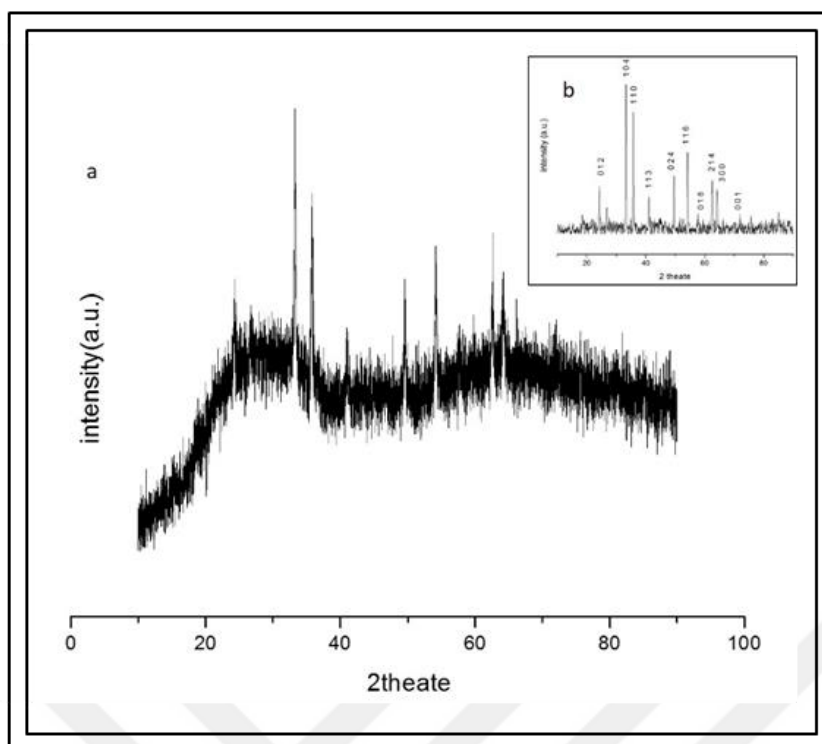


**Figure 32.** (a) Normal and b) baseline corrected XRD pattern of iron oxide nanoparticles which were prepared by hydrothermal method.

To confirm crystal structure of magnetite nanoparticles XRD analysis was carried out in the angular range of  $10^\circ \leq 2\theta \leq 90^\circ$ . The peaks at  $2\theta$  values:  $24.23^\circ$ ,  $33.52^\circ$ ,  $36.12^\circ$ ,  $40.94^\circ$ ,  $49.85^\circ$ ,  $54.64^\circ$ ,  $57.65^\circ$ ,  $62.11^\circ$ ,  $64.71^\circ$ ,  $71.76^\circ$ , are corresponding to (0 1 2), (1 0 4), (1 1 0), (113), (0 2 4), (1 1 6), (0 1 8), (2 1 4), (3 0 0) and (0 1 1) Bragg's reflections respectively (Figure 32).  $2\theta$  values of the particles are matching with the characteristic  $2\theta$  values of hematite structure of iron oxide JCPDS card no: 89-2810). Results are also consistent with the literature According to Han et al. study, XRD pattern indicates that hematite form of iron oxide nanoparticles were synthesized by using the hydrothermal method [99].

Experimental conditions could not be explored because the iron precursor caused corrosion inside the metal parts of the reactor although the reaction was carried out in a Teflon jacket. Therefore the results discussed are the output of a single measurement.

### **3.1.4 Synthesis of Hydrophobic Cubic Shaped Iron Oxide Nanoparticles by Thermal Decomposition Methods**

Thermal decomposition method was used for the Synthesis of cube shape Fe<sub>3</sub>O<sub>4</sub> NPs. Fe-oleate complex formation and higher reflux temperature (about >300 °C ) have an important role for preparing cubic shaped iron oxide nanoparticles. Various procedures were applied and the reaction conditions such as types of surfactants, reflux and intermediate heating temperatures and their durations were modified.

#### **3.1.4.1 Synthesis of Cubic Shaped Iron Oxide Nanoparticles by Using Oleic Acid and Undecanoic Acid as A Surfactant**

Oleic acid was used as surfactant and stabilizer. Thermal decomposition method has already been used in our laboratory for the preparation of spherical Fe<sub>3</sub>O<sub>4</sub> NPs. The main difference in between two procedures was the separation of the heating period into three parts, complex formation time, initial heating and reflux time. Degassed precursors were stirred for 1 h at 60 °C under N<sub>2</sub> atmosphere, the temperature was risen to 200 °C and stirring was continued for 2.5 h. The Fe-oleate complex was expected to be formed at the 60 °C heating step. One hour high-temperature reflux was applied for the decomposition of the formed complex for the synthesis of cubic iron oxide nanoparticles. The highest temperature that could be achieved under this condition was 290 °C.

For the morphological characterization of the particles TEM was used. According to TEM image, and the size histogram prepared by measuring the size of nanoparticles are given in Figure 33. The size of the nanoparticles was accumulated in the range of 5-8 nm and there are highly monodisperse. However, their shapes are mostly triangle prism. Only a few cubic structures were observed.

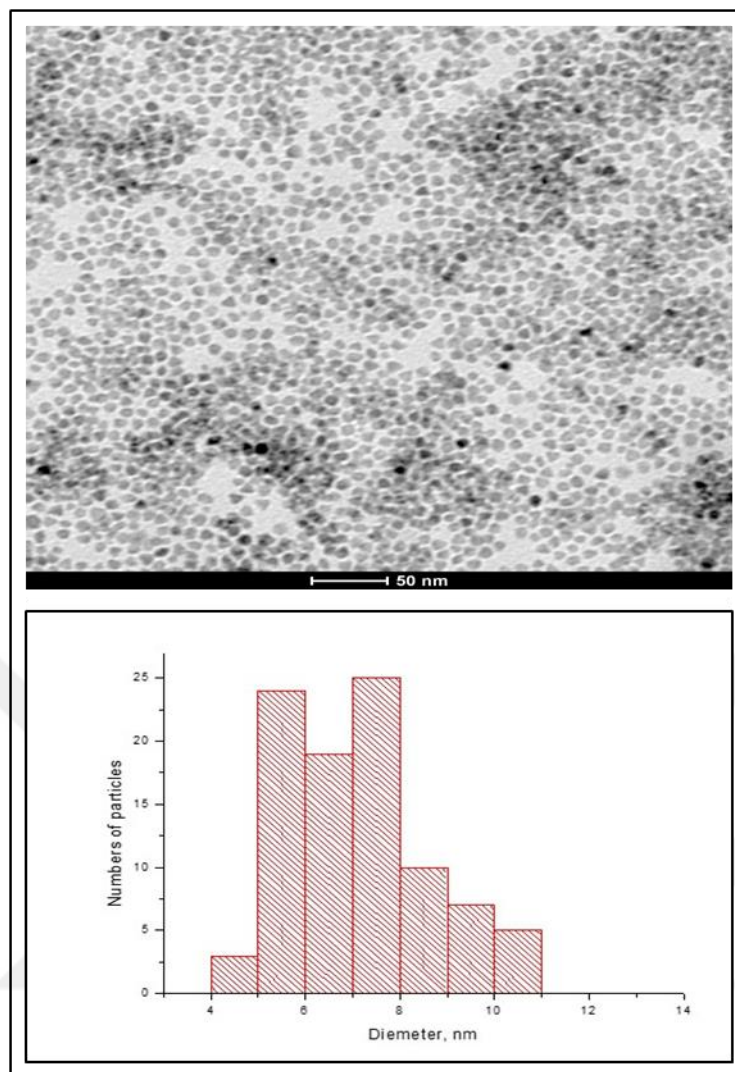


**Figure 33.** TEM image and the size histogram of the nanoparticles prepared by thermal decomposition method by using oleic acid as surfactant

At this stage, surfactant was changed. Instead of oleic acid undecanoic acid was used. Oleic acid has eighteen carbon with a double bond between ninth and tenth carbon which gives an angular shape to the molecule whereas undecanoic acid has ten methyl chain. First of all the effect of complex formation time on the shape control was examined. One hour and 45 minutes complex formation period at 60 °C were tried. For both experiments, 2.5 h initial heating at 200 °C and 1-hour reflux time at highest maximum temperature were applied. TEM images are given in Figure 34.

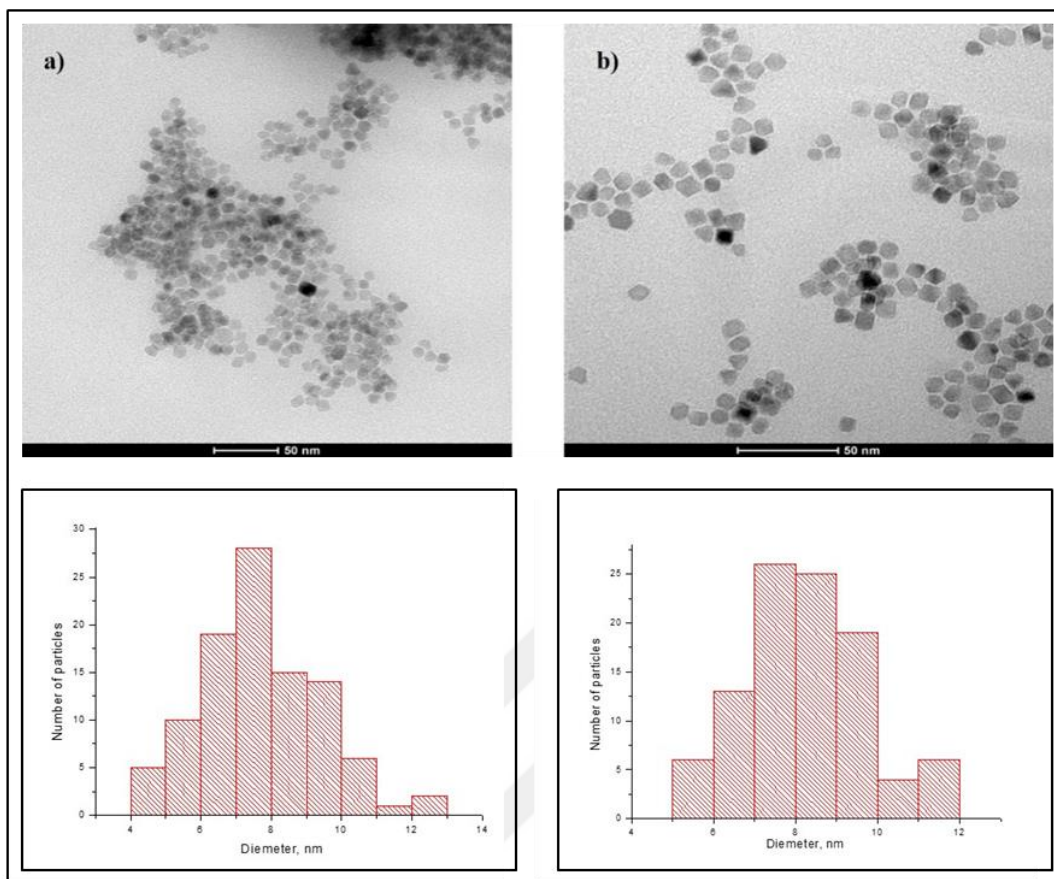


**Figure 34.** TEM images of iron oxide nanoparticles that are synthesized in undecanoic acid by applying a) 1 h and b) 45 min complex formation heating period. Corresponding size distribution histograms of the nanoparticles are given below each TEM images.

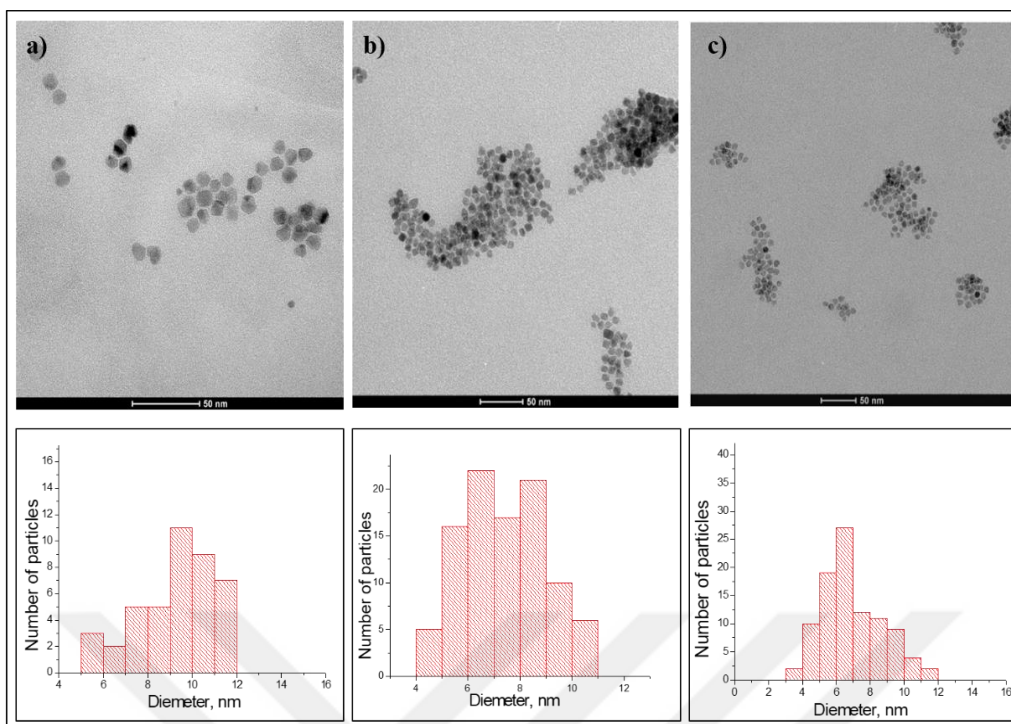


**Figure 35.** TEM images of iron oxide nanoparticles prepared in undecanoic acid with a) 2,5-hours, b) 1-hour and c) 1.5-hours intermediate heating applications at constant complex formation (at 60 °C, 45 min) and reflux time (45 min). Corresponding size distribution histograms of the nanoparticles are given below each TEM images.

As can be seen from Figure 35. When the duration of complex formation is decreased, more cubic shaped particles can be obtained. Therefore 45 min complex formation time was selected and the intermediate heating period was changed in between 1.0-2.5 hrs. TEM images of the particles are given in Figure 34. According to TEM images, no significant change in their size and shape were observed. Additionally, the effect of the amount of the surfactant was examined at 1.0 hr. complex formation period at 60 °C, 1.5-hours intermediate heating at 200 °C and 45 min refluxing time at the highest possible temperature. TEM image and its corresponding size distribution histogram are depicted in Figure 36.

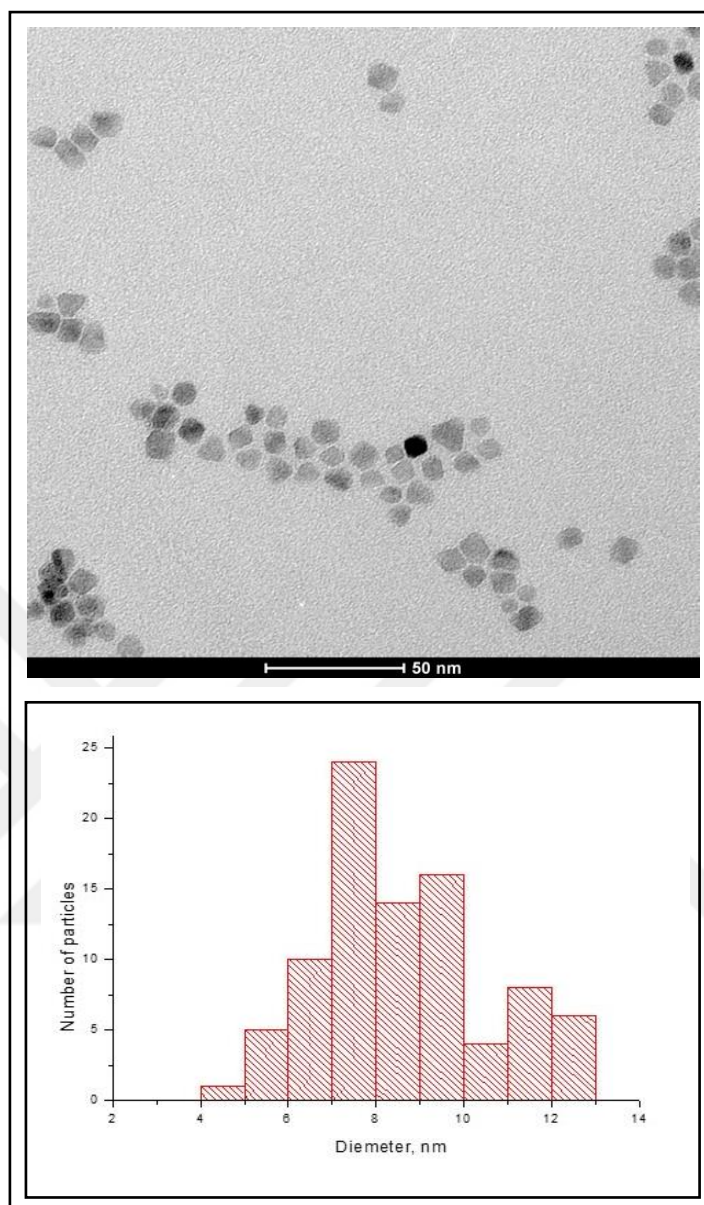


**Figure 36.** TEM images of iron oxide nanoparticles prepared at low concentration of undecanoic acid ( $\frac{1}{4}$  fold of the original amount), 45 min complex formation period at  $60^{\circ}\text{C}$ , 1.5-hours intermediate heating at  $200^{\circ}\text{C}$  and 45 min refluxing time at the highest possible temperature. Corresponding size distribution histogram of the nanoparticles is given below the TEM image.

When the undecanoic acid amount was reduced  $\frac{1}{4}$  fold, Figure 35, again cubic shaped magnetite nanoparticles were obtained, however the shape and size distribution was not homogeneous.

During all these experiments, the main problem was to rise the temperature up to above 300 °C and to keep it there stable throughout refluxing. Occasionally it had reached to 298 °C but rapidly decreased about 20 °C. The boiling point of benzyl ether is 298 °C. It was expected that the boiling point of the benzyl ether solution containing the reaction precursors and surfactants (oleic or undecanoic acid) would be higher than that of the pure compound. It was also reported that benzyl ether decomposes above 310-350 °C. However, the order and rate of this decomposition process are catalysed by acid, glass surfaces, and impurities [100],[60]. Therefore, the decrease in temperature can probably be explained by the decomposition of benzyl ether at temperatures below 300 °C due to the presence of oleic or undecanoic acid and other possible impurities in the reaction medium. It seems that temperature is the most important factor for controlling the shape of the particles. To handle this problem, solvent and surfactant were decided to be changed.

#### **3.1.4.2 Synthesis of Cubic Shaped Iron Oxide Nanoparticles by Using Oleic Acid - Oleate as Surfactant**

By using sodium oleate and oleic acid as a surfactant, three experiments were performed. For all experiment, 1-octadecane was used as solvent so reflux temperature could be increased above 310 °C.



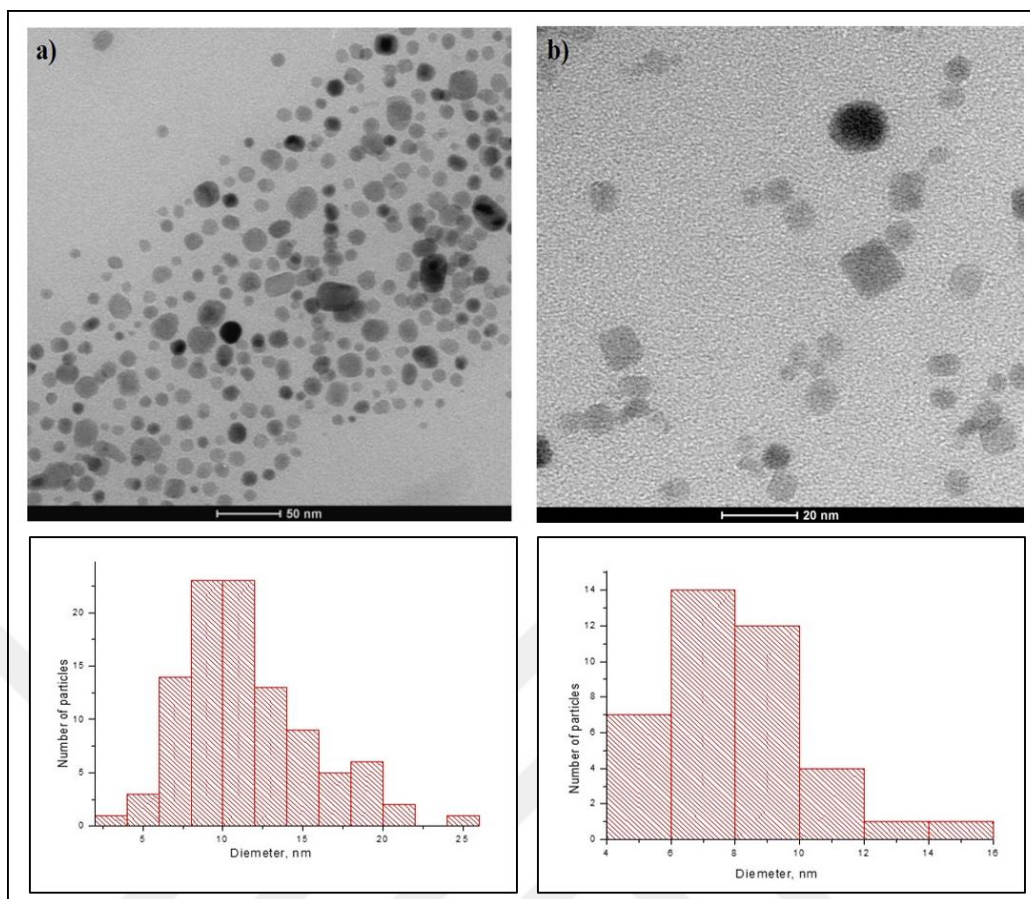


**Figure 37.** TEM images of iron oxide nanoparticles that were synthesized by using a) Fe-oleate-oleic acid, ( Table 3,A), b) Sodium oleate (without preparing Fe-oleate complex), ( Table 3,B) as a surfactant system

For the first trial, the Fe-oleate complex was prepared separately and mixed with oleic acid. According to TEM image, Figure 37a size distribution is not good and their shape mostly spherical (Table 3, A).

For the second experiment, Fe-oleate complex formation step was omitted i.e. precursor and surfactants were mixed at the same time. Considering TEM image of the Figure 37b, although mostly cube shapes were synthesized, spherically shaped particles were also formed. In addition, there is a large variation in their sizes (5 -25 nm), (Table3, B).

For the third experiment (Table 3, C), the same experimental conditions were applied as the previous experiment. The only difference was the usage of the sodium chloride.

Xu et al reported that halogen ions have an important contribution to the formation of cubic shaped metal oxide nanoparticles, particularly the chloride [61].

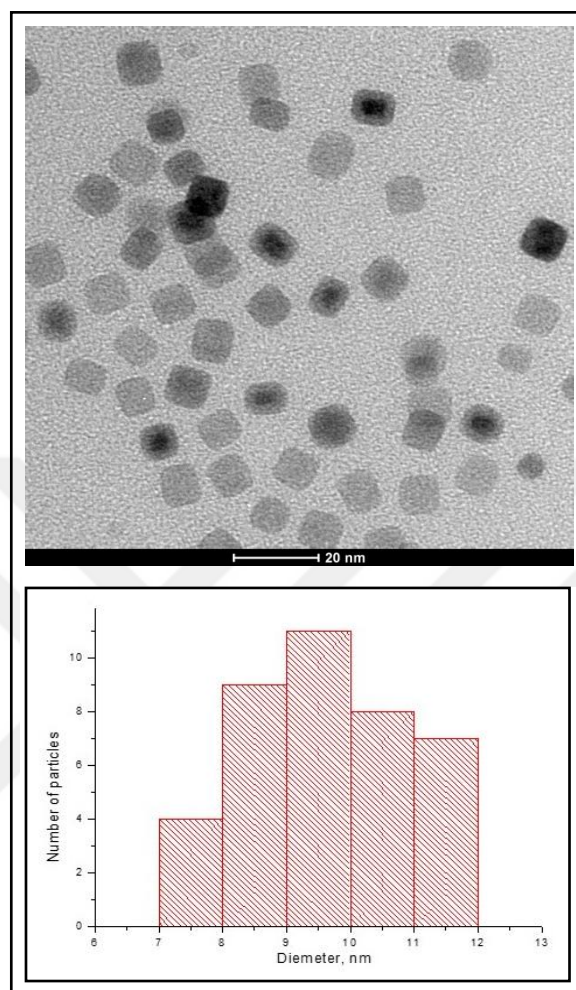


**Figure 38.** TEM images of cubic iron oxide nanoparticles that were synthesized by using Sodium oleate and NaCl. Corresponding size distribution histogram of the nanoparticles is given below the TEM image (Table 3,C)

TEM image of cubic shaped iron oxide nanoparticles is shown in Figure 38. According to TEM image, all of the iron oxide nanoparticles have cubic shape; they have narrow size distribution of 8-11 nm and average size of  $9.6 \pm 1.2$  nm. This appearance proves the effect of  $\text{Cl}^-$  on the formation of cubic shaped particles.

The behaviour of the cubic shape nanoparticles in the presence of a magnetic field is shown in Figure 39.

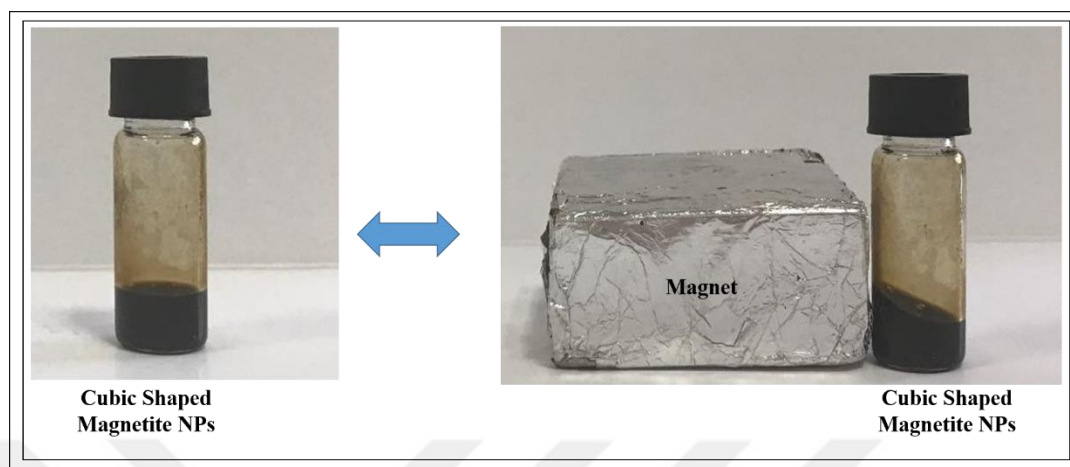


**Figure 39.** Behaviors of cubic shaped iron oxide nanoparticles near the magnet

As seen in the Figure 39, 60 seconds after they were placed next to the magnet, they were accumulated on the side of the magnet but they were not fully collected.

For structural characterization, XRD was used. Baseline corrected XRD pattern has been inserted to the original XRD pattern of cubic shaped iron oxide nanoparticles, Figure 40.

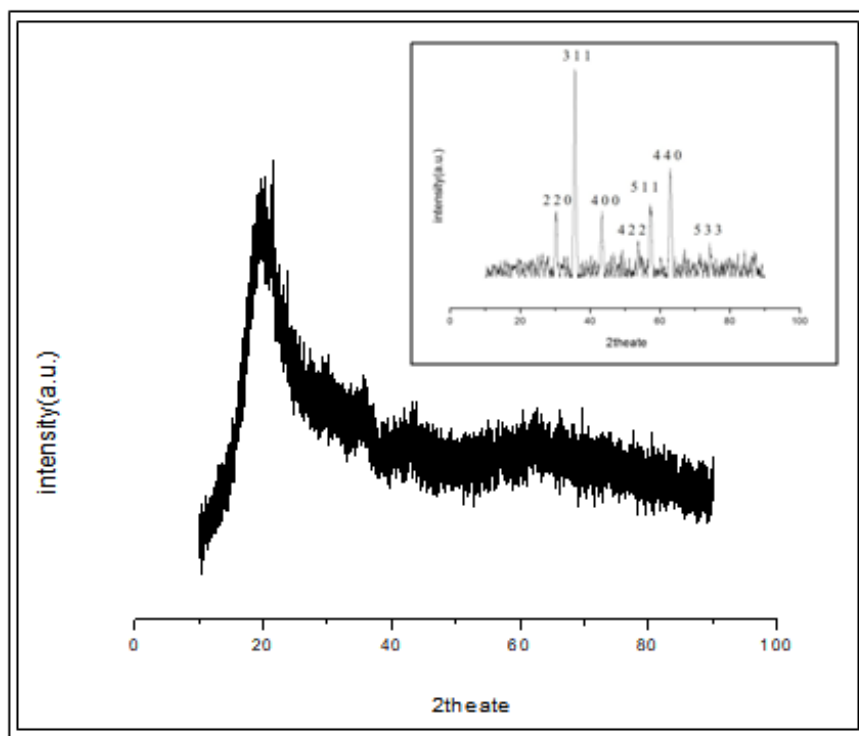


**Figure 40.** XRD pattern of cubic shaped iron oxide nanoparticles. Baseline corrected spectrum is inserted into graph

The characteristic peak of magnetite iron oxide is shown at XRD pattern (Figure 40). The analysis was carried out between angular range at  $10^\circ \leq 2\theta \leq 90^\circ$  and Bragg's reflections of (2 2 0), (3 3 1), (4 0 0), (4 2 2), (5 1 1) and (4 4 0) appear at the values of  $2\theta$  :  $30.13^\circ$ ,  $35.81^\circ$ ,  $43.16^\circ$ ,  $53.48^\circ$ ,  $57.25^\circ$ ,  $62.72^\circ$ ,  $73.88^\circ$  respectively and they are matching with the characteristic  $2\theta$  values of magnetite, (JCPDS NO: 89-2810) [101].

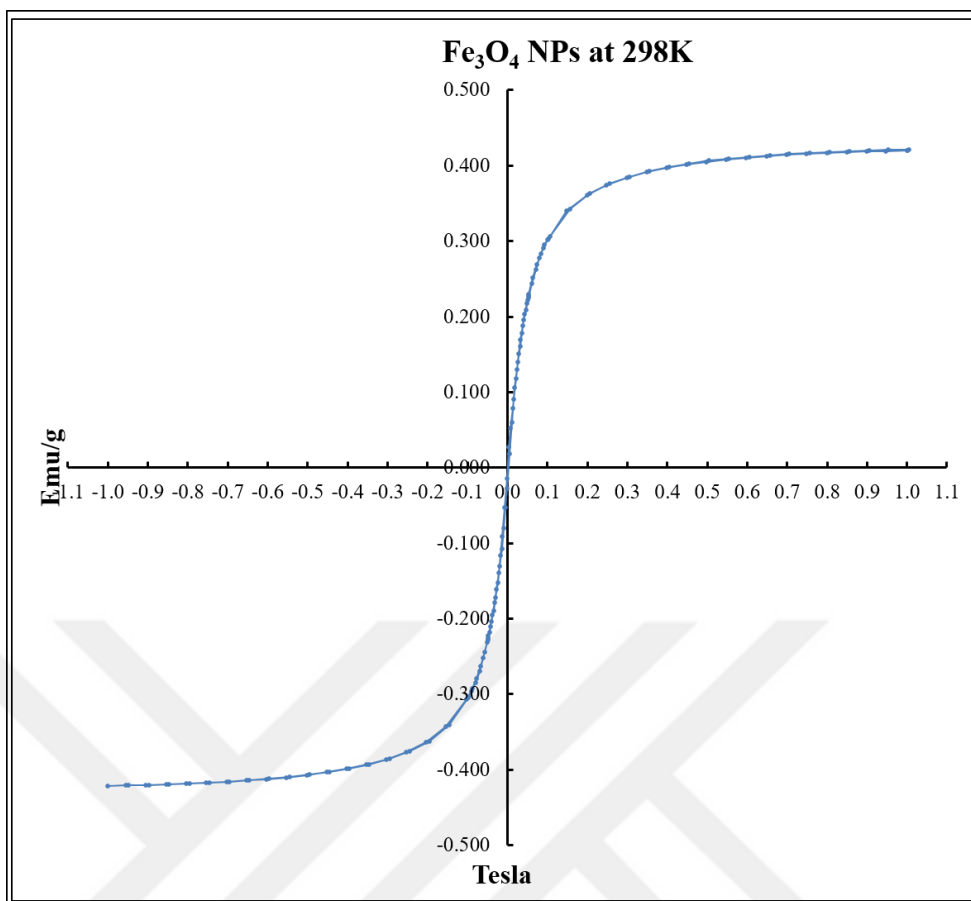


**Figure 41.** Magnetization versus magnetic field curves for cubic shaped iron oxide nanoparticles( Table 3C) at 298 K

Magnetization measurements were carried out with a field scan of  $\pm 1.1$ T at 298 K and 5 K. Magnetization versus magnetic field curves of the cubic shaped iron oxide nanoparticles (Table 3, C) at these two temperatures were prepared. Figure 41 shows the magnetic behaviour of the cubic shaped iron oxide nanoparticles measured at 298 K.

$M_s$  values of our cubic shaped iron oxide nanoparticles were also compared to that of the literature values. Generally  $M_s$  value for 10-20 nm magnetite iron oxide nanoparticles is greater than 1 emu/g [59]. Superparamagnetic behaviour were observed for cubic shaped iron oxide nanoparticles at 298K, Figure 41. As seen in the Figure, they have zero coercivity in the absence of a magnetic field. However,  $M_s$  value was too low, about 0.4 emu/g. This low result was probably related with the

difficulty that we had in the sample preparation step. Cubic shaped iron oxide nanoparticles could not be dried properly due to the presence of large amount of surfactant and liquid remained in the consistency of adhesive jelly. VSM measurement had to be done with powder sample instead of liquid sample. Possibly this physical difficulty affected the measurements negatively.

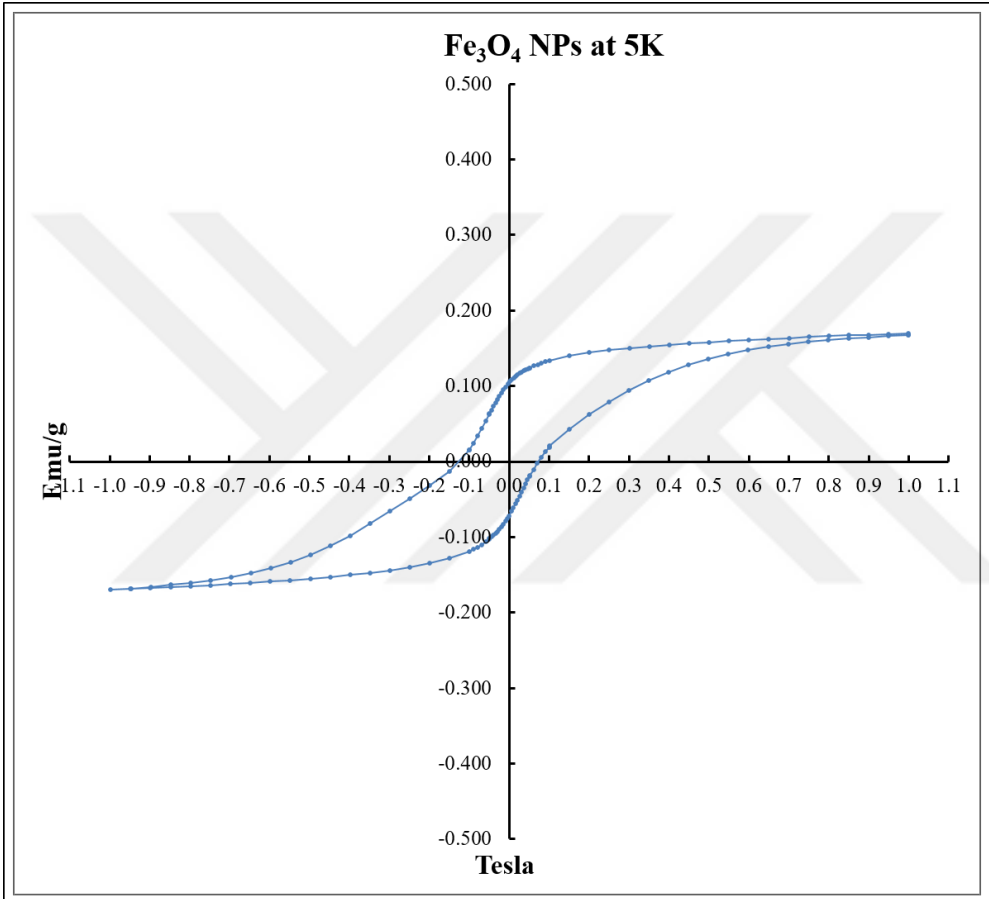


**Figure 42.** Magnetization versus magnetic field curves for cubic shaped iron oxide nanoparticles( Table 3,C) at 5K.

Figure 42 shows magnetization (Ms) as a function of applied magnetic field ( H ) for cubic shaped iron oxide nanoparticles. ( Table3,C) at 5K, below T<sub>b</sub> of cubic shaped magnetite nanoparticles (~270 K) [63].As expected our nanocubes do have hysteresis

at 5K. As can be seen from Figure 41  $M_s$  of nanocubes are 0.12 emu/g and their remanent magnetization ( $M_r$ ) is 0.1 emu/g. Actually,  $M_s$  should be over than 1 emu/g. Due to sampling problem and device sensitivity, results were not desirable. These magnetic measurements indicate that superparamagnetic cubic shaped magnetite nanoparticles were synthesized.

### 3.1.4.3 Conversion of Hydrophobic Cubic Shaped Iron Oxide Nanoparticles into Hydrophilic form

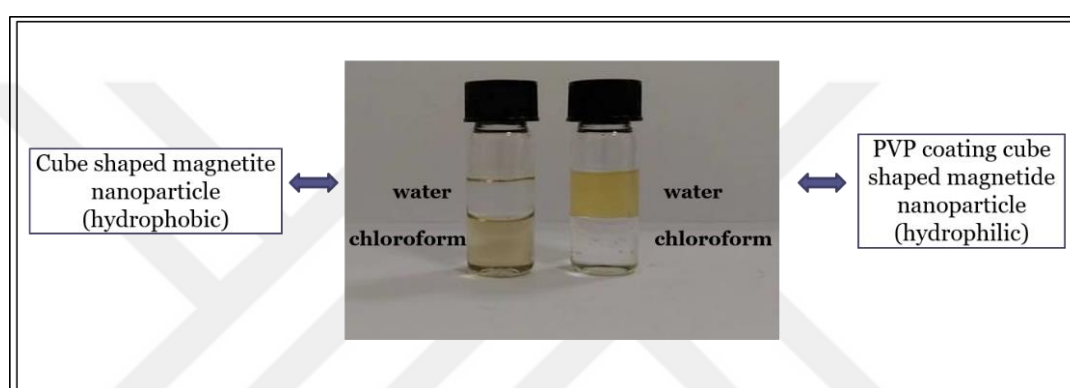


**Figure 43.** Cubic shaped magnetic nanoparticles dispersed in water phase after PVP coating

The hydrophobic surfaces of  $Fe_3O_4$  NPs were modified to exhibit hydrophilicity by adding an excess amount of amphiphilic PVP to cubic shaped MNPs so that the oleate ligand on MNPs could be exchanged with PVP. Following modification,  $Fe_3O_4$  NPs were able to be redispersed in hydrophilic solvents such as EtOH and water. As shown in Figure 43, PVP coated iron oxide nanoparticles are in the water phase whereas as prepared, hydrophobic ones, prefer to be in the chloroform phase. This property change indicates that the oleate ligands on  $Fe_3O_4$  NPs were successfully replaced by PVP [89].

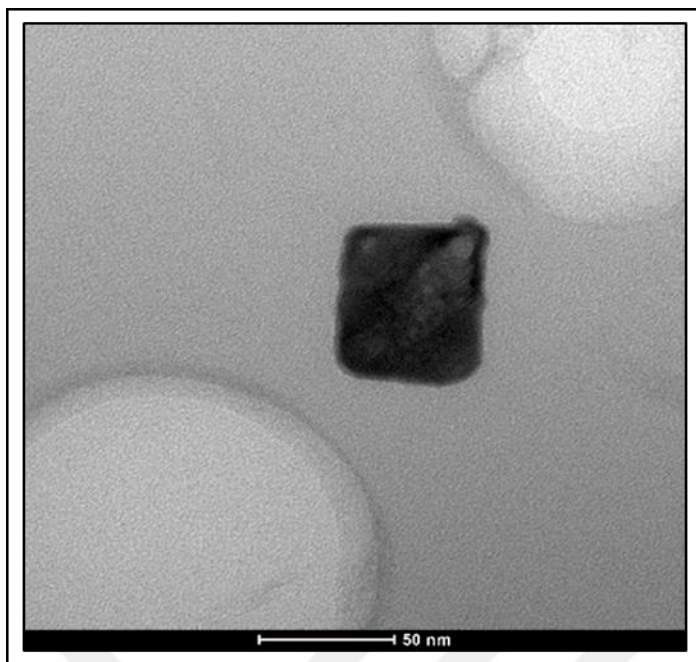


**Figure 44.** TEM image of PVP coated iron oxide nanoparticles

TEM image of PVP coated iron oxide nanoparticles are presented in Figure 44. 10 nm naked cubic shaped iron oxide nanoparticles were coated with 20nm PVP layer. After coating procedure, their geometrical properties were not changed. Moreover, any aggregation of the  $\text{Fe}_3\text{O}_4$  NPs was not detected after ligand exchange.



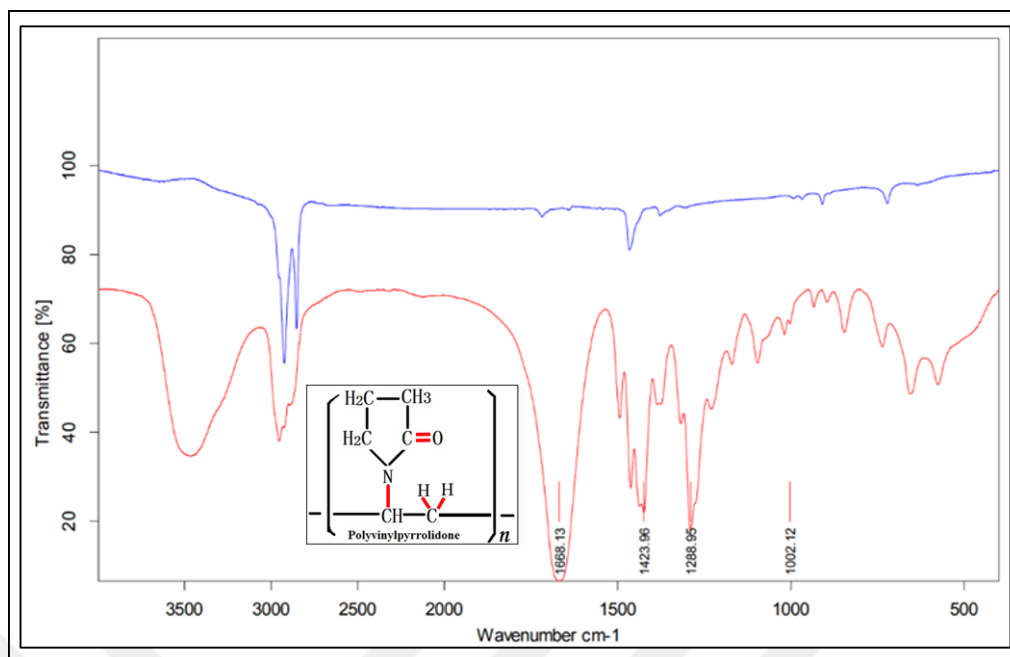


**Figure 45.** IR spectra of naked (blue line) and PVP coated (red line) iron oxide nanoparticles.

PVP coating process was further investigated with IR measurements. IR spectra of naked (blue line) and PVP coated (red line) cubic shaped iron oxide nanoparticles are given in Figure 45. The band at  $1668.13\text{ cm}^{-1}$  and  $1423\text{ cm}^{-1}$  represent C=O stretching vibration and  $\text{CH}_2$  bending, respectively. The bands at  $1288.95\text{ cm}^{-1}$  and  $1005\text{ cm}^{-1}$  are responsible for characteristic C-N stretching. Appearance of these new peaks indicate that cubic shaped hydrophobic iron oxide nanoparticles were coated with PVP successfully [102].

### 3.2 Preparation TPP-( $\text{CH}_2$ )<sub>3</sub>-OH and TPP-DCA

In this study, we purpose the attaching three phenyl phosphonium molecule (TPP) dichloroacetate molecule to increase intaken to mitochondria. Also TPP ion provide positive charge to drug for binding negatively charged nanoparticle surface. TPP-DCA molecule cold not supplied commercially. For this reason it should be synthesized.

### 3.2.1 Synthesis of TPP-(CH<sub>2</sub>)<sub>3</sub>-OH

DCA attached to TPP molecule via esterification reaction and alcohol reactant is needed for this reaction. For this reason, TPP was reacted with 3-bromopropan-ol.

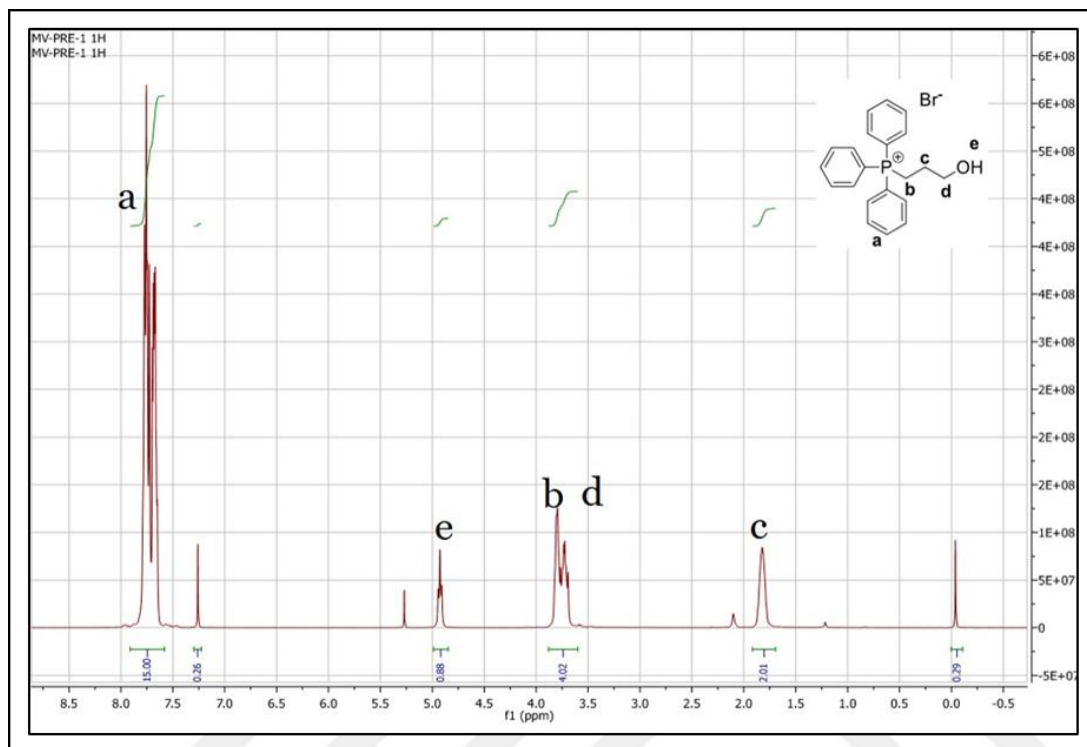


**Figure 46** <sup>1</sup>H-NMR spectrum of TPP-(CH<sub>2</sub>)<sub>3</sub>-OH precursor. <sup>1</sup>H NMR (400 MHz, CDCl<sub>3</sub>): δ 7.75 (m, 15H), 4.91 (t, 1H), 3.77 (m, 4H), 1.82 (m, 2H)).

The NMR spectrum of TPP-(CH<sub>2</sub>)<sub>3</sub>-OH is given in Figure 46. NMR spectrum confirms that the pure alcoholic precursor was obtained. The yield of the reaction was 61%.

### 3.2.2 Synthesis of TPP-DCA by Using Dichloroacetic Anhydride

Dichloroacetic anhydride used as a source of dichloroacetate. TPP-(CH<sub>2</sub>)<sub>3</sub>-OH makes a nucleophilic attack to one of carbonyl group of dichloroacetic anhydride and esterification reaction occurs. After 12 h stirring, bulky colorless to pale yellow product was obtained.

For purification study silica gel column was used. Before the purification study, in order to find the suitable solvent system, TLC studies were done. Dichloromethane (DCM), methanol, diethyl ether, acetonitrile, chloroform were used as solvent for separation-purification studies. We started with a solvent mixture, methanol: DCM (1:10), suggested by Pathak et al [91]. But the products were not separated from each other. Then the ratio of the components of the mixture were changed and also several different solvent mixtures were tried as eluent, Table 4.

**Table 4.** Solvent system that was used for TLC trials.

<b>Mobile phase</b>	<b>Ratio(mL/mL)</b>
DCM:Methanol	9:1
DCM:Methanol	2:1
DCM:Methanol	4:3
DCM:Acetonitrile	9:1
DCM:Diethyl ether	9:1
DCM:Ethanol	1:1
DCM:Methanol:Ethanol	4:2:1
DCM:Methanol:Ethanol	100:10:70

The appearances of the TLC plates under portable UV light (254 nm) after eluting with DCM ; ethanol and DCM ; ethanol; methanol mixtures are given in Figure 46. According to silica-TLC results, Figure 47, separation could not be observed, precursors and the product (TPP-DCA) were moving almost at the same speed, although, DCM: Methanol: Ethanol (100:10:70) system which has been purposed as the best solvent mixture used in silica column chromatography was used.

For characterization NMR Spectroscopy was used. H-NMR spectrum is shown in Figure 48.

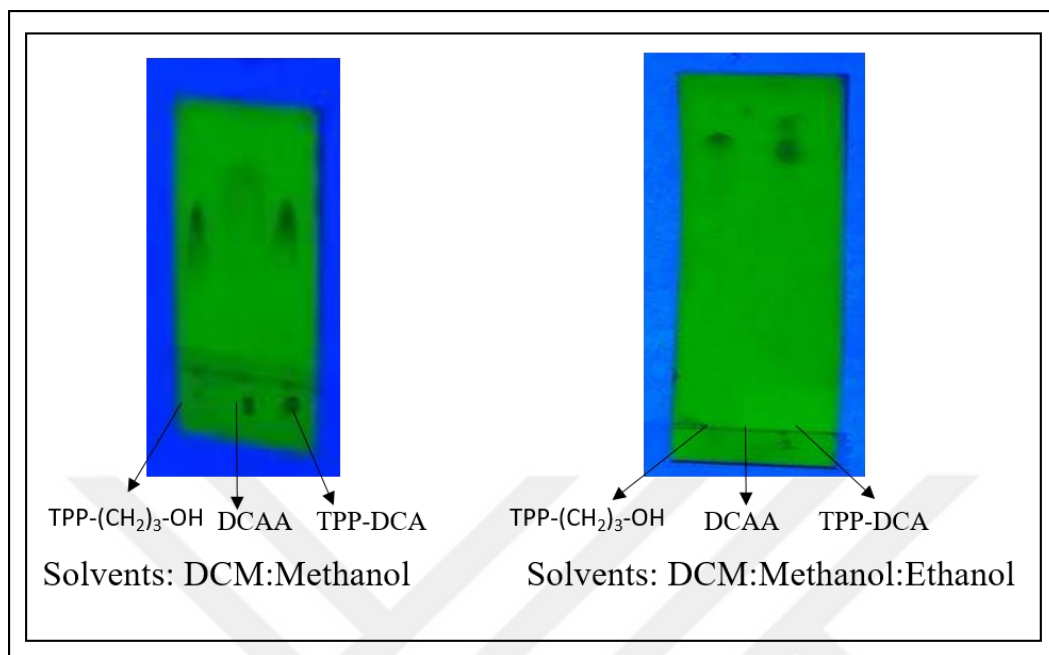


**Figure 47.** Appearance of TLC plate after DCM: Methanol: (90:10) and DCM: Methanol: Ethanol (100:10:70) solvent system were applied

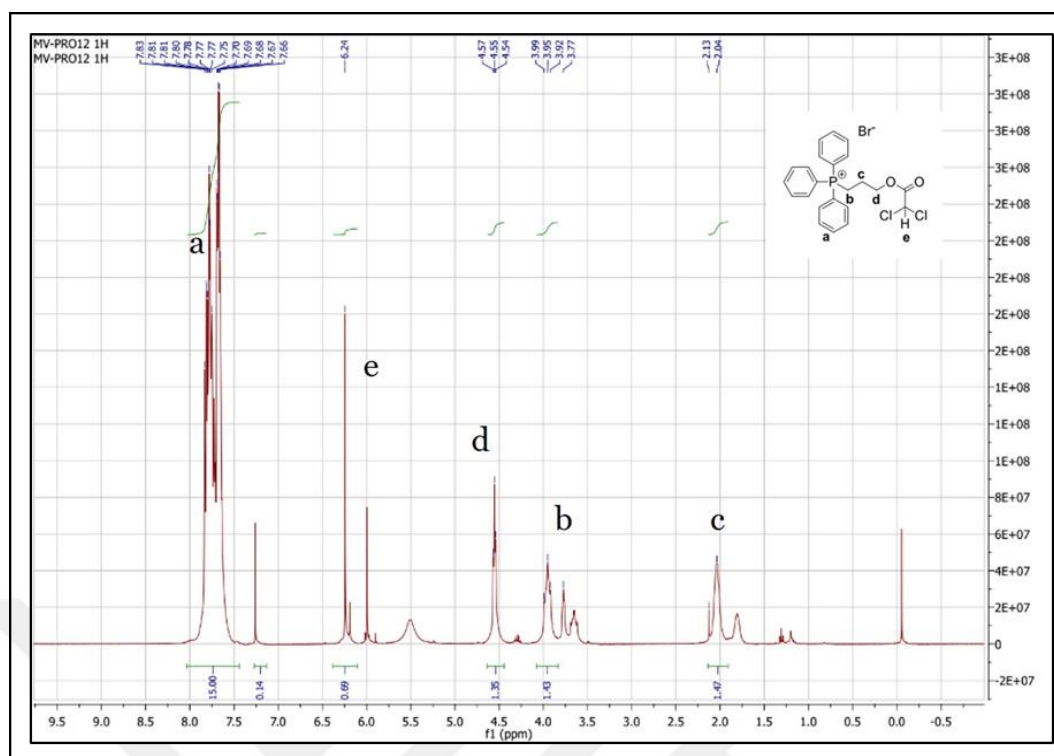


**Figure 48.** <sup>1</sup>H-NMR spectrum of TPP-DCA purified using silica-TLC plate with methanol-DCM (9:1) solvent mixture. The molecular formula of the expected product (TP-DCA) is given as inset and the corresponding peak positions are labeled (a-e). <sup>1</sup>H NMR (400 MHz, CDCl<sub>3</sub>) : δ 7.74 (dddd, 15H), 6.22 (d, 1H), 6.04 – 5.91 (m, 1H), 5.69 – 5.23 (m, 1H), 4.55 (t, J = 5.4 Hz, 2H), 3.95 (t, , 2H), 3.79 – 3.51 (m, 1H), 1.97 (dd, , 1H), 1.34 – 1.09 (m, 1H).

The shifts corresponding to the protons of the expected product were labelled with letters (a-e). The remaining shifts belong to impurities. NMR spectrum also indicated that separation process was not satisfactory.

Since the purification by the silica column method was ineffective, we decided to use preparative TLC method. Preparative TLC plates were prepared at the laboratory. Additionally new solvent couples such as acetone: DCM, acetonitrile: DCM, diethyl ether: DCM and ethyl acetate: DCM as eluents were prepared and their separation performances were examined in TLC for selecting the proper solvent for preparative TLC. The best separation was obtained by DCM and ethyl acetate mixture. Therefore

various volume ratios of DCM and ethyl acetate were tried. The appearances of the TLC plates after eluting with DCM and ethyl acetate mixtures, under portable UV light (254  $\lambda$  nm) are given in Figure 49.

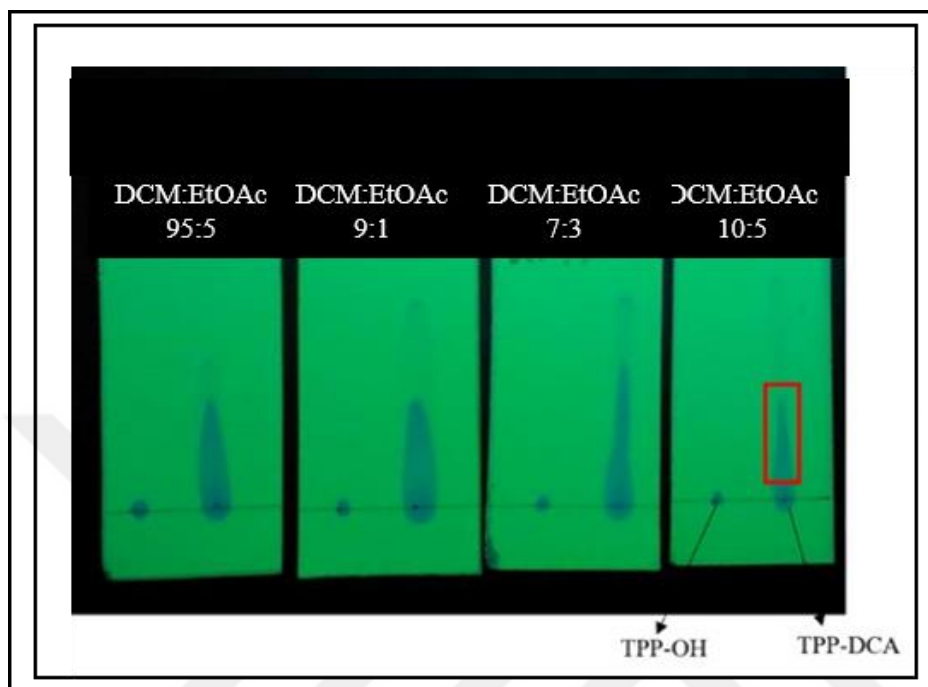


**Figure 49.** Purification of TPP-DCA utilizing TLC plate and DCM: ethyl acetate solvent mixture in various volume ratios 95:5, 9:5, 7:3 and 10:5.

According to the outputs given in Figure 49, the best separation of TPP-DCA from its precursors was observed in the last plate where DCM: ethyl acetate in 2:1 volume ratio was used as eluent. Therefore DCM: ethyl acetate in 2:1 volume ratio was decided to be used as eluent in the preparative TLC.



**Figure 50** Appearance of preparative TLC plate First plate image shows the thin line of the TPP-DCA prepared by using dichloroacetic anhydride, the last plate shows the separation of the same sample after running with DCM: ethylacetate in 2:1 (v/v)

A thin line of sample was deposited across pencil line Then the preparative TLC plate was place in the chamber having 20 mL of DCM: ethylacetate in 2:1 (v:v) as eluent. Follow in 30 mins the plate were removed and visualized under UV light. The two bands of the preparative TLC plate indicated by red frames in Figure 50 were scraped off and sonicated in DCM, then filtered through a glass cotton. The purified compounds were concentrated by evaporating under vacuum and yellow to colorless oily extracts were remained. Structural analyses of the extracts were done by utilizing NMR spectroscopy where  $\text{CDCl}_3$  was used as solvent, Figure 51 and Figure 52.

NMR spectrum of lower part (Red frame 1) is shown in Figure 51. All of the expected proton shifts indicated by letters (a-e) are observed. NMR shift at 4.12 and 1.26 belong to ethyl acetate which was used as mobile phase. According to NMR spectrum, pure product was obtained. The yield of the reaction was calculated as 48%. The product was kept under oxygen free medium. NMR spectrum of upper part (Red frame 2) is given in Figure 52

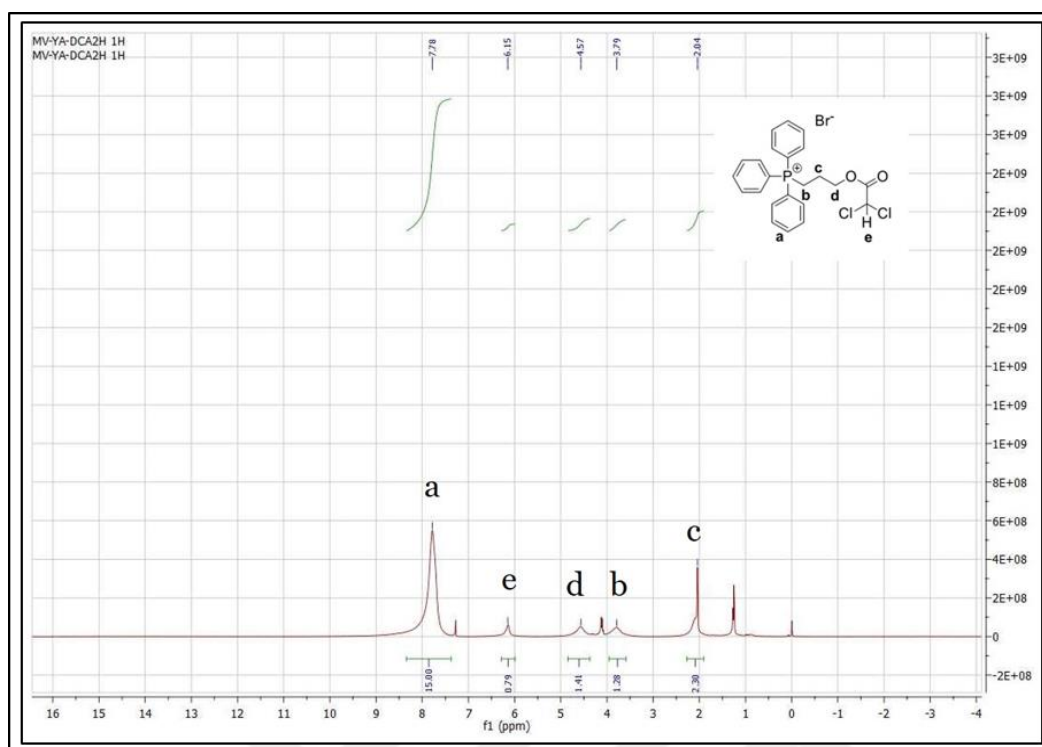


**Figure 51.** NMR spectrum of lower part (Red frame 1), TPP-DCA prepared with by using dichloroacetic anhydride. The structure of the the molecular formula of the expected product (TPP-DCA) is also given in the Figure and the position of the protons are labeled with lower case letters (a-e).  $^1\text{H}$  NMR (400 MHz,  $\text{CDCl}_3$ )  $\delta$  7.78 (s, 15H), 6.14 (s, 1H), 4.43 (d, H), 3.79 (s, 2H), 2.04 (s, 2H).



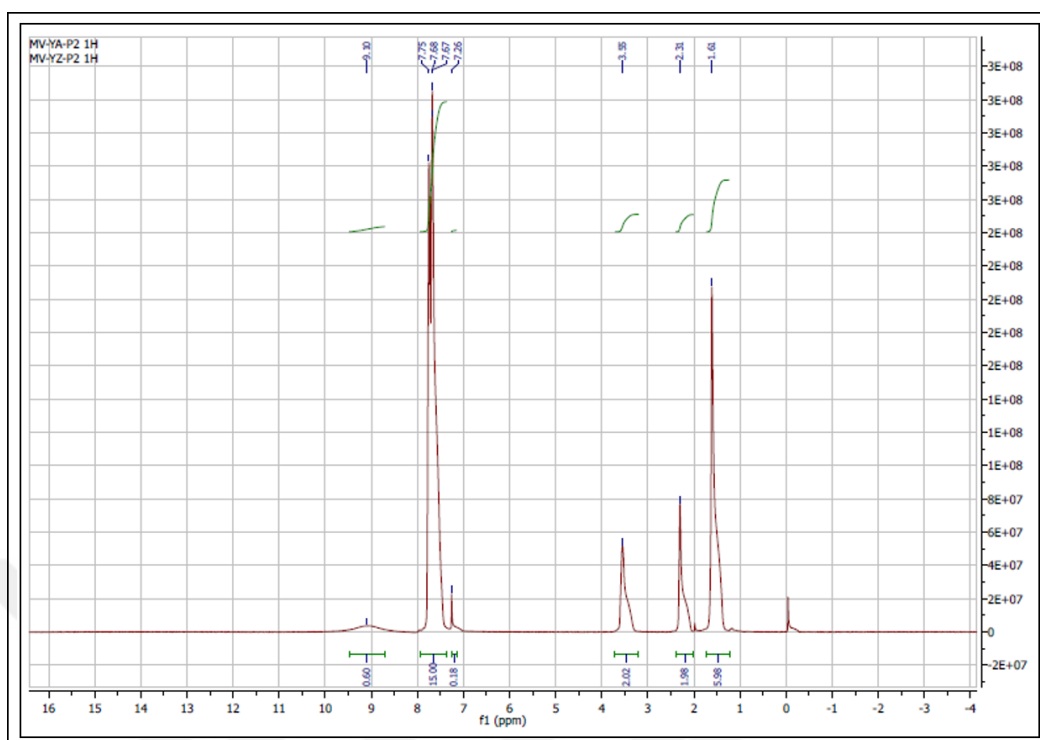


**Figure 52.** NMR spectrum of upper part (Red frame 2)

Although it was not identified properly the proton shift observed at 9.10 ppm indicates that this is an acidic species. The probable mechanism supporting acid formation is given below in Figure 53. Reaction mechanism indicates that dichloroacetic acid was formed as a side product. According to H-NMR spectrum in Figure 52, when upper red frame is taken mixture of acidic side product are obtained.

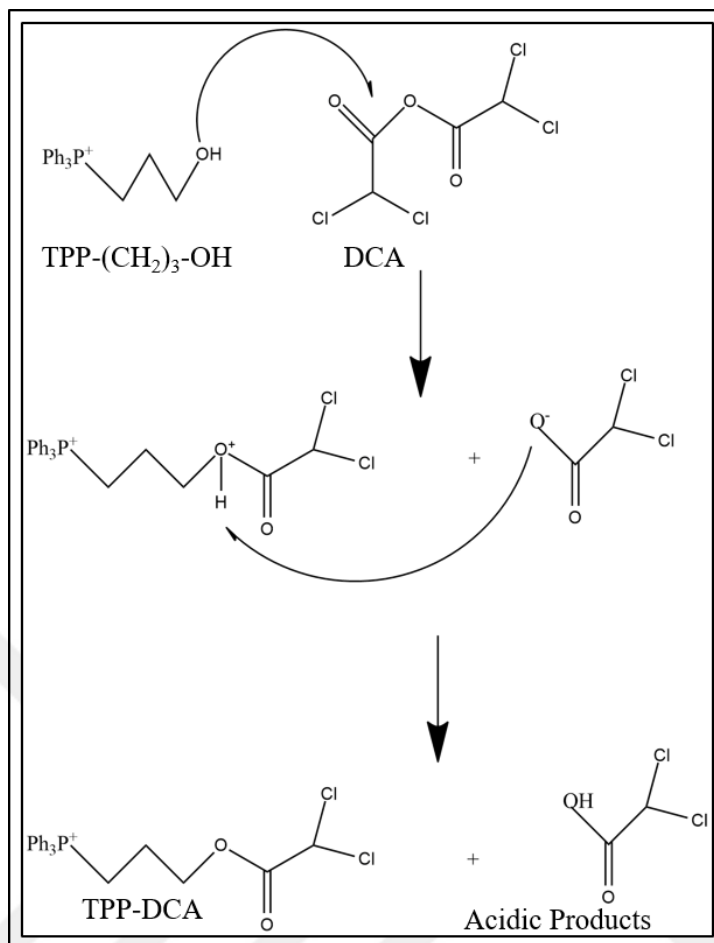


**Figure 53.** Mechanism of reaction of TPP-(CH<sub>2</sub>)<sub>3</sub>-OH and dichloroacetic anhydride

### 3.2.3 Synthesis of TPP-DCA by Using Dichloroacetylchloride

It is very difficult to obtain dichloroacetic anhydride from chemical companies. Since it is used in the synthesis of narcotic material, its supplying requires strict permits. Additionally, it is expensive and esterification reaction is slow, on the other hand dichloroacetyl chloride is more reactive than dichloroacetic anhydride so that the reaction can be completed within five minutes instead of twelve hours. In addition, in comparison, it is inexpensive than dichloroacetic anhydride. For this reason, dichloroacetyl chloride was used as dichloroacetate source.

For purification studies, preparative TLC methods with the same solvent system (DCM: ethyl acetate, 2:1) were used and similar results were obtained (Figure 54).

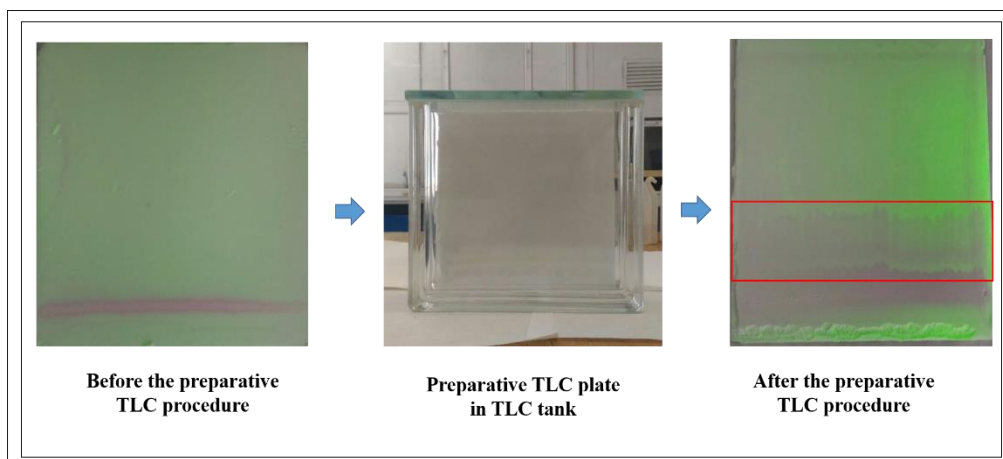


**Figure 54.** Appearance of preparative TLC .First plate image shows the thin line of the TPP-DCA prepared by using Dichloroacetylchloride, the last plate shows the separation of the same sample after running with DCM: ethylacetate in 2:1 (v:v).

For structural characterization, NMR Spectroscopy was used. NMR spectra are shown in Figure 55.

All of the expected proton shifts indicated by letters (a-e) are observed. NMR shift at 4.12 and 1.26 belong to ethylacetate which was used as mobile phase. According to NMR spectrum, pure product was obtained. The yield of the reaction was calculated as 28%. The product was kept under oxygen free medium.

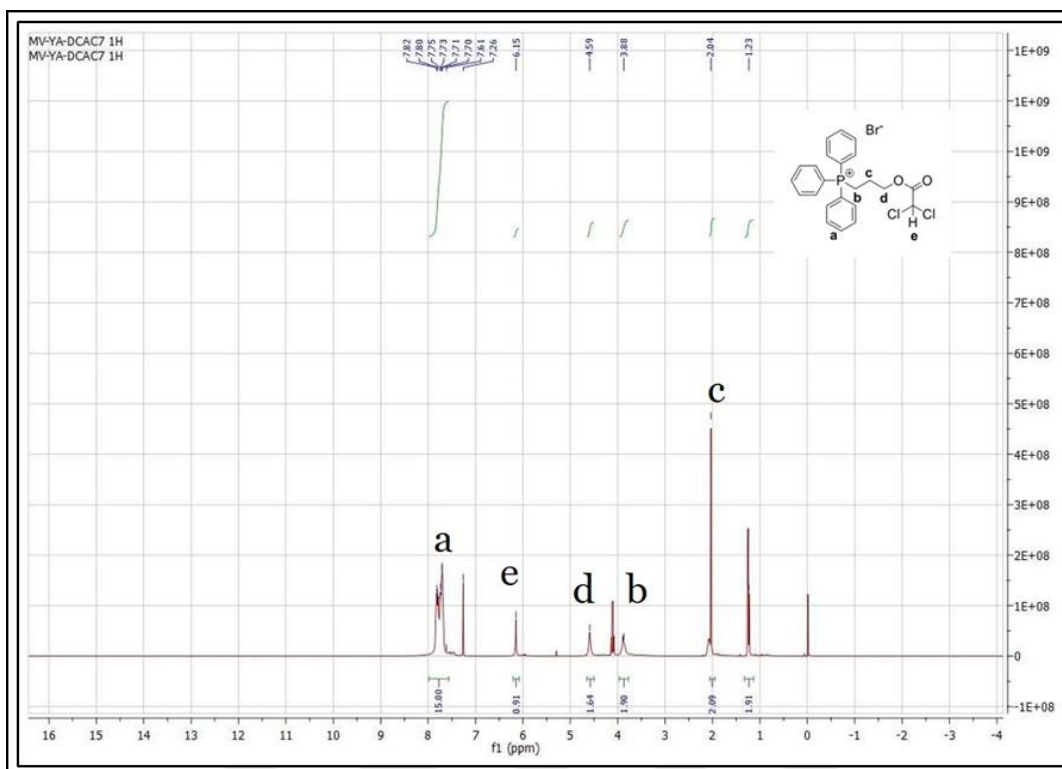


**Figure 55.** NMR spectrum of TPP-DCA prepared by using Dichloroacetylchloride. The molecular formula of the expected product (TPP-DCA) is also given in the Figure and the position of the protons are labeled with lower case letters (a-e)..  $^1\text{H}$  NMR (400 MHz,  $\text{CDCl}_3$ )  $\delta$  7.94 – 7.57 (m, 15H), 6.15 (s, 1H), 4.59 (s, 2H), 3.89 (s, 2H), 2.17 – 1.86 (m, 3H).

### 3.3 Modification of iron oxide Nanoparticles for Biomedical Applications

At this part, hyperthermia measurements and particle modification studies were purposed to carry on at same time. According to literature, large particles ( $>10$  nm) have higher heating efficiency than smaller iron oxide particles at same conditions [103]. For this reason, spherical iron oxide nanoparticles which have 13.6 nm size average, were used firstly for modification studies. After optimization studies will be handled, same modification, hyperthermia and biologic experiments will be applied for flower and cubic shaped iron oxide nanoparticles.

### 3.3.1 Heparin Coating

The various procedure can be applied for coating surface of magnetic nanoparticles with heparin. By applying coupling reaction with EDC/NHS reagents, the carboxylate group of heparin can be bonded to aminated magnetic nanoparticles from the amine group [104]. Another procedure is based on electrostatic interaction. Negatively charged heparin molecules are attached to the positively charged surface of magnetic nanoparticles [105]. In this study, electrostatic interaction approach was used (Figure 56).

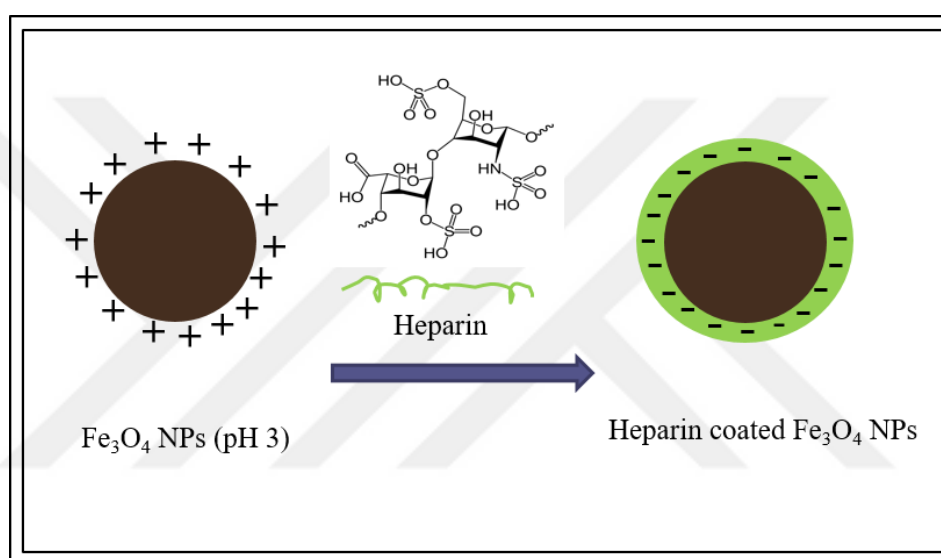


**Figure 56.** Scheme for coating of iron oxide nanoparticles with negatively charged heparin.

For characterization studies Transmission Electron Microscopy, Infrared Spectrophotometer and Zeta potential measurement device were used.

Zeta potential measurement results are summarized in Table 5. Naked iron oxide nanoparticles were treated with nitric acid solution to render their surface positively charged. After acid treatment of magnetite NPs surface charge was changed from  $1.85 \pm 0.61$  mV to  $33.34 \pm 2.35$  mV. This increase of the zeta potential in the positive direction was indicating that -OH groups were changed to  $-\text{OH}_2^+$ .

**Table 5.** Table of zeta potential measurements.

Sample	Zeta potential value(mV)
Naked magnetite NPs solution	1.85±0.61
Naked magnetite NPs solution (pH=3)	33.34±2.5
Heparin Coated magnetite NPs solution	-42.57± 2.14

After heparin coating procedure zeta potential of magnetite nanoparticles were measured again and found as  $-42.57 \pm 2.14$  mV. Similar results were reported in the literature [104][106]. The increase of zeta potential in negative direction was correlated to the presence of negatively charged sulphate groups of heparin on magnetite nanoparticle's surface. High negative charge on the surface of the nanoparticles also brings colloidal stability and decreases the tendency of agglomeration [106]. TEM image of heparin coated nanoparticles is given in Figure 57.

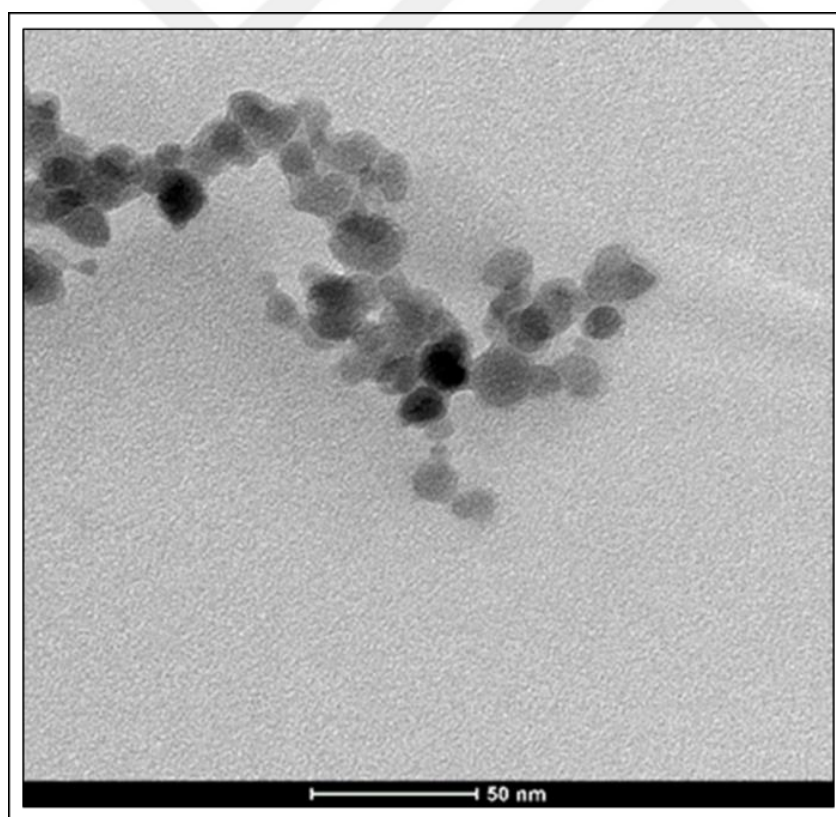


**Figure 57.** TEM image of heparin coated spherical iron oxide nanoparticles

According to TEM image, thin heparin layer has been coated on the surface of magnetite nanoparticles. The thickness of heparin layer measured is about  $2.9 \pm 0.9$  nm. Heparin coating on magnetite nanoparticles was further investigated through IR measurements. FT-IR Spectra is given below in Figure 58.

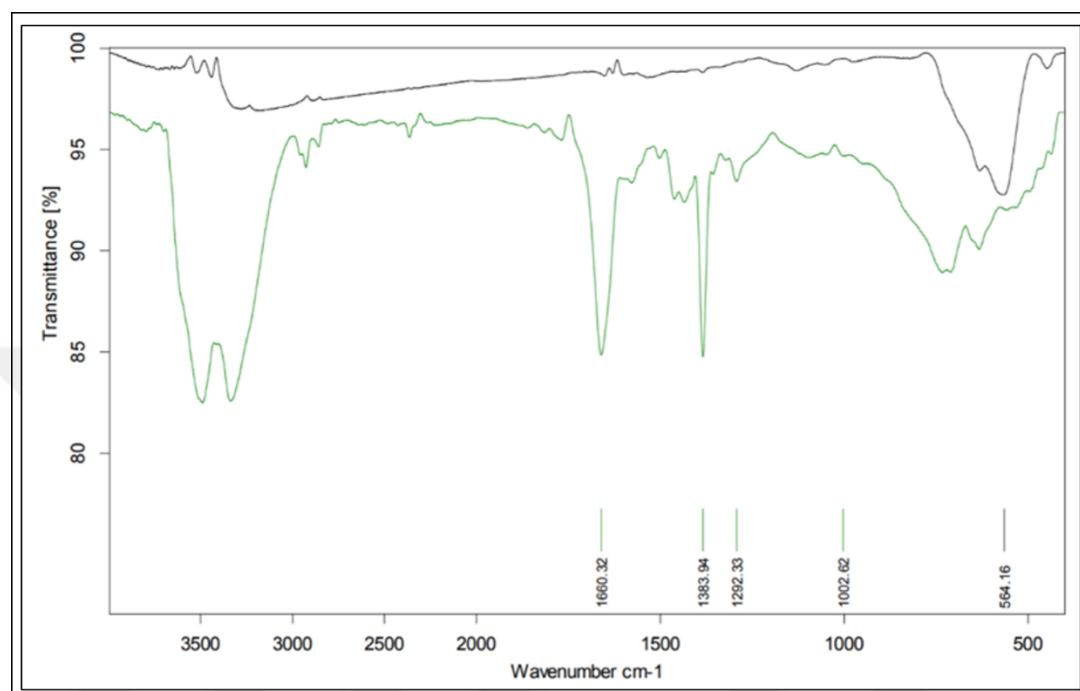


**Figure 58** IR spectra of naked (black line) and heparin coated (green line) iron oxide nanoparticles

While black line depicts naked magnetite nanoparticle, the green line represents heparin coated magnetite nanoparticles. There are several peaks in the spectrum of the heparin coated particles that are not seen on the spectrum of a naked one. Among them,  $1292 \text{ cm}^{-1}$  and  $1002.62 \text{ cm}^{-1}$  peaks belong to symmetrical and asymmetrical stretching of S=O in  $\text{NH-SO}_3$ , respectively. In addition, the stretching of the C=O and N-H bonds are observed at  $1662.22 \text{ cm}^{-1}$ , and  $1383.95 \text{ cm}^{-1}$  respectively [107].

These results confirm that heparin was successfully coated on the surface of iron oxide nanoparticles.

### 3.3.2 Attaching TPP-DCA to Heparin Coated Iron Oxide Surface

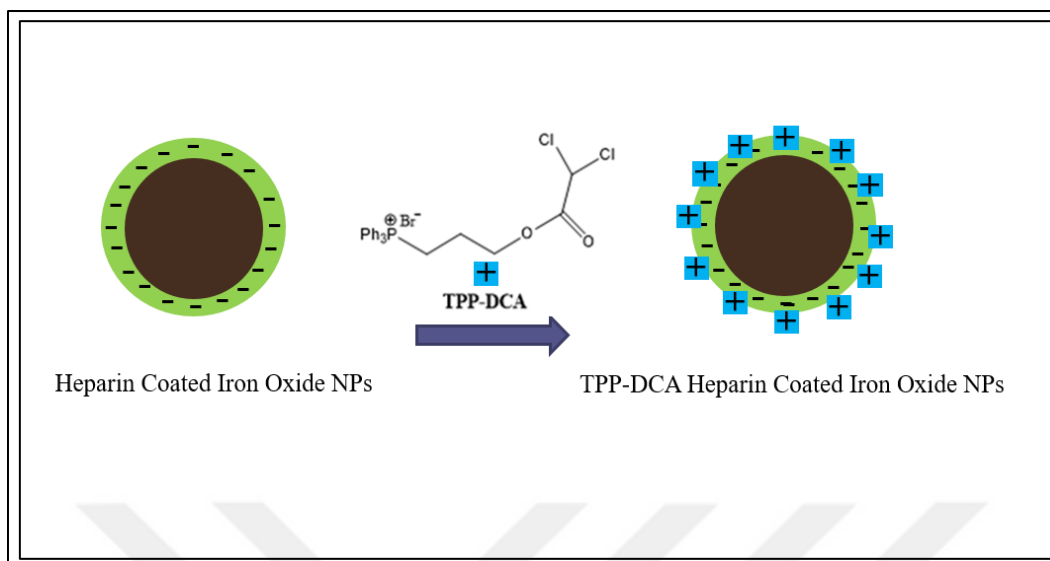


**Figure 59.** Scheme for the immobilization of positively charged TPP-DCA on to negatively charged heparin coated iron oxide nanoparticles.

For the immobilization, again the electrostatic attraction principle was used (Figure 59). We kept the amount of heparin coated iron oxide nanoparticles fixed as 9 mg for each time and 4.0 mL, 6.0 mL and 8.0 mL (1mg/mL) TPP-DCA solutions were added to 25 mL aqueous solutions of the nanoparticles. The presence of TPP-DCA on the surface was characterized by zeta potential and FTIR measurements. First of all Zeta Potentials were measured. We were expecting that the added positively charged TPP-DCA would neutralize the negative charge of the surface imparted by heparin either fully or partially. Measured potential values were  $24.2 \pm 0.5$  mV,  $-20.9 \pm 0.4$  mV,  $-12.9 \pm 1.2$  mV corresponding to the addition of 4 mL, 6 mL and 8 mL of (1mg/mL) TPP-DCA solutions respectively. The change of zeta potentials from  $-42.57 \pm 2.14$  mV to less negative (positive side) values following the increase in the amount of TPP-DCA was accepted as a confirmation of TPP-DCA loading. Additionally, after coating procedure, the dispersity of nanoparticles was decreased and agglomeration was observed. This observation was also supporting our hypothesis because the magnetic attraction among magnetic nanoparticles became stronger than that of electrostatic repulsion due to the decrease in negative zeta potential values when the volume of



(1mg/mL) TPP-DCA solution was increased above 8mL, probably due to agglomeration, meaningful results were not obtained. So this study was carried on by loading 8 mL (1mg/mL) TPP-DCA solution to 9mg iron oxide nanoparticles.

FTIR spectra, at Figure 60, indicates that TPP-DCA molecules were attached to heparin coated magnetite nanoparticles. The blue line and green line belong to heparin coated magnetite nanoparticles and TPP-DCA modified heparin coated magnetite nanoparticles, respectively.

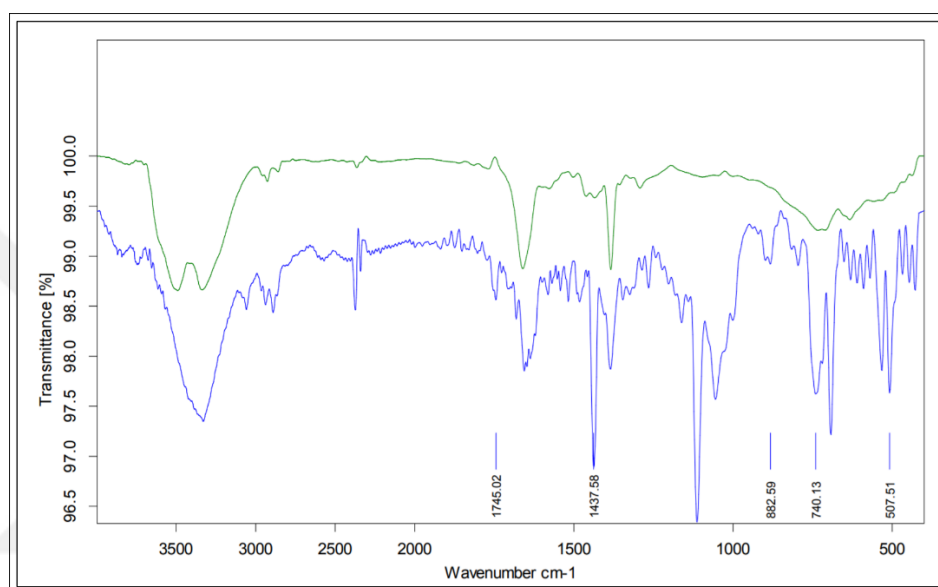


**Figure 60.** IR spectra of heparin coated (green line) and TPP-DCA attached heparin coated (blue line) iron oxide nanoparticles.

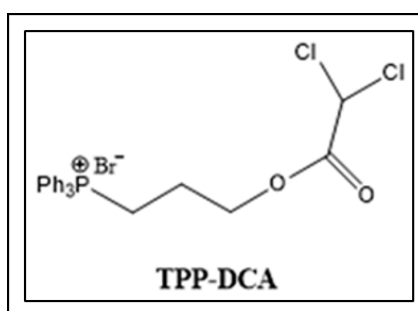


**Figure 61.** Chemical structure of TPP-DCA

The molecular structure of TPP-DCA molecule is shown in Figure 61. TPP-DCA molecule has C-Cl, C-P and phenyl groups that all have characteristic IR peaks for the

identification. Dichloroacetate side has bands at  $1745\text{ cm}^{-1}$  and  $882\text{ cm}^{-1}$ , these are corresponding to the C=O stretching and C-Cl stretching, respectively [108]. The bands at  $1437\text{ cm}^{-1}$  and  $740\text{ cm}^{-1}$  are matching to phenyl groups, The band at  $493\text{ cm}^{-1}$  is related to the asymmetric stretching of P- C bond at TPP side of TPP-DCA molecule [109].

### 3.3.3 Embedding TPP-DCA into Heparin Layer

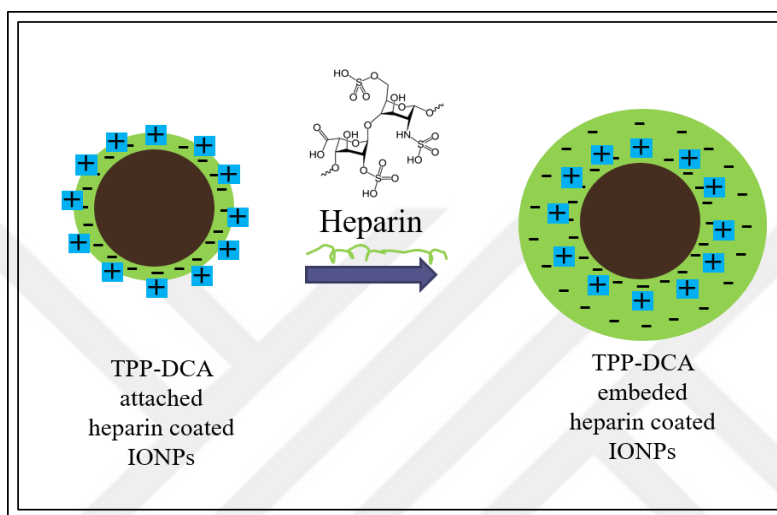


**Figure 62.** Scheme of heparin coating procedure (second time) TPP-DCA attached heparin coated iron oxide nanoparticles and changing of surface charge

For characterization studies, zeta potential measurements, transmission electron microscopy, and thermal gravimetric analysis techniques were used. According to zeta potential measurements results, the charge of particle surface changed from  $-12.9 \pm 1.2\text{ mV}$  to  $-42.52 \pm 2.15\text{ mV}$ . Increasing of negative charge on particle surface confirms the heparin coating particle surface second time is satisfactory (Figure 62).

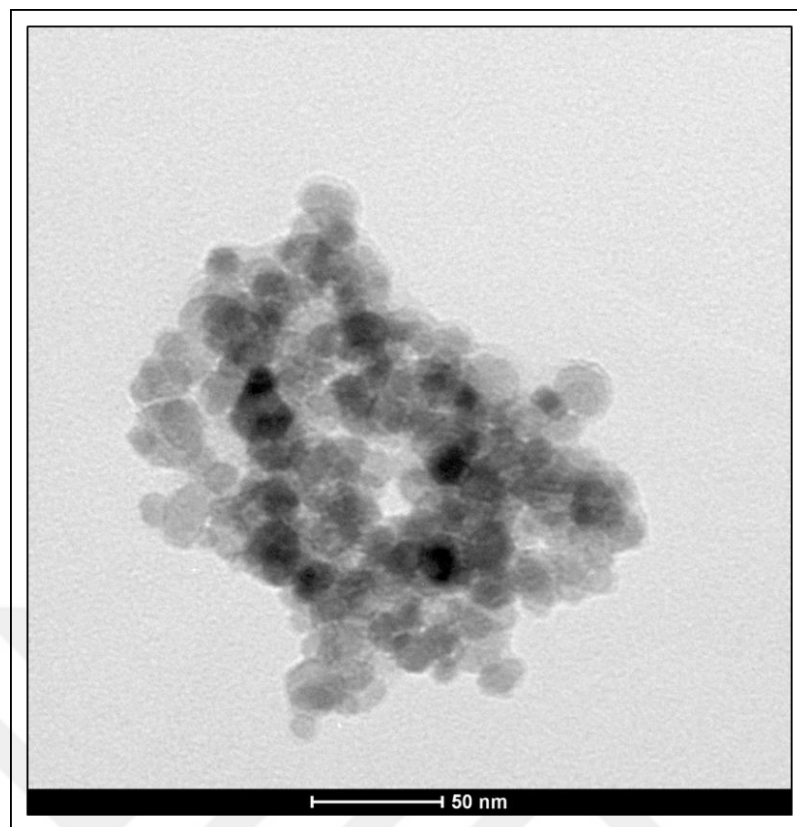


**Figure 63.** TEM image of 2-DG-HEP-TPP-DCA-HEP coated IONPs

Figure 63 depicts the TEM images of 2-DG-HEP-TPP-DCA-HEP coated IONP. TEM sample was prepared with dipping method. According to TEM image thickness of heparin, shell was measured about  $4.8 \pm 0.9$  nm. At Figure 55, TEM image belongs to one layer heparin coated IONPs One layer shell thickness had been measured  $2.9 \pm 0.9$  nm. This results confirm that IONPs were coated with second layer with heparin.

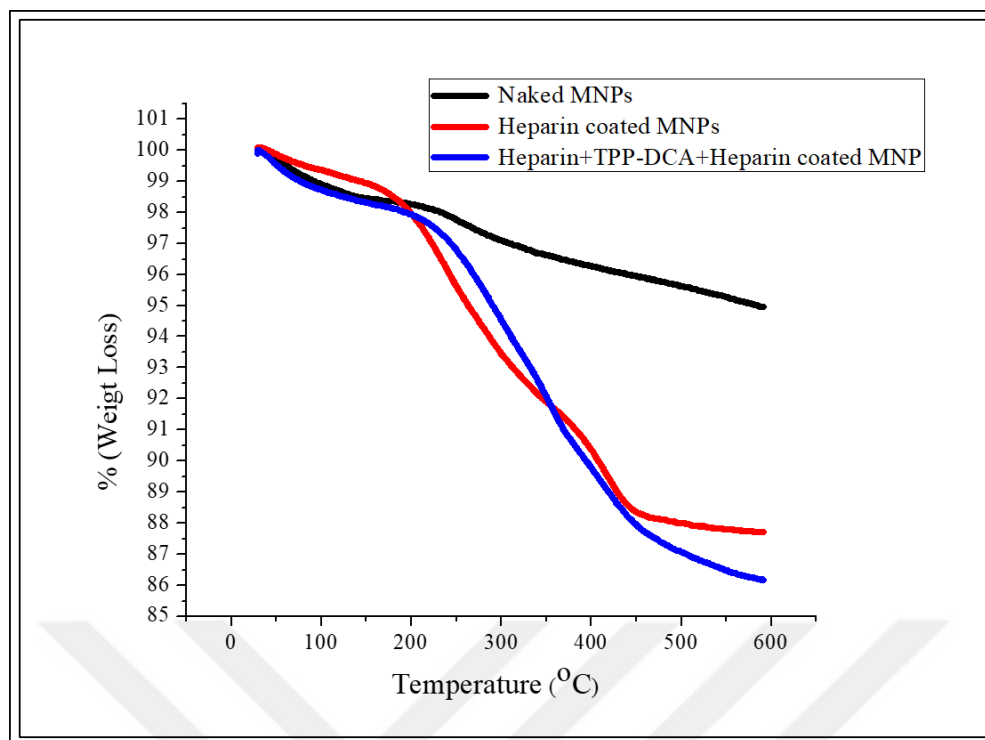


**Figure 64.** TGA curve of0 naked iron oxide (black line), single layer heparin coated iron oxide nanoparticles (red line) and double layer heparin coated and TPP-DCA loaded iron oxide nanoparticles (blue line).

Presence of heparin on the iron oxide nanoparticles surface was also investigated by TGA analysis, Figure 64. The black line represents TGA curve of naked iron oxide, red and blue lines are corresponding to single layer heparin coated and double layer heparin coated and TPP-DCA loaded iron oxide nanoparticles respectively Analyses was carried out at 25 °C to 600 °C. Due to organic compound, only 3.5 % weight loss was observed for naked iron oxide particles. On the other hand, 11.5 % and 14% weight loss were measured for single layer and double layer heparin coated and TPP-DCA loaded iron oxide nanoparticles, respectively. These results confirm that 8% and 10.5% of the total mass is corresponding to single layer heparin and double layer heparin containing TPP-DCA [110].

### **3.3.4 Determination 2-Deoxy-d-glucose By Cupric Reduction Based Methods**

100 microliter of the sample was taken and it was diluted according to the proposed method. The final solution was used for the determination. The handled UV-Vis spectra was on.

The absorbance at 455 nm was 0.0507 A. From the calibration curve equation, the concentration of D-Glucosamine on 150  $\mu$ l nanoparticle (1mg Fe<sub>3</sub>O<sub>4</sub>/mL) surface was calculated as 4.86x10<sup>-6</sup> M. (All measurements were done by 3 replicates, and the net values calculated as their mean values.)

## **3.4 Biological Experiments**

### **3.4.1 XTT Cell Cytotoxicity Assay**

The cytotoxic effects of 2-DG-HEP-TPPDCA-HEP coated IONPs on HepG2 cell line were investigated by XTT cell viability assay.

Cell viability for each concentration was indicated as percentage viability (%), assuming that the control well is 100 % viable. Also, cultured wells without cells were used to avoid the effect of samples on absorption which could be misleading.

First experiments were carried out without a washing (pre-wash) procedure. As seen in Figure 65, the light microscopy image of DC and different concentrated nanoparticles treated HepG2, the accumulation of nanoparticles in the environment of cell increases as the concentration of nanoparticles increases.

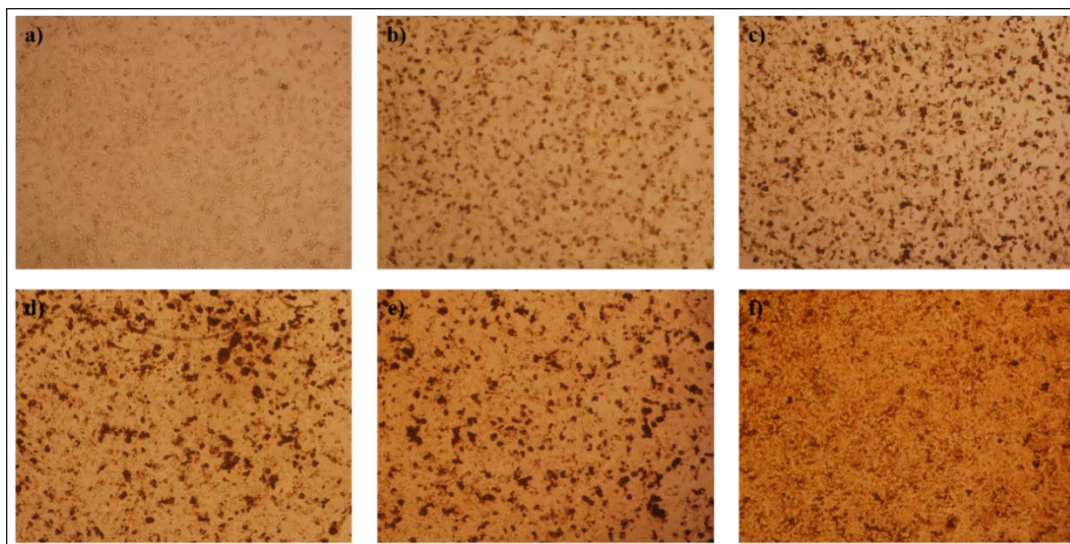


**Figure 65.** Light microscopy images of a) DC, b) 50 µg/ml, c) 250 µg/ml, d) 500 µg/ml, e) 750 µg/ml and 1000 µg/ml 2-DG-HEP-TPPDCA-HEP coated IONPs treated HepG2 cells after 24-hour treatment without pre-wash.

The effect of 24-hour treatment of 2-DG-HEP-TPPDCA-HEP coated IONP on HepG2 cells were investigated in a dose dependent manner. Cell viability percentages were plotted for each concentration and given in Figure 66.

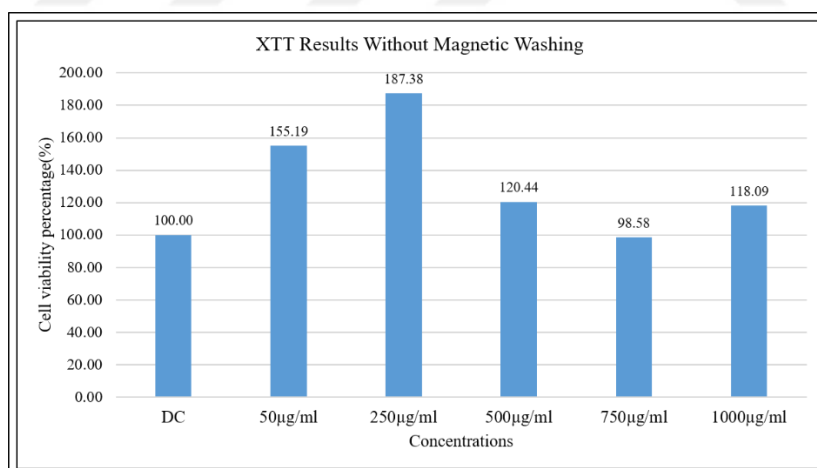


**Figure 66.** XTT results of a) DC, b) 50 µg/ml, c) 250 µg/ml, d) 500 µg/ml, e) 750µg/ml and f) 1000µg/ml 2-DG-HEP-TPPDCA-HEP coated IONPs treated HepG2 cells after 24-hour treatment without washing (pre-wash) procedure

The cell viability was expected to decrease directly proportional to the particle concentration. However, as seen from the figure, this trend was not observed. Agglomeration of iron oxide nanoparticles effected the ELISA reading and caused an extra background absorption.

In order to handle this incorrect measurements, cells were washed with PBS buffer via magnet after 24-h treatment and the results are given in Figure 67.

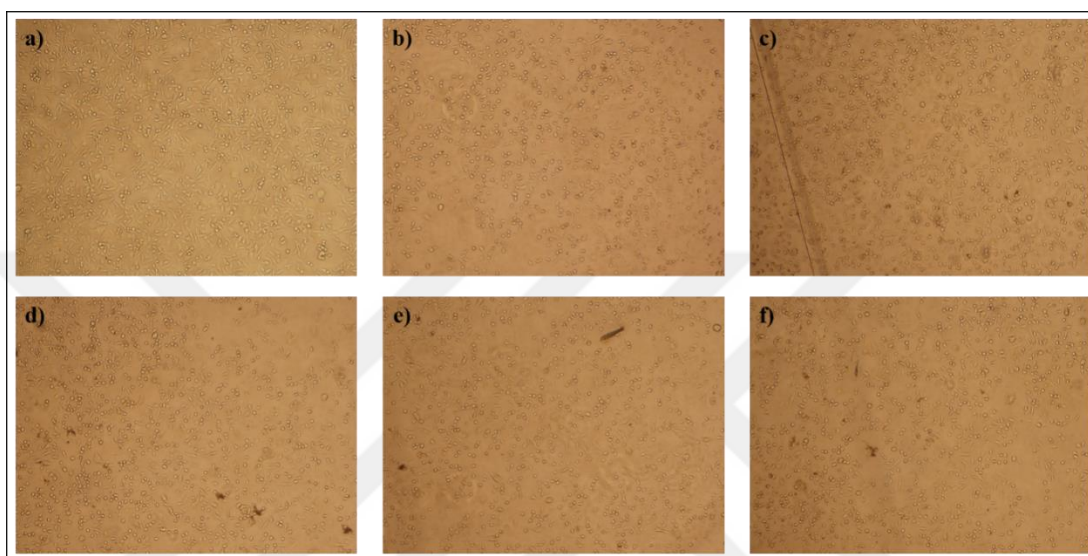


**Figure 67.** Light microscopy images of a) DC, b) 125 µg/ml, c) 250 µg/ml, d) 375 µg/ml, e) 500µg/ml and f) 750µg/ml 2-DG-HEP-TPP-DCA-HEP coated IONPs treated HepG2 cells after 24-hour treatment with washing procedure.

As seen from the light microscopy images, agglomeration of magnetic nanoparticles decreased and cells were not damaged by the magnet. Comparing the DC control cell images (Figure 67) showed the decreasing number of cells with 125 µg/ml, 250 µg/ml, 375 µg/ml, 500µg/ml and 750µg/ml (Figure 67 b, c, d, e and f) 2-DG-HEP-TPPDCA-HEP coated IONPs treatments. As the concentration increased, cell viability decreased.

XTT measurements, given in Figure 68, confirmed the microscope images. A decrease in the cell viability trend which is proportional to nanoparticle concentrations were observed.

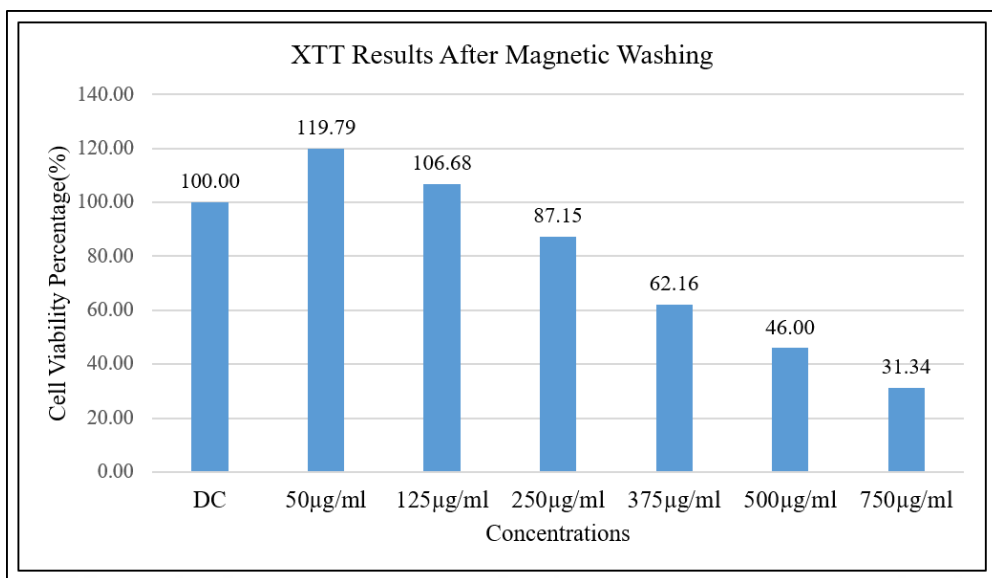


**Figure 68.** XTT results of a) DC, b) 125 µg/ml, c) 250 µg/ml, d) 375 µg/ml, e) 500 µg/ml and f) 750 µg/ml 2-DG-HEP-TPP-DCA-HEP coated IONPs treated HepG2 cells after 24-hour treatment with washing procedure.

IC<sub>50</sub> value for the 24 hr treatment of 2-DG-HEP-TPPDCA-HEP coated IONP, that is a concentration at which 50% of cells are alive, were calculated as 525 µg/ml. After other confirming experiments, this concentration will be used.

XTT tetrazolium (pink) salt which is used in cell viability assay is reduced by succinate in the presence of mitochondrial succinate dehydrogenase and converted to XTT formazan which has orange colour. When the cells die, this colour change cannot be observed because mitochondrial activity will also stop. Our XTT results also provide the collapse of mitochondrial metabolism when the TPP-DCA loaded IONPs are taken into the cell.

### 3.4.2 Viable Cell Counting with Trypan Blue Exclusion Method

Trypan blue exclusion method (TBE) was performed in order to compare XTT cell viability assay results and also to eliminate any absorbance interference caused by the nanoparticle solution.



The logic of the Trypan Blue Exclusion method lies behind the permeability of the cell membrane. Cells with disrupted membranes that are generally dead cells allow the dye to enter into the cells, so dead cells are observed in blue whereas healthy cells with undamaged membrane is seen as transparent since the dye cannot penetrate through intact membrane. Although this method has some limitations including low accuracy, our main objective was to validate XTT Cell Viability assay, and the results were almost same in each experiment of TBE. Cell viability for each concentration was indicated as percentage viability (%), assuming that the control well (0.2% DMSO control) is 100 % alive. In order to investigate the effect of 2-DG-HEP-TPP-DCA-HEP coated IONP on HepG2 cell line, cells were treated with these nanoparticles for 24 hour in a dose dependent manner.

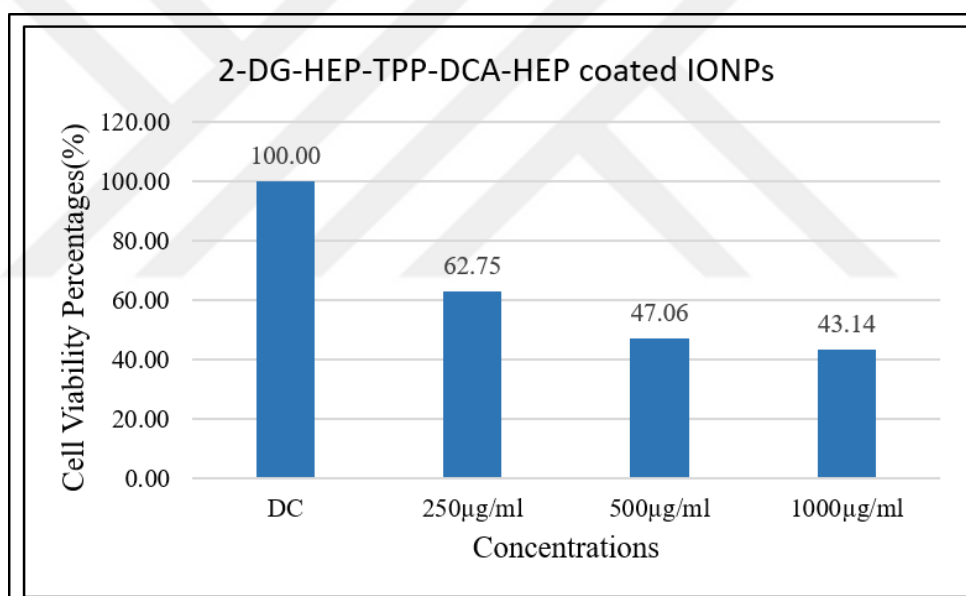


**Figure 69.** Cell viability with TBE method.

The  $IC_{50}$  value that is the concentration required to reduce the cell viability to 50% was calculated as 520 µg/ml (Figure 69). The result was similar with the XTT Cell viability assay results which was calculated as 525 µg/ml.

Figure 69). The result was similar with the XTT Cell viability assay results which was calculated as 525  $\mu\text{g/ml}$ . In order to compare the effect of TPP-DCA, the same experiment was carried on with 2-DG-HEP-TPPDCA-HEP coated IONP and with 2-DG-HEP coated IONP at 250 $\mu\text{g/ml}$ , 500 $\mu\text{g/ml}$ , 1000 $\mu\text{g/ml}$  concentrations. Cell viability percentages were plotted for each concentration and given in Figure 70. The results indicated that TPPDCA is highly effective for cell death. At IC50 value ( $\sim$ 500 $\mu\text{g/ml}$ ), cell viability was found as 60.78%. This result showed that low molecular weight heparin has a role to kill the HepG2 cells. According to Niers et al. [111], heparin have an anti-cancer effect.

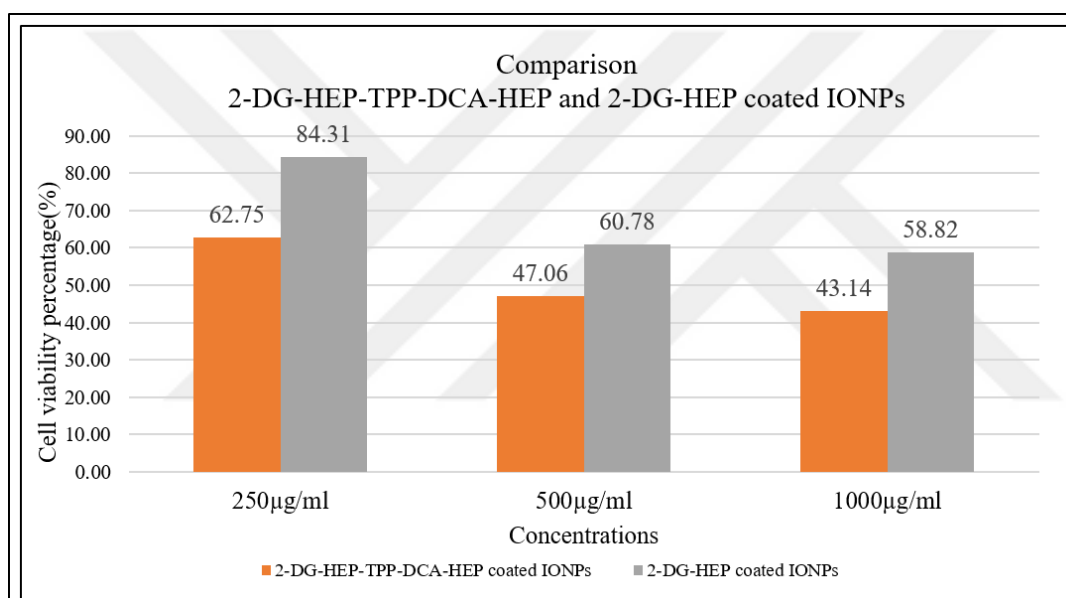


**Figure 70.** Comparison of cell viability of 2-DG-HEP-TPPDCA-HEP coated IONP with 2-DG-HEP coated IONP at 250 $\mu\text{g/ml}$ , 500 $\mu\text{g/ml}$ , 1000 $\mu\text{g/ml}$  concentrations by TBE assay.

In this study, at first, TPP-DCA was attached to the nanoparticle by embedding heparin layers that was used as a coating material. The purpose in this design was to make the attachment of TPP-DCA molecule on the nanoparticles surface more stable. To confirm this idea, trypan blue exclusion method (TBE) was performed for naked, 2-DG-HEP-TPP-DCA-HEP coated and 2-DG-HEP-TPP-DCA coated IONPs at same

concentrations (500 $\mu$ g/ml). Cell viability percentages were plotted. This plot is given in Figure 71 as yellow, blue and green coloured bars representing naked, 2-DG-HEP-TPP-DCA-HEP coated and 2-DG-HEP-TPP-DCA coated IONPs, respectively. According to Figure 71, when TPP-DCA molecules were embedded into heparin layer, stability increased so that TPP-DCA molecules were not detached. Additionally, both of 2-DG-HEP-TPP-DCA-HEP coated and 2-DG-HEP-TPP-DCA coated IONPs are more effective in killing HepG2 cells than the naked IONPs.

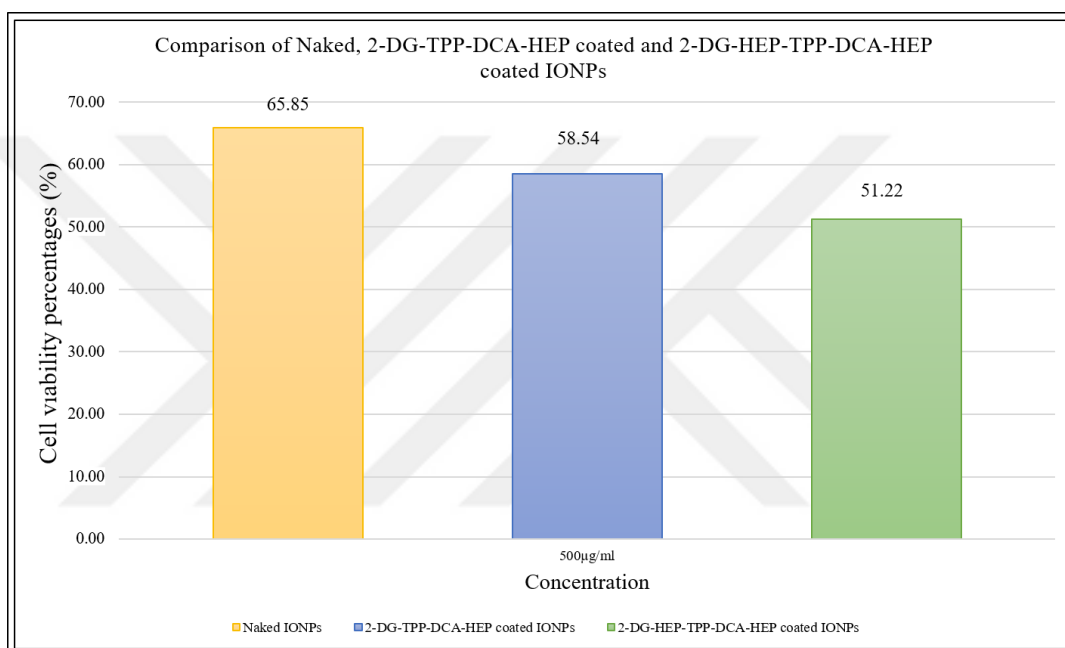


**Figure 71.** Comparison of cell viability of naked, 2-DG-TPP-DCA-HEP coated and 2-DG-HEP-TPP-DCA-HEP coated IONPs at 500  $\mu$ g/ml concentration by trypan blue exclusion ( TBE) method.

In order to understand the efficiency of 2-DG-HEP-TPP-DCA-HEP coated IONPs, Trypan blue exclusion method was used to determine percent cell viability of 2-DG-HEP-TPP-DCA-HEP coated IONPs, TPP-DCA and Na-DCA treated HepG2 cells. Drug loading efficiency had been calculated as 23.3% but results were not found to be reliable. Mass assumption of TPP-DCA and Na-DCA at 500  $\mu$ g/ml IONPs surface was

calculated and treatment was carried out according to this assumption. Cell viability percentages were plotted and shown in Figure 72.

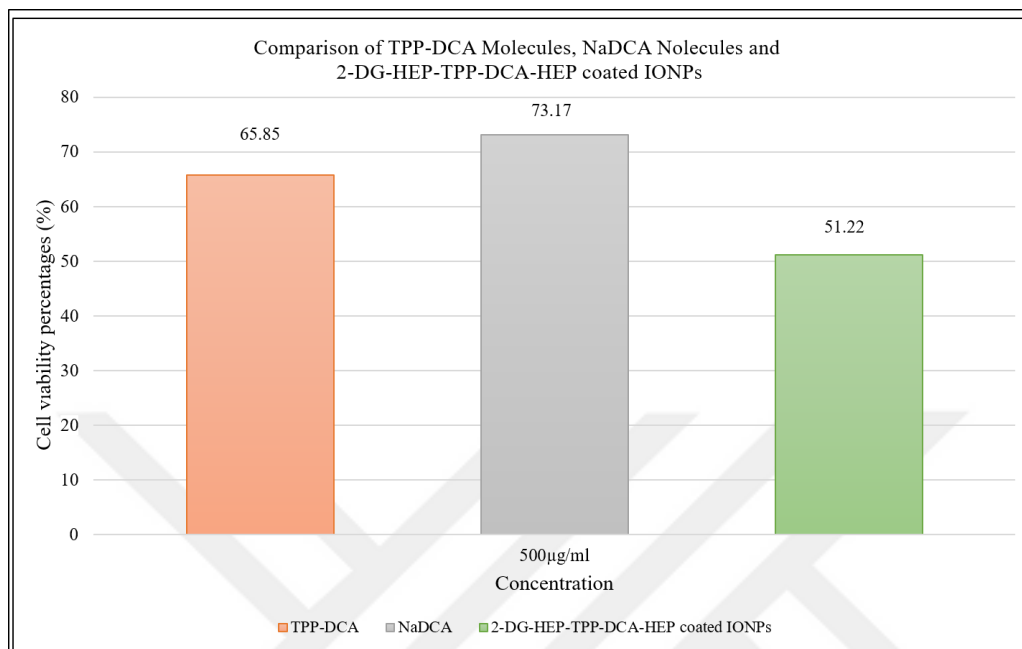


Figure 72. Comparison of cell viability of 2 -DG-HEP-TPP-DCA-HEP coated IONPs, TPP-DCA and Na-DCA at 500µg/ml concentration with TBE method.

When the cell viabilities were compared after treatment with TPP-DCA and NaDCA, TPP-DCA molecules were found to be more effective than the NaDCA. The reason for this results is most probably because DCA molecules are positively charged and become lipid-soluble after modification with TPP, so that TPP-DCA is taken into the mitochondria, which has phospholipid membrane, which is easier with hydrophilic sodium dichloroacetate (DCA) [25]. Our results are similar with the results of a study of Pathak et al.[91]. In our study, according to the plot in Figure 72, 2 -DG-HEP-TPP-DCA-HEP coated IONPs were more efficient than TPP-DCA on HepG2 cells.

2-deoxy-D-glucose (2-DG) is used as targeting agent. Because of the Warburg effect, glucose metabolism is changed and aerobic glycolysis occurs in cancer cells. Cancer cell generates energy via aerobic glycolysis at sufficient oxygen by fermenting glucose into lactate and needs more energy for proliferation and survival. For this reason, they

take more glucose from GLUT receptors. 2-DG is taken into the cancer cells through these receptors. However, 2-DG is not metabolized by glycolysis and also it inhibits glycolytic metabolism [112]. Therefore, labelled TPP-DCA loaded IONPs are taken into the cancer cells via GLUT receptors easier than the TPP-DCA molecules.

### **3.5 Results of Inductive Heating Measurements**

The ability of the home-made instrument to cause magnetically-induced heating was tested using our spherical nanoparticles after each modification of the instrument. These conditions are summarized in Table 6 all assemblies tested caused heating, but there were differences in the heating rates and the final temperatures realized due to the efficiency of magnetic coupling. Temperature kinetic curves obtained after application of an alternating magnetic field on samples dispersed in water at various instrumental conditions stated in Table 6 are given in Figure 73.

**Table 6.** Optimization studies of inductive heating measurements

<b>Name</b>	<b>Coil diameter(cm)</b>	<b>Coil type</b>	<b>Conc. (mg/mL)</b>	<b>Temperature change (°C)</b>	<b>Time (min)</b>	<b>Power supply (kHz)</b>
<b>1</b>	2	wire	160	6	21	130
<b>2</b>	4	wire	160	7,5	90	130
<b>3</b>	4	wire	160	10	20	>130
<b>4</b>	4	wire	160	6	18	>130
<b>5</b>	4	wire	40	2	10	>130
<b>6</b>	4	wire	20	1	10	>130
<b>7</b>	4	wire	40	4,5	6	100 Khz
<b>8</b>	6	pipe	40	7	23	100 khz

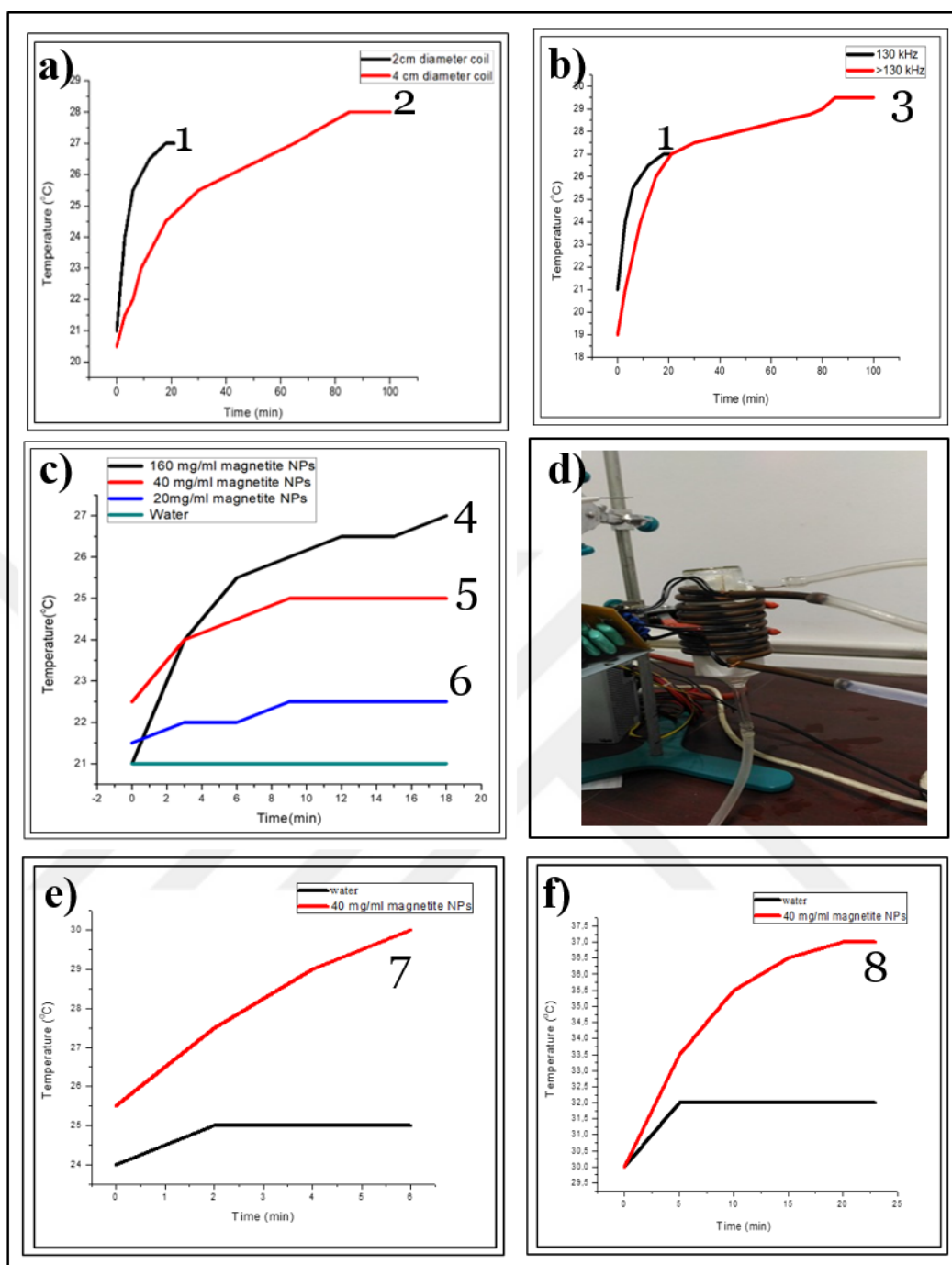


**Figure 73.** (a,b,c,e,f) Temperature kinetic curves obtained after application of an alternating magnetic field on samples dispersed in water at various instrumental conditions stated in Table 6, d.) Photograph of copper pipe coil.

As can be seen from the Figure 73, the promising inductive heating results were obtained only with the combination stated in Table 6 e and f. That is why these two measurements will be discussed.

Figure 73e (7) depicts the heating efficiency of 40mg/mL spherical nanoparticles in water under the magnetic field. Comparing previous trials, this result was very promising. In 6 minutes 4.5° C increasing was measured whereas the temperature of water itself was changed only 1.0° C.

Unfortunately, although performance of the device was desirable, usage of it cause the appliance to become warm. This heating could be not controlled and the device had to be turned off at 6 mins after being turned on. To handle this problem, coil type changed and the helical copper pipe was used (Figure 73, d)By using this pipe (coil diameter is 6cm), cooling water has passed both glass jacket and inside of pipe and heating problem was tried to be overcome.

Results of hyperthermia measurement with pipe coil, Figure 73f, were not as expected. While by using wire coil 4.5° C increasing was observed in 6 minutes, however by using pipe coil 7° C increasing was achieved in 23 munities.

Construction is still in progress. From now on an optical thermometer will be used in temperature measurement



## CHAPTER 4

### CONCLUSION

Dichloroacetate (DCA) is a generic drug for lactic acidosis and a potential metabolic-targeting therapy agent for cancer. It reverses the suppressed mitochondrial apoptosis in cancer and causes in suppression of tumour growth in vitro and in vivo. There is a 40 years of human experience with mechanistic studies of DCA in human tissues. In preclinical vitro and in vivo models there is significant evidences that DCA might be beneficial in human cancer. However it was also reported that DCA might develop symptomatic peripheral neuropathy .Therefore in clinical trials with DCA carefull monitoring of neurotoxicity and establishing clear dose-reduction strategies are advisable in order to overcome toxicities. On the other hand, therapeutically prohibitive high DCA doses are needed for tumor growth suppression. Thus, preparation of magnetic nanoparticles designed to carry pharmacologically relevant doses of DCA directly to the tumor site and enhance its effective cellular uptake may represent a more effective therapeutic option. This was the starting point in this study. Firstly spherical magnetite nanoparticles with 10-20 nm in size and having hydrophilic characteristic were prepared. The second group prepared was flower shaped nanoparticles having a mean diameter of 13.5 nm and they were established of 6 nm sized grains exhibiting maghemite structure. They are found to be superparamagnetic at room temperature and are hydrophylic. The third group prepared was cubic shaped nanoparticles with 7-12 nm distribution exhibiting magnetite crystal structure. They are also superparamagnetic at room temperature but having hydrophobic properties. For this reason they were made hydrophilic by polymer coating. Being hydrophilic all these nanoparticles were suitable for biological applications. For preliminary hyperthermia measurements the spherical particles were chosen due to their larger size compared to the other groups and they were used in all further experiments conducted in the study.

Dichloroacetate is a mitochondrial cancer drug. When it is used orally, its poorly up taken into mitochondria causing a decrease in the efficiency of the treatment. For this reason dichloroacetate was modified by triphenylphosphin and (3-(2,2-dichloroacetoxy)propyl) triphenylphosphonium was synthesized.

To make nanoparticles biocompatible, their surface was coated by heparin, which has negatively charged sulfo groups, creating a negative surface on nanoparticles. This negative charge provide active site for binding of positively charged (3-(2,2-dichloroacetoxy)propyl) triphenylphosphonium. To increase their stability, (3-(2,2-dichloroacetoxy)propyl) triphenylphosphonium molecules must be embedded into heparin layer so nanoparticles coated heparin a second time, and altered surface charges were confirmed by Zeta potential and IR measurements.

2-deoxy-D-glucose molecule was used as targeting agents. 2-deoxy-D-glucose molecules were attached to carboxylic acid side of heparin via EDC/NHS coupling reaction.

To understand the efficiency of 2 -DG-HEP-TPP-DCA-HEP coated IONPs, Trypan blue exclusion method was used determine percentage cell viability (a measure of the destruction capacity) using HepG2 cells. Measurements were carried out for 2 -DG-HEP-TPPDCA-HEP coated IONPs, TPP-DCA and Na-DCA molecules. Cell viability percentages obtained are shown in the Figure 74 given below.

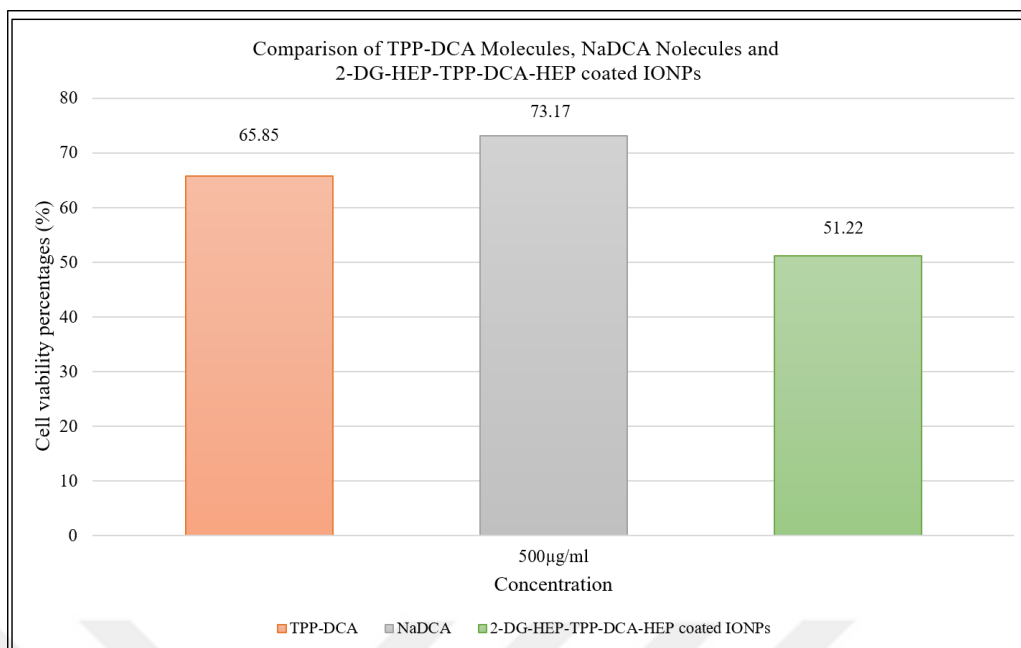


**Figure 74.** Comparison of cell viability of 2-DG-HEP-TPP-DCA-HEP coated IONPs, TPP-DCA and NaDCA molecules at 500µg/mL concentration by Trypan blue exclusion method (TBE)

The percent viabilities observed are 73.2 for commercial NaDCA molecules 65.8 for TPP modified DCA molecules and 51.2 for 2-DG-HEP-TPP-DCA-HEP. The lowest viability is obtained for 2-DG-HEP-TPP-DCA-HEP coated iron oxide nanoparticles prepared in this work turns out to be a very promising result for the aim of this study. For further optimization of the proposed application in the study, hyperthermia measurement are still being carried out using a home-made inductive heating device. So far 0.75 °C/ min heating rate is the best result that is obtained with spherical iron oxide nanoparticles in the aqueous medium.

Another promising side application of these nanoparticles prepared can be their possible use in MRI study



## REFERENCES

- [1] J. Choi and N. S. Wang, "Nanoparticles in Biomedical Applications and Their Safety Concerns," *Biomed. Eng. - From Theory to Appl.*, no. May, pp. 299–314, 2011.
- [2] J. Shi, A. R. Votruba, O. C. Farokhzad, and R. Langer, "Nanotechnology in Drug Delivery and Tissue Engineering: From Discovery to Applications," *Nano Lett.*, vol. 10, no. 9, pp. 3223–3230, 2010.
- [3] M. Fakruddin, Z. Hossain, and H. Afroz, "Prospects and Applications of Nanobiotechnology : A Medical Perspective," *J. Nanobiotechnology*, vol. 10, no. 1, pp. 1–8, 2012.
- [4] C. R. Lowe, "Nanobiotechnology: The Fabrication and Applications of Chemical And Biological Nanostructures," *Nanobiotechnology Lowe*, vol. 10, pp. 428–434, 2000.
- [5] N. Durán and P. D. Marcato, "Nanobiotechnology Perspectives. Role of Nanotechnology In the Food Industry: A Review," *Int. J. Food Sci. Technol.*, vol. 48, pp. 1127–1134, 2013.
- [6] R. Langer and N. A. Peppas, "Advances in Biomaterials, Drug Delivery, and Bionanotechnology," *AIChE J.*, vol. 49, no. 12, pp. 2990–3006, 2003.
- [7] X. Wang, L.-H. Liu, O. Ramström, and M. Yan, "Engineering Nanomaterial Surfaces for Biomedical Applications," *Exp. Biol. Med. (Maywood)*, vol. 234, pp. 1128–1139, 2009.
- [8] W. Wu, Z. Wu, T. Yu, C. Jiang, and W.-S. Kim, "Recent Progress on Magnetic Iron Oxide Nanoparticles: Synthesis, Surface Functional Strategies and Biomedical Applications," *Sci. Technol. Adv. Mater.*, vol. 16, pp. 1–43, 2015.
- [9] J. Li and J.-J. Zhu, "Quantum dots for fluorescent biosensing and bio-imaging applications.," *Analyst*, vol. 138, no. 9, pp. 2506–15, 2013.
- [10] K. E. Uhrich, S. M. Cannizzaro, R. S. Langer, and K. M. Shakesheff, "Polymeric Systems for Controlled Drug Release," *Chem. Rev.*, vol. 99, no. 11, pp. 3181–3198, 1999.

- [11] Y. Zare and I. Shabani, "Polymer/metal nanocomposites for biomedical applications," *Mater. Sci. Eng. C*, vol. 60, no. 28, pp. 195–203, 2016.
- [12] E. S. Kawasaki and A. Player, "Nanotechnology, Nanomedicine, and the Development of New, Effective Therapies for Cancer," *Nanomedicine Nanotechnology, Biol. Med.*, vol. 1, no. 2, pp. 101–109, 2005.
- [13] S. Nie, Y. Xing, G. J. Kim, and J. W. Simons, "Nanotechnology Applications in Cancer," *Annu. Rev. Biomed. Eng.*, vol. 9, no. 1, pp. 257–288, 2007.
- [14] D. Pathania, M. Millard, and N. Neamati, "Opportunities in Discovery and Delivery of Anticancer Drugs Targeting Mitochondria and Cancer Cell Metabolism," *Adv. Drug Deliv. Rev.*, vol. 61, pp. 1250–1275, 2009.
- [15] V. C. Fogg, N. J. Lanning, and J. P. MacKeigan, "Mitochondria in cancer: At the crossroads of life and death," *Chin. J. Cancer*, vol. 30, no. 8, pp. 526–539, 2011.
- [16] J. R. Cantor and D. M. Sabatini, "Cancer Cell Metabolism: One Hallmark, Many Faces," *Cancer Discov.*, vol. 2, no. 10, pp. 881–898, 2012.
- [17] M. V Liberti and J. W. Locasale, "The Warburg Effect: How Does it Benefit Cancer Cells?," *Trends Biochem Sci.*, vol. 41, no. 3, pp. 211–218, 2016.
- [18] A. Mallick, P. More, M. M. K. Syed, and S. Basu, "Nanoparticle-Mediated Mitochondrial Damage Induces Apoptosis in Cancer," *ACS Appl. Mater. Interfaces*, vol. 8, pp. 13218–13231, 2016.
- [19] Z.-P. Chen et al., "Mitochondria-Targeted Drug Delivery System for Cancer Treatment," *J. Drug Target.*, vol. 24, no. 6, pp. 492–502, 2016.
- [20] A. Olszewska and A. Szewczyk, "Mitochondria as a Pharmacological Target: Magnum Overview," *Int. Union Biochem. Mol. Biol.*, vol. 65, no. 3, pp. 273–281, 2013.
- [21] S. Fulda, L. Galluzzi, and G. Kroemer, "Targeting mitochondria for cancer therapy," *Nat. Rev. Drug Discov.*, vol. 9, pp. 447–464, 2010.
- [22] P. W. Stacpoole, E. M. Harman, S. H. Cuury, T. G. Baumgartner, and R. I. Misbin, "Treatment of Lactic Acidosis with Dichloroacetate," *N. Engl. J. Med.*, vol. 70, no. 4, pp. 853–862, 1983.
- [23] D. A. vid W. Crabb, E. A. Yount, and R. A. Harris, "The metabolic effects of dichloroacetate," *Metabolism*, vol. 30, no. 10, pp. 1024–1039, 1981.

- [24] E. D. Michelakis, L. Webster, and J. R. Mackey, "Dichloroacetate (DCA) as A Potential Metabolic-Targeting Therapy for Cancer," *Br. J. Cancer*, vol. 99, pp. 989–994, 2008.
- [25] M. F. Ross et al., "Lipophilic Triphenylphosphonium Cations as Tools in Mitochondrial Bioenergetics and Free Radical Biology," *Biochem.*, vol. 70, no. 2, pp. 222–230, 2005.
- [26] S. Mornet, S. Vasseur, F. Grasset, and E. Duguet, "Magnetic Nanoparticle Design for Medical Diagnosis and Therapy," *J. Mater. Chem.*, vol. 14, pp. 2161–2175, 2004.
- [27] A. B. Salunkhe, V. . M. Khot, and S. H. Pawar, "Magnetic Hyperthermia with Magnetic Nanoparticles: A Status Review," *Curr. Top. Med. Chem.*, vol. 14, pp. 1–23, 2014.
- [28] A. J. Giustini, A. A. Petryk, S. A. Cassim, J. A. Tate, I. Baker, and P. J. Hoopes, "Magnetic Nanoparticle Hyperthermia in Cancer Treatment," *Nano Life*, vol. 1, pp. 1–23, 2013.
- [29] T. O. Tasci, I. Vargel, A. Arat, E. Guzel, P. Korkusuz, and E. Atalar, "Focused RF Hyperthermia Using Magnetic Fluids," *Med. Phys.*, vol. 36, no. 5, pp. 1906–1912, 2009.
- [30] M. Prabakaran, J. J. Grailer, S. Pilla, D. A. Steeber, and S. Gong, "Gold nanoparticles with a monolayer of doxorubicin-conjugated amphiphilic block copolymer for tumor-targeted drug delivery," *Biomaterials*, vol. 30, no. 30, pp. 6065–6075, 2009.
- [31] M. Nurunnabi, Z. Khatun, W.-C. Moon, G. Lee, and Y.-K. Lee, "Heparin Based Nanoparticles for Cancer Targeting and Noninvasive Imaging," *Quant. Imaging Med. Surg.*, vol. 2, no. 3, pp. 219–26, 2012.
- [32] H.-J. Chai et al., "Renal Targeting Potential of a Polymeric Drug Carrier, Poly-L-Glutamic Acid, in Normal and Diabetic Rats," *Int. J. Nanomedicine*, vol. 12, pp. 577–591, 2017.
- [33] X. Mao, J. Xu, and H. Cui, "Functional nanoparticles for magnetic resonance imaging," *Wiley Interdiscip. Rev. Nanomedicine Nanobiotechnology*, vol. 8, no. 6, pp. 814–841, 2016.
- [34] J.-S. Baek and C.-W. Cho, "A multifunctional lipid nanoparticle for co-delivery

- of paclitaxel and curcumin for targeted delivery and enhanced cytotoxicity in multidrug resistant breast cancer cells.,” *Oncotarget*, vol. 8, no. 18, pp. 30369–30382, 2017.
- [35] A. K. Singla, A. Garg, and D. Aggarwal, “Paclitaxel and its formulations,” *Int. J. Pharm.*, vol. 235, no. 1–2, pp. 179–192, 2002.
- [36] M. Vendrell, K. K. Maiti, K. Dhaliwal, and Y.-T. Chang, “Surface-enhanced Raman scattering in cancer detection and imaging,” *Trends Biotechnol.*, vol. 31, no. 4, pp. 249–257, 2013.
- [37] A. B. Chinen, C. M. Guan, J. R. Ferrer, S. N. Barnaby, T. J. Merkel, and C. A. Mirkin, “Nanoparticle Probes for the Detection of Cancer Biomarkers, Cells, and Tissues by Fluorescence,” *Chem. Rev.*, vol. 115, no. 19, pp. 10530–10574, 2015.
- [38] A. Miaskowski and A. Krawczyk, “Magnetic Fluid Hyperthermia for Cancer Therapy,” *PRZEGLĄD ELEKTROTECHNICZNY (Electrical Rev.)*, no. 12, pp. 125–127, 2011.
- [39] M. Banobre-Lopez, A. Teijeiro, and J. Rivas, “Magnetic nanoparticle-based hyperthermia for cancer treatment,” *Reports Pract. Oncol. Radiother.*, vol. 18, no. 6, pp. 397–400, 2013.
- [40] A. G. Kolhatkar, A. C. Jamison, D. Litvinov, R. C. Willson, and T. R. Lee, “Tuning the Magnetic Properties of Nanoparticles,” *Int. J. Mol. Sci.*, vol. 14, pp. 15977–16009, 2013.
- [41] Z. Hedayatnasab, F. Abnisa, and W. M. A. W. Daud, “Review on Magnetic Nanoparticles Formagnetic Nanofluid Hyperthermia Application,” *Mater. Des.*, vol. 123, pp. 174–196, 2017.
- [42] W. Wu, Z. Wu, T. Yu, C. Jiang, and W. Kim, “Recent Progress on Magnetic Iron Oxide Nanoparticles: Synthesis, Surface Functional Strategies and Biomedical Applications,” *Sci. Technol. Adv. Mater.*, vol. 16, pp. 1–43, 2015.
- [43] A. S. Teja and P. Y. Koh, “Synthesis, Properties, and Applications of Magnetic Iron Oxide Nanoparticles,” *Prog. Cryst. Growth Charact. Mater.*, vol. 55, pp. 22–45, 2009.
- [44] H. Guo and A. S. Barnard, “Naturally Occurring Iron Oxide Nanoparticles: Morphology, Surface Chemistry and Environmental Stability,” *J. Mater. Chem.*



- A, vol. 1, pp. 27–42, 2013.
- [45] J. Santoyo Salazar et al., “Magnetic Iron Oxide Nanoparticles in 10-40 nm Range: Composition in Terms of Magnetite/Maghemite Ratio and Effect on the Magnetic Properties,” *Chem. Mater.*, vol. 23, pp. 1379–1386, 2011.
- [46] S. Dutz and R. Hergt, “Magnetic Nanoparticle Heating and Heat Transfer on A Microscale: Basic Principles, Realities and Physical Limitations of Hyperthermia for Tumour Therapy,” *Int. J. Hyperth.*, vol. 29, no. 8, pp. 790–800, 2013.
- [47] A. E. Deatsch and B. A. Evans, “Heating Efficiency in Magnetic Nanoparticle Hyperthermia,” *J. Magn. Magn. Mater.*, vol. 354, pp. 163–172, 2014.
- [48] G. Nedelcu, “Magnetic nanoparticles impact on tumoral cells in the treatment by magnetic fluid hyperthermia,” *Dig. J. Nanomater. Biostructures*, vol. 3, no. 3, pp. 103–107, 2008.
- [49] A. K. Gupta and M. Gupta, “Synthesis and Surface Engineering of Iron Oxide Nanoparticles for Biomedical Applications,” *Biomaterials*, vol. 26, pp. 3995–4021, 2005.
- [50] W. Wu, Q. He, and C. Jiang, “Magnetic Iron Oxide Nanoparticles: Synthesis and Surface Functionalization Strategies,” *Nanoscale Res. Lett.*, vol. 3, pp. 397–415, 2008.
- [51] Y. S. Kang, S. Risbud, J. F. Rabolt, and P. Stroeve, “Synthesis and Characterization of Nanometer-Size Fe<sub>3</sub>O<sub>4</sub> And  $\Gamma$ -Fe<sub>2</sub>O<sub>3</sub> Particles,” *Chem. Mater.*, vol. 8, no. 9, pp. 2209–2211, 1996.
- [52] T. Hyeon, “Chemical Synthesis of Magnetic Nanoparticles,” *Chem. Commun.*, pp. 927–934, 2003.
- [53] G. Zhen et al., “Comparative Study of the Magnetic Behavior of Spherical and Cubic Superparamagnetic Iron Oxide Nanoparticles,” *J. Phys. Chem. C*, vol. 115, no. 2, pp. 327–334, 2011.
- [54] S. H. Noh et al., “Nanoscale Magnetism Control via Surface and Exchange Anisotropy for Optimized Ferrimagnetic Hysteresis,” *Nano Lett.*, vol. 12, pp. 3716–3721, 2012.
- [55] A. Ali et al., “Synthesis, Characterization, Applications, and Challenges of Iron Oxide Nanoparticles,” *Nanotechnol. Sci. Appl.*, vol. 9, pp. 49–67, 2016.

- [56] S. F. Hasany, I. Ahmed, R. J, and A. Rehman, "Systematic Review of the Preparation Techniques of Iron Oxide Magnetic Nanoparticles," *Nanosci. Nanotechnol.*, vol. 2, no. 6, pp. 148–158, 2012.
- [57] Z.-A. Lin, J.-N. Zheng, F. Lin, L. Zhang, Z. Cai, and G.-N. Chen, "Synthesis of Magnetic Nanoparticles with Immobilized Aminophenylboronic Acid for Selective Capture of Glycoproteins," *J. Mater. Chem.*, vol. 21, pp. 518–524, 2011.
- [58] L. Shen et al., "Facile Co-Precipitation Synthesis of Shape-Controlled Magnetite Nanoparticles," *Ceram. Int.*, vol. 40, pp. 1519–1524, 2014.
- [59] M. R. Dewi, W. M. Skinner, and T. Nann, "Synthesis and Phase Transfer of Monodisperse Iron Oxide (Fe<sub>3</sub>O<sub>4</sub>) Nanocubes," *Aust. J. Chem.*, vol. 67, pp. 663–669, 2014.
- [60] P. Guardia et al., "One Pot Synthesis of Monodisperse Water Soluble Iron Oxide Nanocrystals with High Values of the Specific Absorption Rate," *J. Mater. Chem. B*, vol. 2, pp. 4426–4434, 2014.
- [61] Z. Xu, C. Shen, Y. Tian, X. Shi, and H.-J. Gao, "Organic Phase Synthesis of Monodisperse Iron Oxide Nanocrystals Using Iron Chloride as Precursor," *Nanoscale*, vol. 2, pp. 1027–1032, 2010.
- [62] S. Sheng-Nan, W. Chao, Z. Zan-zan, H. Yang-Long, S. S. Venkatraman, and X. Zhi-Chuan, "Magnetic Iron Oxide Nanoparticles: Synthesis and Surface Coating Techniques for Biomedical Applications," *Chinese Phys. Soc.*, vol. 23, no. 3, pp. 1–19, 2014.
- [63] P. Guardia et al., "Water-Soluble Iron Oxide Nanocubes with High Values of Specific Absorption Rate for Cancer Cell Hyperthermia Treatment," *ACS Nano*, vol. 6, no. 4, pp. 3080–3091, 2012.
- [64] S. Sun and H. Zeng, "Size-Controlled Synthesis of Magnetite Nanoparticles," *J. Am. Chem. Soc.*, vol. 124, no. 28, pp. 8204–8205, 2002.
- [65] S.-N. Sun, C. Wei, Z.-Z. Zhu, Y.-L. Hou, S. S. Venkatraman, and Z.-C. Xu, "Magnetic Iron Oxide Nanoparticles: Synthesis and Surface Coating Techniques for Biomedical Applications," *Chinese Phys. B*, vol. 23, no. 3, pp. 1–19, 2014.
- [66] W. Y. Rho et al., "Facile Synthesis of Monodispersed Silica-Coated Magnetic

- Nanoparticles,” *J. Ind. Eng. Chem.*, pp. 1–4, 2013.
- [67] M. Z. Iqbal et al., “Silica-Coated Super-Paramagnetic Iron Oxide Nanoparticles (Spionps): A New Type Contrast Agent of T1 Magnetic Resonance Imaging (MRI),” *J. Mater. Chem. B*, vol. 3, pp. 5172–5181, 2015.
- [68] D. Caruntu, G. Caruntu, Y. Chen, C. J. O’Connor, G. Goloverda, and V. L. Kolesnichenko, “Synthesis of Variable-Sized Nanocrystals of Fe<sub>3</sub>O<sub>4</sub> with High Surface Reactivity,” *Chem. Mater.*, vol. 16, no. 25, pp. 5527–5534, 2004.
- [69] R. Hachani et al., “Polyol Synthesis, Functionalisation, and Biocompatibility Studies of Superparamagnetic Iron Oxide Nanoparticles as Potential MRI Contrast Agents,” *Nanoscale*, vol. 8, pp. 3278–3287, 2016.
- [70] K. Niemirowicz, K. Markiewicz, A. Wilczewska, and H. Car, “Magnetic Nanoparticles as New Diagnostic Tools in Medicine,” *Adv. Med. Sci.*, vol. 57, no. 2, pp. 196–207, 2012.
- [71] S. Laurent, J.-L. Bridot, L. Vander Elst, and R. N. Muller, “Magnetic Iron Oxide Nanoparticles for Biomedical Applications,” *Future Med. Chem.*, vol. 2, no. 3, pp. 427–449, 2010.
- [72] H. Khurshid et al., “Development of Heparin-Coated Magnetic Nanoparticles for Targeted Drug Delivery Applications,” *J. Appl. Phys.*, vol. 105, no. 7, pp. 105–106, 2009.
- [73] T. Liu et al., “Immobilization of Heparin/Poly-L-Lysine Nanoparticles on Dopamine-Coated Surface to Create A Heparin Density Gradient for Selective Direction of Platelet and Vascular Cells Behavior,” *Acta Biomater.*, vol. 10, pp. 1940–1954, 2014.
- [74] H. Jack, J. L. Shaughnessy, Stephen G. Halperin, C. Granger, E. M. Ohman, and J. E. Dalen, “Heparin and Low-Molecular- Weight Heparin Mechanisms of Action, Pharmacokinetics, Dosing, Monitoring, Efficacy, and Safety Jack,” in *Sixth ACCP Consensus Conference on Antithrombotic Therapy*, 2001, p. 64S–94S.
- [75] A. B. Salunkhe, V. M. Khot, and S. H. Pawar, “Magnetic Hyperthermia with Magnetic Nanoparticles: A Status Review,” *Curr. Top. Med. Chem.*, vol. 14, no. 6, pp. 1–23, 2014.
- [76] D. Ortega and Q. A. Pankhurst, “Magnetic Hyperthermia,” *Nanoscience*, vol. 1,

- pp. 60–88, 2013.
- [77] A. Jordan, R. Scholz, P. Wust, H. Fahling, and R. Felix, “Magnetic Fluid Hyperthermia (MFH): Cancer Treatment with AC Magnetic Field Induced Excitation of Biocompatible Superparamagnetic Nanoparticles,” *J. Magn. Mater.*, vol. 201, pp. 413–419, 1999.
- [78] S. U. S. Mohite, P. P. Shreshtha, and G. K. Jadhav, “Review on Thermal Seeds in Magnetic Hyperthermia Therapy,” *Int. J. Innov. Technol. Res.*, vol. 3, no. 4, pp. 2283–2287, 2015.
- [79] A. Hervault and N. T. K. Thanh, “Magnetic Nanoparticle-Based Therapeutic Agents for Thermo-Chemotherapy Treatment of Cancer,” *Nanoscale*, vol. 6, pp. 11553–11573, 2014.
- [80] S. Laurent, S. Dutz, U. O. Häfeli, and M. Mahmoudi, “Magnetic Fluid Hyperthermia: Focus on Superparamagnetic Iron Oxide Nanoparticles,” *Adv. Colloid Interface Sci.*, vol. 166, pp. 8–23, 2011.
- [81] A. J. Giustini, A. A. Petryk, S. A. Cassim, J. A. Tate, I. Baker, and P. J. Hoopes, “Magnetic Nanoparticle Hyperthermia in Cancer Treatment,” *Nano Life*, vol. 1, pp. 1–23, 2013.
- [82] A. Jordan, P. Wust, H. Föhling, W. John, A. Hinz, and R. Felix, “Inductive Heating of Ferrimagnetic Particles and Magnetic Fluids: Physical Evaluation of Their Potential for Hyperthermia,” *Int. J. Hyperth.*, vol. 25, no. 7, pp. 499–511, 2009.
- [83] Q. A. Pankhurst, N. T. K. Thanh, S. K. Jones, and J. Dobson, “Progress in Applications of Magnetic Nanoparticles in Biomedicine,” *J. Phys. D: Appl. Phys.*, vol. 42, pp. 1–15, 2009.
- [84] K. Maier-Hauff et al., “Intracranial Thermotherapy Using Magnetic Nanoparticles Combined with External Beam Radiotherapy: Results of A Feasibility Study on Patients with Glioblastoma Multiforme,” *Int. J. Radiat. Oncol. Biol. Phys.*, vol. 81, pp. 53–60, 2007.
- [85] Z.-A. Lin, J.-N. Zheng, F. Lin, L. Zhang, Z. Cai, and G.-N. Chen, “Synthesis of Magnetic Nanoparticles with Immobilized Aminophenylboronic Acid for Selective Capture of Glycoproteins,” *J. Mater. Chem.*, vol. 21, p. 518, 2011.
- [86] P. Hugounenq et al., “Iron Oxide Monocrystalline Nanoflowers for Highly

- Efficient Magnetic Hyperthermia,” *J. Phys. Chem. C*, vol. 116, pp. 15702–15712, 2012.
- [87] X. Liu, G. Qiu, and X. Li, “Shape-Controlled Synthesis and Properties of Uniform Spinel Cobalt Oxide Nanocubes,” *Nanotechnology*, vol. 16, no. 12, pp. 3035–3040, 2005.
- [88] D. Kim, N. Lee, M. Park, B. H. Kim, K. An, and T. Hyeon, “Synthesis of Uniform Ferrimagnetic Magnetite Nanocubes,” *J. AM. CHEM. SOC*, vol. 131, pp. 454–455, 2009.
- [89] W. Y. Rho et al., “Facile synthesis of monodispersed silica-coated magnetic nanoparticles,” *J. Ind. Eng. Chem.*, vol. 20, no. 5, pp. 2646–2649, 2014.
- [90] R. K. Pathak, S. Marrache, D. A. Harn, and S. Dhar, “Mito-DCA: A mitochondria targeted molecular scaffold for efficacious delivery of metabolic modulator dichloroacetate,” *ACS Chem. Biol.*, vol. 9, no. 5, pp. 1178–1187, 2014.
- [91] R. K. Pathak, S. Marrache, D. A. Harn, and S. Dhar, “Mito-DCA: A Mitochondria Targeted Molecular Scaffold for Efficacious Delivery of Metabolic Modulator Dichloroacetate,” *ACS Chem. Biol.*, vol. 9, pp. 1178–1187, 2014.
- [92] F. Xiong et al., “Preparation, Characterization of 2-Deoxy-D-Glucose Functionalized Dimercaptosuccinic Acid-Coated Maghemite Nanoparticles for Targeting Tumor Cells Fei,” *Pharm. Res.*, vol. 29, pp. 1087–1097, 2012.
- [93] K. S. Başkan, E. Tütem, E. Akyüz, S. Özen, and R. Apak, “Spectrophotometric total reducing sugars assay based on cupric reduction,” *Talanta*, vol. 147, pp. 162–168, 2016.
- [94] N. M. Salem and A. M. Awwad, “A Novel Approach for Synthesis Magnetite Nanoparticles at Ambient Temperature,” *Nanosci. Nanotechnol.*, vol. 3, no. 3, pp. 35–39, 2013.
- [95] S. Rajput, L. P. Singh, C. U. Pittman Jr., and D. Mohan, “Lead (Pb<sup>2+</sup>) and Copper (Cu<sup>2+</sup>) Remediation From Water Using Superparamagnetic Maghemite (C-Fe<sub>2</sub>O<sub>3</sub>) Nanoparticles Synthesized by Flame Spray Pyrolysis (FSP),” *J. Colloid Interface Sci.*, vol. 492, pp. 176–190, 2017.
- [96] P. Kucheryavy et al., “Superparamagnetic iron oxide nanoparticles with

- variable size and an iron oxidation state as prospective imaging agents.,” *Langmuir*, vol. 29, no. 2, pp. 710–6, 2013.
- [97] P. Hugounenq et al., “Iron Oxide Monocrystalline Nanoflowers for Highly Efficient Magnetic Hyperthermia,” *J. Phys. Chem. C*, vol. 116, pp. 15702–15712, 2012.
- [98] D. Vollath, D. V Szabó, R. D. Taylor, J. O. Willis, and K. E. Sickafus, “Synthesis and properties of nanocrystalline superparamagnetic gamma-Fe<sub>2</sub>O<sub>3</sub>,” *Nanostructured Mater.*, vol. 6, no. 5–8, pp. 941–944, 1995.
- [99] C. Han, J. Xie, C. Deng, and D. Zhao, “A Facile Synthesis of Porous Hematite Nanomaterials and Their Fast Sorption of Cr (VI) in Wastewater,” *J. Chil. Chem. Soc.*, vol. 4, no. 57, pp. 1372–1374, 2012.
- [100] K. E. Gilbert and J. J. Gajewski, “Coal Liquefaction Model Studies: Free Radical Chain Decomposition of Diphenylpropane, Dibenzyl Ether, and Phenyl Ether via  $\beta$ -Scission Reactions,” *J. Org. Chem.*, vol. 47, no. 25, pp. 4899–4902, 1982.
- [101] W. Lu, M. Ling, M. Jia, P. Huang, C. Li, and B. Yan, “Facile Synthesis and Characterization of Polyethylenimine-Coated Fe<sub>3</sub>O<sub>4</sub> Superparamagnetic Nanoparticles for Cancer Cell Separation,” *Mol. Med. Rep.*, vol. 9, pp. 1080–1084, 2014.
- [102] K. M. Koczkur, S. Mourdikoudis, L. Polavarapu, and S. E. Skrabalak, “Polyvinylpyrrolidone (PVP) in Nanoparticle Synthesis,” *Dalt. Trans.*, vol. 44, pp. 17883–17905, 2015.
- [103] K. D. Bakoglidis, K. Simeonidis, D. Sakellari, G. Stefanou, and M. Angelakeris, “Size-dependent mechanisms in AC magnetic hyperthermia response of iron-oxide nanoparticles,” *IEEE Trans. Magn.*, vol. 48, no. 4, pp. 1320–1323, 2012.
- [104] Q. Wu et al., “Heparinized Magnetic Mesoporous Silica Nanoparticles as Multifunctional Growth Factor Delivery Carriers,” *Nanotechnology*, vol. 23, no. 48, pp. 1–9, 2012.
- [105] K. Ah Min, F. Yu, V. C. Yang, X. Zhang, and G. R. Rosania, “Transcellular Transport of Heparin-coated Magnetic Iron Oxide Nanoparticles (Hep-MION) Under the Influence of an Applied Magnetic Field,” *Pharmaceutics*, vol. 2, pp. 119–135, 2010.

- [106] A. Javid, S. Ahmadian, A. A. Saboury, S. M. Kalantarc, and R.-Z. Saeed, "Novel Biodegradable Heparin-Coated Nanocomposite System for Targeted Drug Delivery," *RSC Adv.*, vol. 4, pp. 13719–13728, 2014.
- [107] N. Bogdan et al., "Bio-Functionalization of Ligand-Free Upconverting Lanthanide Doped Nanoparticles for Bio-Imaging and Cell Targeting," *Nanoscale*, vol. 4, pp. 3647–3650, 2012.
- [108] Y. P. Singh and R. A. Singh, "Theoretical Studies of Different Tautomers of Anti Cancer Drug: Dichloroacetate," *Pak. J. Pharm. Sci.*, vol. 21, no. 4, pp. 390–395, 2008.
- [109] K. A. Jensen and P. H. Nielsen, "Infrared Spectra of Some Organic Compounds of Group V B Elements," *Acta Chemica Scandinavica*, vol. 17, no. 7. pp. 1875–1885, 1963.
- [110] P. Wang, H. Kouyoumdjian, D. C. Zhu, and X. Huang, "Heparin nanoparticles for  $\beta$  amyloid binding and mitigation of  $\beta$  amyloid associated cytotoxicity," *Carbohydr. Res.*, vol. 405, pp. 110–114, 2015.
- [111] T. M. H. Niers et al., "Mechanisms of heparin induced anti-cancer activity in experimental cancer models," *Crit. Rev. Oncol. Hematol.*, vol. 61, no. 3, pp. 195–207, 2007.
- [112] D. Zhang, J. Li, F. Wang, J. Hu, S. Wang, and Y. Sun, "2-Deoxy-D-glucose targeting of glucose metabolism in cancer cells as a potential therapy," *Cancer Lett.*, vol. 355, no. 2, pp. 176–183, 2014.





## CURRICULUM VITAE

### PERSONAL INFORMATION

Name SURNAME: Yeliz AKPINAR

Address : Middle East Technical University, Department of CHEMISTRY

Telephone : +903122103245

E- mail : akpinar@metu.edu.tr/ yeliz.akpinar@hotmail.com

Nationality : Republic of Turkey

Date of birth : 13.02.1985

### Educations:

Post- Bachelor of Doctoral: MIDDLE EAST TECHNICAL UNIVERSITY  
Graduate School of Natural and Applied Science,  
2010 -2017

Thesis Title: HEPARIN COATED AND 2-DEOXY-D-GLUCOSE  
CONJUGATED IRON OXIDE NANOPARTICLES FOR HYPERTHERMIA  
TREATMENT

Supervisor: Prof. Dr.MURVET VOLKAN

Co-supervisor: Prof. Dr. N.TULUN GURAY

English preparatory class: Basic English Department, 2009-2010

Bachelor of Science : GAZI UNIVERSITY  
Department of Education/ Chemistry Education  
2004-2009

### PROFESSIONAL EMPLOYMENT :

1.) Research Asistant: ORTA DOĞU TEKNİK ÜNİVERSİTESİ/FEN-EDEBİYAT  
FAKÜLTESİ/KİMYA BÖLÜMÜ/KİMYA ANABİLİM DALI), 2010-2017 ,  
(ÖYP Asistant)

2.) Research Asistant: AHİ EVRAN ÜNİVERSİTESİ/FEN-EDEBİYAT  
FAKÜLTESİ/KİMYA BÖLÜMÜ/ANALİTİK KİMYA ANABİLİM DALI), 2009-  
2010

A.)Publication (SCI)

1.) AŞIK ELİF,AKPINAR YELİZ,GÜRAY NÜLÜFER TÜLÜN,İŞCAN MESUDE,ÇAKMAK DEMİRCİGİL GONCA,VOLKAN MÜRUVET (2016). Cellular uptake genotoxicity and cytotoxicity of cobalt ferrite magnetic nanoparticles in human breast cells. Toxicology Research, 5(6), 1649-1662., Doi: 10.1039/C6TX00211K (Yayın No: 3223404)

2.)DZUDZEVIC CANCAR HURİJA,SÖYLEMEZ SANİYE,AKPINAR YELİZ,KESİK MELİS,GÖKER SEZA,GÜNBAŞ EMRULLAH GÖRKEM,VOLKAN MÜRUVET,TOPPARE LEVENT KAMİL (2016). A Novel Acetylcholinesterase Biosensor Core Shell Magnetic Nanoparticles Incorporating a Conjugated Polymer for the Detection of Organophosphorus Pesticides. ACS Applied Materials & Interfaces, 8(12), 8058-8067., Doi: 10.1021/acsami.5b12383 (Yayın No: 3206783)

B.) Presentations ( National and International Congress, Meetings, etc.)

1.)AKPINAR YELİZ,VOLKAN MÜRUVET (2016). Preparation of Biocompatible Magnetic Nanoparticles for Hyperthermia Treatment. 10th Aegean Analytical Chemistry Days: AACD 2016 (Özet Bildiri/Poster)(Yayın No:3159107)

2.)YELİZ AKPINAR, MURAT KAYA, MÜRUVET VOLKAN, Preparation and Characterization of  $\text{CoFe}_2\text{O}_4@\text{SiO}_2@\text{Au}$  Nanoparticles, 9th Aegean Analytical Chemistry Days, AACD 2012, September 29-October 3, 2014, Chios, Greece (RSC Analyst Best Poster Award)

3.)CEREN UZUN, YELİZ AKPINAR, MURAT KAYA, MÜRUVET VOLKAN, Synthesis and Characterization of Surface Enhanced Raman Scattering Tags with Ag and Au Core-Ag Shell Nanostructures, NanoTR7, 2011, Nanoscience and

4.)CEREN UZUN, YELİZ AKPINAR, MURAT KAYA, MÜRUVET VOLKAN, Raman-Dye-Labeled Nanoparticle Probes for DNA Studies, NanoTR8, 25-29 June 2012, Nanoscience and Nanotechnology Conference, Hacettepe University, Ankara, Turkey

- 5.) YELİZ APINAR, CEREN UZUN, MÜRVEVET VOLKAN, Preparation of Mono disperse Iron -oxide Nanoparticles Through Seed-mediated Growth. NanoTR8, 25-29 June 2012, Nanoscience and Nanotechnology Conference, Hacettepe University, Ankara, Turkey
- 6.)YELİZ AKPINAR, MURAT KAYA AND MÜRVEVET VOLKAN, Usage of silica coated magnetic nanoparticles and SERS nanotags for gene detection, 22nd IUBMB & 37th FEBS Congress, 1-11 September, 2012, in Seville (Spain).
- 7.) NEHİR UTKU, YELİZ AKPINAR , ERDAL BAYRAMLI, MÜRVEVET VOLKAN, Preparation of Highly Ordered Gold Nanorod Monolayer and Multilayers by Langmuir Technique, NanoTR10, 17-21 June 2014, Nanoscience and Nanotechnology Conference, Yeditepe University, İstanbul, Turkey (Best Poster Awards)
- 8.) YELİZ AKPINAR, SEÇKİN ÖZTÜRK, MÜRVEVET VOLKAN, Manyetik Hipertermi Tedavisinde Kullanıma Uygun Manyetik Nanoparçacıklarının Hazırlanması, 29. Ulusal Kimya Kongresi, 10-14 Eylül , Ankara,(Oral Preasentation).